University of Southampton

Faculty of Engineering and Physical Sciences

Optoelectronics Research Centre

Chalcogenide Platforms for Photonic Metamaterials

by

Davide Piccinotti

Thesis for the degree of Doctor of Philosophy

November 2018

University of Southampton

Abstract

Faculty of Engineering and Physical Sciences

Optoelectronics Research Centre

Thesis for the degree of Doctor of Philosophy

Chalcogenide Platforms for Photonic Metamaterials

by Davide Piccinotti

Photonic metamaterials - media artificially structured at the nanometre scale - provide extraordinary optical properties not found in nature. In this work I explored opportunities provided by changes of complex optical properties of chalcogenide alloys related to compositional variation and structural phase change to develop switchable and tunable plasmonic and dielectric metamaterials:

- **I have systematically explored the properties of Bi:Sb:Te across UV to near infrared wavelengths through combinatorial high-throughput mapping techniques for the widest compositional spread reported so far.** This study reveals that Bi:Sb:Te has better plasmonic properties than gold at wavelengths below 580 nm and silver below 365 nm; ability to support dielectric (Mie) resonances better than oxides at telecommunication wavelengths beyond 1200 nm; epsilon-near-zero properties across UV to IR wavelengths; sub-unity refractive index (down to 0.7) in the UV and the highest refractive index in the near-IR (up to 11.5 at 1680 nm) reported so far to our knowledge.
- **I have studied for the first time the plasmonic character of amorphous Bi:Te and developed resonant optical metasurfaces based on this alloy that present strong, period-dependent plasmonic absorption resonances (Q_{Max} = 7.5) in the visible range.** Furthermore, I have investigated changes of optical properties of this alloy upon structural phase change from amorphous to crystalline phases.
- **I have studied for the first time channelling of light through nano-hole arrays filled with dispersive low-epsilon chalcogenides.** The complex changes in the composite's spectral response depend strongly on the interplay between the dispersion of the optical properties of the plasmonic nanostructure and the low-epsilon medium and lead to increase of transmission over a broad range of plasmonic frequencies.
- **I have developed the first switchable UV metamaterials that exploits the low refractive index (equal to 1.07 at 245 nm for *c*-GST) and phase change properties of chalcogenides**. In particular, I have shown that laser-induced structural phase transitions can be used to switch quality factors of dielectric resonances (Q_{Max} = 15) in metamaterials without affecting their spectral positions.

Table of Contents

Table of Contents i
List of Tables v
List of Figures vii
List of Acronyms xiii
Research Thesis: Declaration of Authorship xv
Acknowledgements xvii
Chapter 1 Introduction 1
1.1 Photonic Metamaterials 2
1.1.1 Plasmonic Metamaterials 3
1.1.2 All-dielectric Metamaterials 5
1.1.3 Chalcogenide Functional Metamaterials 8
1.2 Motivation and Project Aim 11
1.3 Thesis Synopsis 12
1.4 Summary 14
Chapter 2 Chalcogenide Semiconductor Alloys for Photonic Applications 15
2.1 Introduction 15
2.2 Combinatorial and High-Throughput Methodology 15
2.3 BST Chalcogenide Platform 18
2.4 Lorentz Oscillator Model 19
2.5 High-Throughput Deposition and Characterization of BST 23
2.5.1 XRD analysis vs Composition 26
2.5.2 Raman Spectroscopy vs Composition 29
2.5.3 Resistivity Measurements vs Composition 33
2.5.4 Compositional Tuning of Optical Properties 34
2.6 Summary 44

Chapter 3 Plasmonic and Phase Change Properties of Bi:Te for Metamaterials Application 47

3.1 Introduction 47
3.2 Fabrication of Nanostructures 47
3.3 Results and Discussion: Optical Spectra and Simulations 50
3.4 Compositional-Dependent Optical Properties 53
3.5 Phase Change Properties of Bi:Te Thin Films 55
3.6 Summary 64

Chapter 4 Epsilon-Near-Zero Properties of Sb_2Te_3 65

4.1 Introduction 65
4.2 Epsilon-Near-Zero Phenomena in Metamaterials 65
4.3 Nano-hole Arrays Filled with Chalcogenide Low-epsilon Media 68
4.4 Simulation of Nano-Slot Metasurfaces 70
4.5 Not-So-Extraordinary Transmission: Simulation 71
4.6 Not-So-Extraordinary Transmission: Experimental 80
4.7 Summary 83

Chapter 5 Reconfigurable Ultraviolet and High-Energy-Visible Dielectric Metamaterials 85

5.1 Introduction 85
5.2 Low Index Enabled Reconfigurable Metamaterials 85
5.3 Results and Discussion 95
5.4 Summary 96

Chapter 6 Conclusions and Future Work.....99

6.1 Conclusions 99
6.1.1 Chalcogenide Semiconductor Alloys for Photonic Applications 99
6.1.2 Plasmonic and Phase Change Properties of Bi:Te for Metamaterials Application 101
6.1.3 Epsilon-Near-Zero Properties of Sb_2Te_3 102
6.1.4 Reconfigurable Ultraviolet and High-Energy-Visible Dielectric Metamaterials 103
6.2 Future Work 104

Appendix A Tools and Techniques 107

A.1 Deposition Techniques 107

A.2 X-Ray Diffraction 108

A.3 Raman Spectroscopy 110

A.4 Energy Dispersive X-Ray Spectroscopy 112

A.5 Ellipsometry 113

A.6 FIB Fabrication 117

A.7 CRAIC Microspectrophotometer 118

A.8 Computational tools: Comsol and Lumerical 119

Appendix B BST Ternary Maps 121

B.1 XRD Maps 121

B.2 Raman Maps 124

B.3 Optical Properties Maps 125

Bibliography 129

List of Publications 145

List of Tables

Table 2.1: Summary of literature data extracted from Raman spectra of elemental crystals of Bi, Sb, Te, compound crystals of Bi_2Te_3, Sb_2Te_3, Bi:Sb alloys and their corresponding solid solutions $(Bi_{(1-x)}Sb_x)_2Te_3$ $(0 < x < 1)$ [91, 97-102]. 32

Table 4.1: Lorentzian oscillator model parameters values for the fitting to ellipsometric data for the relative permittivity of amorphous Sb_2Te_3 and the modified permittivity datasets shown in Figure 4.10a and b. 79

List of Figures

Figure 1.1: Materials map for plasmonic media that could be suitable candidates to fabricate low loss metamaterials. 5

Figure 1.2: Examples of all-dielectric metamaterials from visible to mid-IR. 7

Figure 1.3: Examples of chalcogenide phase change functional metamaterials. 10

Figure 2.1: Low kinetic barrier to materials phases of HT-PVD compared to traditional fabrication methods like sequential deposition, ball milling and 'shake and bake'. 17

Figure 2.2: High-throughput schematic of deposition system [47]..... 18

Figure 2.3: Dielectric properties of BST compounds vs Lorentz oscillator model of optical response. 19

Figure 2.4: Frequency dependence of ε_1 and ε_2 calculated from the Lorentz oscillator model. 21

Figure 2.5: ε_2 behaviour at the crossover point. 22

Figure 2.6: Schematic of the apparatus used for physical vapour deposition of ternary compositional gradient thin BST films..... 23

Figure 2.7: Compositional spread covered in this work for the BST system measured by EDX. 25

Figure 2.8: Ternary compositional map of the phases for as-deposited BST thin films..... 27

Figure 2.9: a) XRD diffractograms for selected compositions (shown in panel b) that are in the amorphous phase as deposited. 27

Figure 2.10: Ternary compositional map showing selected compositions grouped along Te tie-lines according to similar features on their corresponding diffractograms. 27

Figure 2.11: XRD diffractograms for selected compositions along Te tie-lines of the BST ternary space. 28

Figure 2.12: XRD diffractograms in a) and corresponding Raman spectra in b) for selected compositions along Te tie-line of the BST ternary space (orange group in Figure 2.10). 29

Figure 2.13: XRD diffractograms in a) and corresponding Raman spectra in b) for selected compositions along Te tie-line of the BST ternary space (red group in Figure 2.10). 30

Figure 2.14: XRD diffractograms in a) and corresponding Raman spectra in b) for selected compositions along Te tie-line of the BST ternary space (green group in Figure 2.10). 31

Figure 2.15: XRD diffractograms in a) and corresponding Raman spectra in b) for selected compositions along Te tie-line of the BST ternary space (blue group in Figure 2.10). 32

Figure 2.16: a) Resistivity obtained by combining 4 point probe (sheet resistance) and thickness measurements as a function of composition with corresponding resistivities along the indicated tie-line shown in b). 34

Figure 2.17: Compositional variation in spectral dispersion of BST optical properties. 35

Figure 2.18: ε_1 = 0 properties of BST. 37

Figure 2.19: Optical properties of BST at telecoms wavelengths. 38

Figure 2.20: Performance of BST alloys for supporting propagating surface plasmon polaritons. 40

Figure 2.21: Performance of BST alloys for supporting localized, spherical nanoparticle surface plasmons. 41

Figure 2.22: Performance of BST alloys as high-index dielectric media. 42

Figure 2.23: Propagation lengths at the excitation light wavelength of 520 nm calculated for an insulator-metal-insulator waveguide 42

Figure 2.24: Numerically simulated optical response of plasmonic subwavelength period nano-grating metasurfaces of varying composition. 43

Figure 2.25: Numerically simulated optical response of all-dielectric subwavelength period nano-grating metasurfaces of varying composition. 43

Figure 3.1: UV and visible plasmonics in amorphous Bi:Te. 48

Figure 3.2: Amorphous bismuth telluride metasurfaces. 49

Figure 3.3: Composition and structural phase of vapour deposited Bi:Te thin films. 50

Figure 3.4 Optical response of amorphous Bi:Te nano-grating metasurface. 51

Figure 3.5: Metasurface resonances at off-normal incidence. 52

Figure 3.6: Structural tuning of amorphous Bi:Te metasurface resonance wavelength. ... 53

Figure 3.7: Compositional tuning of Bi:Te optical properties. 54

Figure 3.8: Optical response of amorphous Bi:Te nano-grating metasurfaces across different compositions. 55

Figure 3.9: Structural properties of as-deposited combinatorial Bi:Te film for representative compositions. 57

Figure 3.10: Structural properties of furnace annealed combinatorial Bi:Te film for representative compositions. 58

Figure 3.11: Dispersion of optical properties of as-deposited and furnace annealed combinatorial Bi:Te film for representative compositions. 59

Figure 3.12: ENZ properties of combinatorial Bi:Te film vs composition. 60

Figure 3.13: Plasmonic properties of combinatorial Bi:Te film vs composition. 61

Figure 3.14: Dielectric properties of combinatorial Bi:Te film vs composition. 62

Figure 3.15: Phase change properties of Bi:Te nano-gratings metasurfaces. 63

Figure 4.1: Geometry of a generic 2D waveguide structure with an ENZ material section. 67

Figure 4.2: Different approaches explored to achieve structures exhibiting near-zero parameters. 68

Figure 4.3: UV/visible plasmonic and ENZ properties of amorphous antimony telluride. . 70

Figure 4.4: Aluminium nano-slot metasurface modelling. 71

Figure 4.5: Spectral dispersion of reflection and transmission for a metasurface, of period P = 100 nm and w = 10 nm, with empty and Sb_2Te_3-filled slots 72

Figure 4.6: Comparison of electric field distribution between empty and Sb_2Te_3-filled slots. 73

Figure 4.7: Optical spectra through aluminium nano-slot metasurfaces across geometrical parameters. 74

Figure 4.8: Optical spectra through aluminium nano-slot metasurfaces across different channel shapes. 74

Figure 4.9: ENZ channel acceptance angle. 75

Figure 4.10: Reduction of losses in ENZ channels. 76

Figure 4.11: Reduction of losses in low-epsilon composite metasurfaces. 77

Figure 4.12: Refractive index of antimony telluride and reduced-loss variants. 78

Figure 4.13: Comparison of electric field distribution for different values of ε_2. 79

Figure 4.14: Schematic of the aluminium nano-slit array metasurface realized experimentally. 80

Figure 4.15: Fabrication steps for the realization of Sb_2Te_3 filled nano-slits metasurfaces: . 81

Figure 4.16: Spectral dispersion of transmission measured experimentally in a) and simulated via FDTD method (Lumerical) in b) for empty nano-slits metasurfaces (red curves), nano-slits metasurfaces filled with Sb_2Te_3 (blue curves) and unstructured Al film (black curves). 82

Figure 4.17: Optical and SEM images of the aluminium nano-slit array metasurfaces realized experimentally. 83

Figure 5.1: UV-high-energy visible (HEV) refractive index (real part) comparison between a selection of chalcogenides and noble metals (Al [109], Ag and Au [107]). 86

Figure 5.2: Reconfigurable UV-HEV all-dielectric metamaterials. 87

Figure 5.3: UV-High energy visible optical properties of GST and BST. 88

Figure 5.4: Numerically simulated reflection spectra for low index enabled reconfigurable metasurfaces based on $BiSb_5Te_9$ (a) and $Ge_2Sb_2Te_5$ (b) in their corresponding amorphous (blue curves) and polycrystalline states (red curves). 89

Figure 5.5: Optical properties of of ZnS/SiO_2–GST metamaterials..... 91

Figure 5.6: Numerically simulated optical response of hybrid chalcogenide phase-change medium / transparent dielectric metamaterials. 93

Figure 5.7: Potential of low index enabled metasurfaces. 94

Figure 5.8: a) Numerically simulated reflection spectra for low index enabled metasurfaces based on a hypothetical layer characterized by a constant *n* with varying *κ* sandwiched between two films of ZnS/SiO_2. 95

Figure 5.9: Distributions of the normalized electric field, *E* in the yz-plane for subwavelength nanogratings with period 300 nm 96

Figure 6.1: Dielectric function of amorphous BST (composition: Bi 17%, Sb 47%, Te 36%) retrieved from ellipsometry assuming a material structure consisting of a bulk semiconductor with a thin metal film on top; 105

Figure A.1: Representation of diffraction from a stack of *xy* atomic planes in the real space a) and in the reciprocal space b) (adapted from [90]). 109

Figure A.2: Schematic of the principle of energy dispersive x-ray spectroscopy (EDX) in the scanning electron microscope (SEM). 113

Figure A.3: The general principle in ellipsometry: interaction of polarized light with a sample (adapted from [198]). 116

Figure A.4: Schematic representation of the interaction of light with a thin film sample on top of a substrate. 117

Figure A.5: General diagram of a microspectrophotometer in transmission a) and reflection mode b). 118

Figure B.1: Intensity plot of the x-ray signal at a certain selected 2θ angle (in degrees) mapped to the corresponding chemical composition. 121

Figure B.2: Intensity plot of the x-ray signal at a certain selected 2θ angle (in degrees) mapped to the corresponding chemical composition. 122

Figure B.3: Intensity plot of the x-ray signal at a certain selected 2θ angle (in degrees) mapped to the corresponding chemical composition. 123

Figure B.4: Intensity plot of the Raman signal at a certain selected Raman shift (in cm^{-1}) mapped to the corresponding chemical composition. 124

Figure B.5: Intensity plot of the Raman signal at a certain selected Raman shift (in cm^{-1}) mapped to the corresponding chemical composition. 125

Figure B.6: Intensity plot of the Raman signal at a certain selected Raman shift (in cm^{-1}) mapped to the corresponding chemical composition. 125

Figure B.7: Figure of merit for localized surface plasmon resonances (LSPR), defined as F_2 in Eq. (2.16), mapped to the corresponding chemical composition in the UV (253 nm and 350 nm), visible (550 nm) and near-IR (900 nm) spectral range. 126

Figure B.8: Figure of merit for low-loss propagating light waves, defined as F_3 in Eq. (2.17), mapped to the corresponding chemical composition at telecom wavelengths, i.e. 1310 nm (on the left) and 1550 nm (on the right). 127

List of Acronyms

Bi_2Te_3	Bismuth Telluride
BST	Bismuth-Antimony-Tellurium
CMOS	Complementary Metal Oxide Semiconductor
EDX	Energy Dispersive X-ray
ENZ	Epsilon-Near-Zero
FDTD	Finite Difference Time Domain
FIB	Focused Ion Beam
GST	Germanium-Antimony-Tellurium
HEV	High-Energy Visible
HT-PVD	High-Throughput Physical Vapour Deposition
IR	Infrared
LSPR	Localized Surface Plasmon Resonances
PEC	Perfect Electric Conductor
PVD	Physical Vapour Deposition
Q	Quality Factor
Sb_2Te_3	Antimony Telluride
SEM	Scanning Electron Microscopy
SPPs	surface plasmon polaritons
TCOs	Transparent Conductive Oxides
TE	Transverse Electric
TiN	Titanium Nitride
TIs	Topological Insulators
TM	Transverse Magnetic

UHV	Ultra High Vacuum
UV	Ultraviolet
XRD	X-ray Diffraction
ZnS/SiO_2	Zinc Sulphide/Silicon Dioxide

Research Thesis: Declaration of Authorship

Print name:	Davide Piccinotti

Title of thesis:	Chalcogenide Platforms for Photonic Metamaterials

I declare that this thesis and the work presented in it are my own and has been generated by me as the result of my own original research.

I confirm that:

This work was done wholly or mainly while in candidature for a research degree at this University;

Where any part of this thesis has previously been submitted for a degree or any other qualification at this University or any other institution, this has been clearly stated;

Where I have consulted the published work of others, this is always clearly attributed;

Where I have quoted from the work of others, the source is always given. With the exception of such quotations, this thesis is entirely my own work;

I have acknowledged all main sources of help;

Where the thesis is based on work done by myself jointly with others, I have made clear exactly what was done by others and what I have contributed myself;

Parts of this work have been published (see the list of publications at the end).

Signature:		Date:	

Acknowledgements

I would like to thank Prof. N. I. Zheludev that offered me the opportunity to join his research group and for his inspiration, supervision and his feedback, though sometimes tough, always helpful and insightful that gave me a deeper understanding of my research.

I would like to thank Prof. K. F. MacDonald for his supervision, assistance and his continuous availability during my Ph. D studies.

I would like to offer my special thanks to Dr. B. Gholipour for his supervision, great support, his strong motivation and his invaluable help in the laboratory work throughout my Ph. D studies.

I would like to thank Prof. B. E. Hayden for the useful discussions and for giving me access to the high-throughput deposition facilities.

I would like to thank Dr. J. Yao for training me on the high-throughput deposition facilities and his precious advice.

I would like to thank Dr. J. Ou for his patience and help on setting up the optical measurements.

I would like to thank Dr. A. Karvounis that first introduced me in this group and helped me throughout my Ph. D studies with useful comments and suggestions.

I would like to thank all the members of the Nanophotonics and Metamaterials group who supported me during my research studies.

I would like to thank my office mate Marcelo for all the useful discussions about the optical fibres.

I would like to thank all the friends that I met in Southampton, with special thanks to Ilaria and Francesco, and my friends at home.

I would like to thank Angela, the most important person that I met during my Ph. D.

Undoubtedly, the biggest thanks is for my family: my parents, my brother and my beautiful nephew and niece.

Chapter 1

Introduction

Nowadays, our society rely on light-based technologies known as photonics, since photons, quanta of light, has become the major information carrier and manufacturing tool of the 21st century. Indeed, one cannot imagine modern life without telecommunication networks, data storage and modern display technologies. Our reliance on these technologies has created an ever-increasing global demand for compact, power efficient computational power and data storage. Different technologies can be used to control the light such as silicon photonic-based devices, fibre optics and metamaterials. In particular, optical metamaterials, artificial media structured in such a way that they exhibit exceptional electromagnetic properties not readily observed in nature [1], offer a highly compact and novel technological solution for controlling light at the nanoscale with the potential to facilitate advancement in many areas of fundamental and applied science and technology, including imaging with lenses, telecommunications and sensing [2-4]. Conventional lenses have an imaging resolution that is limited by diffraction, however metamaterials enabled the development of "superlenses" [5] that can go beyond this limit and could have a great potential in applications such as biomedical imaging, optical lithography and data storage. Moreover, 2-dimensional metamaterials (also called metasurfaces) have enabled the recent development of flat, ultrathin optical components giving rise to the so-called 'flat optics' technologies that provide new functionalities, increase design freedom in correcting aberrations, achieve high scattering efficiency and broadband performance and reduction in system size and weight compared to conventional optical components [6]. The integration of metamaterials with fibre optics could give the opportunity to develop novel optical components such as lenses, beam splitters and optical modulators inside the fibre resulting in low-cost, potentially high-speed optical switching and modulation that could help to avoid the expected capacity shortage in telecommunication networks [7]. Additionally, the dependence of the resonant spectral response of metamaterials on the surrounding environment could be suitable for sensing purposes [8].

Originally created for achieving extraordinary electromagnetic response in passive media (e.g. negative refraction, giant chirality, terahertz magnetism and subwavelength switches [9, 10]), plasmonic metamaterials have been conventionally made out of noble metals such as Au, Ag, Al or Cu [11]. Such metals suffer from high-energy dissipation due to Ohmic losses, particularly in the near-infrared (IR) to visible spectral range, which compromise some applications [12, 13]. Furthermore, the metamaterial paradigm was recently extended from passive devices to functional metamaterials or metadevices where active tunability and switching of electromagnetic characteristics of metamaterials are aimed [14]. Therefore, the development of new material platforms beyond noble metals is nowadays a crucial research topic [15-17]. Investigations have variously encompassed conductive oxides, nitrides [18], superconductors [19] and graphene[20], to name but a few [21]. Among candidate materials, chalcogenides (alloys containing at least one of the 'chalcogen' elements sulphur, selenium or tellurium) are promising, because they offer compositionally controlled ultra-wide transmission windows and can combine multiple functionalities like nonlinear properties, memory function and switchability in the same metadevices [14, 22].

1.1 Photonic Metamaterials

Metamaterials offer the capacity to manipulate light deep into the subwavelength regime and give rise to resonant wave-matter interactions responsible for the exotic and striking properties observed for this class of artificial materials [15]. In general, metamaterial designs typically consists of scattering elements arranged or patterned periodically [23]. In this way, it is possible to define a unit cell that is essentially a resonator designed to couple and interact with the free-space propagating wavelength. These resonators are subwavelength, namely their size is smaller than the wavelength of interest and are usually called meta-atoms or meta-molecules. In a basic view, an incident wave induces oscillating currents in the metamaterial and these resonators re-radiate electromagnetic waves. The meta-atoms behave as a little antenna and resonance conditions can be obtained for certain shape and size of resonators. At the resonance electrical currents are strongly coupled to the incident field and can be amplified to very high values. Therefore, amplified currents ensure strong response of the metamaterial at the resonance frequency, for instance strong magnetism. Since the unit cell size is subwavelength, a metamaterial can be described by using an effective permittivity and permeability that are functions of some geometrical parameters, i.e. size, height and width of the unit cell. Hence, by using specific shape and size for the resonators is possible to achieve either electric or magnetic response or even both simultaneously. This concept enabled the realization of the first metamaterial with negative

refractive index [24]. Apart negative refraction, resonances in metamaterials can be used for subwavelength-focusing, cloaking, wave-front-shaping and for obtaining perfect absorption [25].

Initial experiments on metamaterials were carried out in the microwave range and the first metamaterials were made of noble metals, because in this spectral range metals are good conductors and they can support strong electrical currents that are necessary for achieving resonant spectral responses. After that, metamaterial's research has expanded toward near-infrared and visible spectral ranges, since by scaling down the metamaterial unit cell, resonances can be moved to shorter wavelengths [26]. However, the implementation of optical or photonic metamaterials is challenging, because at optical frequencies electrical currents are replaced with surface plasmon polaritons which require a different design of metamaterials. Moreover, metals, even silver and gold that have very high conductivities, are characterized by high losses at optical frequencies that provide high absorption spectral responses. This behaviour is useful for several application ranging from photo-detection to solar photo-catalysis [16]. Nevertheless, high material losses affect the realization of many other application such as light sources, detectors, solar cells, interconnects, switches and modulators [16]. Furthermore, the possibility of constitutive materials with active tunability and switching of electromagnetic characteristics would enable the extension of metamaterial paradigm from passive devices to functional metamaterials or metadevices increasing even further the potential impact of metamaterials [14].

In general, metamaterials can be classified in plasmonic and all-dielectric metamaterials, according to the optical properties of the constitutive materials.

1.1.1 Plasmonic Metamaterials

The first approach to obtain a metamaterial is related to the use of plasmonic materials, namely substances with a negative real permittivity (ε_1) that is indispensable to support surface plasmon polaritons, i.e. coupled excitations of a free electrons gas with electromagnetic fields [27]. In fact, plasmons provide the mechanism for harvesting light from free space and confining it to nanoscale volumes realizing intense electromagnetic field concentration beyond the diffraction limit, an essential feature of metamaterials [16, 28]. Specifically, surface plasmon polaritons are waves that propagate at the interface between two materials where the real part of the dielectric function changes sign across the interface, typically a metal/dielectric boundary [29]. Despite their propagating nature, the subwavelength structure and periodicity of metamaterial unit cells induces a confinement of

these modes and so they are called localized surface plasmon polaritons. The optical properties of plasmonic metamaterials are related to the excitation of these modes by the incident electromagnetic field. Indeed, the ability to trap and confine light of localized surface plasmon polaritons gives rise to subwavelength effects and by the excitation of specific modes an optical response characterized by strong resonances can be obtained. Since the resonant frequencies are determined by meta-molecule size and geometry, their spectral position can be controlled at will if the material is not too lossy in that spectral range. In order to obtain resonances with high-quality (*Q*) factors, losses at the resonant frequency must be low. Otherwise, the energy associated to the incident electromagnetic field is not transferred efficiently to the plasmonic mode since losses mechanism draw off energy causing a damping of the resonance. In particular, losses have two sources: radiative losses and non-radiative losses [30]. In general, the modes excited in metamaterials are strongly coupled with free space radiation that leads to strong scattering and short resonance lifetimes. These are called radiative losses and they can be minimized by a careful design of meta-molecules that enables the excitation of higher order modes characterized by a longer lifetime of the resonance and a corresponding higher quality factor [30, 31]. Instead, non-radiative losses are associated with dissipative processes, i.e. Joule losses due to free conductors in materials. Hence, non-radiative losses are linked essentially to the material used to make a metamaterial.

For these reasons, the choice of the building material for metamaterials is fundamental and currently, since metals suffer from high losses at optical frequencies, the search of new materials is a central topic for plasmonic and nanophotonic applications.

In ref. [32] they have suggested the classification of materials based on three parameters that control the optical properties of conducting materials: the carrier concentration, the carrier mobility and the interband losses (Figure 1.1). A high enough carrier concentration is necessary for providing a negative real permittivity (a fundamental requirement for any plasmonic material) and large carrier mobilities with low interband losses enable the minimization of losses. According with these defined parameters, alkali metals and metallic alloys could be potential candidates to substitute gold and silver in the UV/visible spectral range. In addition to this, high doped semiconductors with wide bandgap could be suitable plasmonic materials for metamaterials and, in particular, titanium nitride is reported as a good candidate for metamaterials fabrication [11]. Instead, other recent materials proposed for plasmonic applications such as nitrides, transparent conducting oxides, graphene and perovskites could be used in the near-IR spectral range. Intermetallics like silicides and germanides and elemental materials such as antimony and bismuth have a lower carrier

concentration and could be used at longer wavelengths (e.g. mid-IR). Despite the optical properties, also fabrication issues should be considered and for example alkali metals are extremely reactive in air ambient environments, hence they have not been used in plasmonic applications regardless of their high quality factors [27].

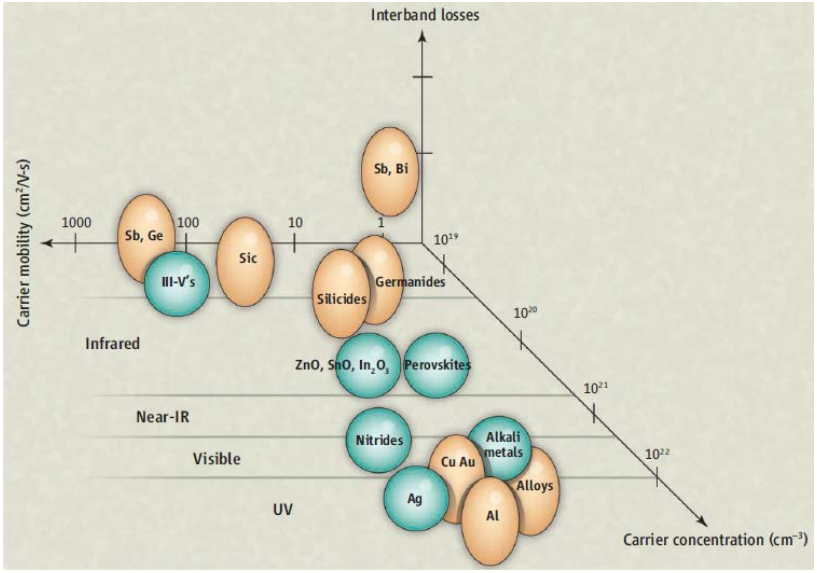

Figure 1.1: Materials map for plasmonic media that could be suitable candidates to fabricate low loss metamaterials. Materials are classified by considering three important parameters such as carrier concentration, carrier mobility and interband losses. Spherical bubbles represent materials with low interband losses and elliptical bubbles denote media with larger interband losses in the respective part of the electromagnetic spectrum [32].

Topological insulators (TIs) represent another class of promising plasmonic materials for the visible and UV parts of the spectrum [33, 34]. These materials have an insulating interior with surface conducting states topologically protected from back-scattering [34]. Therefore, charge carriers from these surface states are less affected by contaminants and defects compared to metals. Moreover, TIs could enable the scaling down of metamaterials to thickness of few nanometres, since these topologically protected states are located on the surface of TIs. Furthermore, a topological insulator semiconductor at optical frequencies has been demonstrated recently at optical frequencies, which is an extremely challenging domain for plasmonics [33].

1.1.2 All-dielectric Metamaterials

Another way to realize metamaterials with low loss is based on the use of dielectrics [35]. In this case, conduction currents are substituted with displacement currents and different microscopic phenomena are involved. An optical resonant response can be obtained by using

dielectric subwavelength structures providing a new class of metamaterials called all-dielectric metamaterials. In fact, dielectric nanoparticles with high permittivity can support electric and magnetic modes of different order that can be excited with electromagnetic waves [36]. The features of these modes can be calculated by using Mie-theory and so they are called Mie-type modes [37]. In general, high permittivity nanoparticles support a first resonance mode that is a magnetic dipole mode and a second resonance that is an electric dipole mode. Resonant frequencies of the particles can be shifted by changing their size and shape; since some dielectric materials such as silicon are characterized by almost complete absence of conductivity currents in optical range, low dissipative losses are generated and high-Q resonances are expected. Similar behaviour to dielectric nanoparticles can be observed also for cubic, disk-shaped or cylindrical objects. These electric and magnetic dipole resonances act as artificial "atoms" which form the basis of all-dielectric metamaterials. Indeed, by arranging a collection of such resonant particles their combined scattering response can act like a material with almost arbitrary values of effective permittivity and permeability [37]. For this class of metamaterials a high permittivity of unit cells is a fundamental feature in order to obtain a subwavelength effect as the wavelength of electromagnetic radiation inside the meta-atoms is reduced by a factor equal to the root square of the permittivity (ε_r) for materials without magnetic activity, i.e. the relative magnetic permeability ($\mu_r = 1$). In fact the wavelength inside a medium (λ) is defined as:

$$\lambda = \frac{\lambda_0}{n} = \frac{\lambda_0}{\sqrt{\varepsilon_r}} \; as \; n = \sqrt{\varepsilon_r \mu_r} = \sqrt{\varepsilon_r} \; (\mu_r = 1, nonmagnetic \; material) \qquad (1.1)$$

Where λ_0 is the free-space wavelength of the electromagnetic radiation and *n* is the refractive index of the medium.

In general, the materials used for the fabrication of all-dielectric metamaterials have two common features, namely they are low-loss media with high refractive index in the range of interest. These qualities minimize absorption losses and ensure that metamaterial unit cells are sufficiently subwavelength in size to avoid diffraction effects [38]. All-dielectric metamaterials have been demonstrated in a wide spectral range – from mid-IR to visible (Figure 1.2) and so far, the main material used is silicon due to its relatively high refractive index associated with low absorption (near-IR and mid-IR) and its feasibility to realize the integration between optical devices and microelectronics since it is the most used material in this industry. Other materials used for all-dielectric metamaterials are germanium [39], tellurium [40] and titanium dioxide (in particular for the visible spectral range) [41-43].

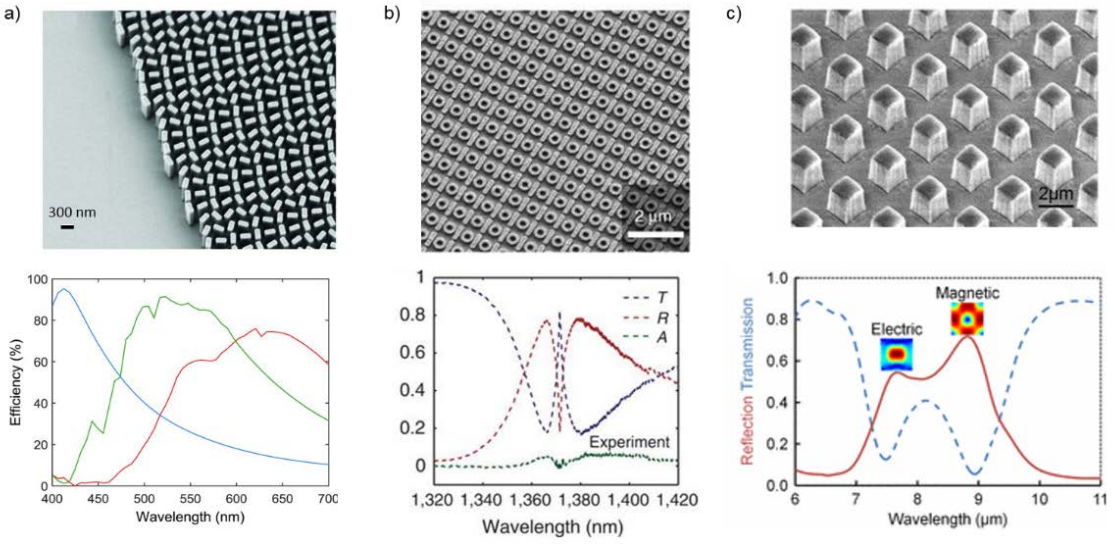

Figure 1.2: Examples of all-dielectric metamaterials from visible to mid-IR. a) Scanning electron microscope (SEM) image of a titanium dioxide metasurface[1] (top) fabricated and designed as metalens working in the visible range and corresponding simulated polarization conversion efficiency as a function of wavelength (bottom) [44]. b) SEM image of an all-dielectric silicon metasurface analogue of electromagnetically induced transparency (top) working in the near-IR and corresponding experimentally measured transmittance, reflectance and absorption spectra (bottom) [12]. c) SEM image of an all-dielectric metamaterial composite in the mid-IR based on micron-sized, high-index tellurium dielectric resonators and corresponding reflection and transmission spectra (bottom) [40].

In summary resonances in the plasmonic and dielectric structures have a considerably different nature; the former requires the excitation of surface plasmon polaritons while in the latter dielectric Mie-modes are involved. Because of the low-loss feature, all-dielectric metamaterials considerably exceed plasmonic metamaterials in efficiency and resonance quality factor, since losses cannot be eliminated completely in plasmonic nanostructures [45]. However, plasmonic metamaterials have tighter field confinement, broader bandwidth and smaller device footprint. In particular, the ability to strongly confine the electromagnetic field can be useful in many application like colour filtering, enhanced harmonic generation, improved nonlinearity, detection sensitivity improvement, perfect absorption, efficient thermal emission, photocatalysis, and high-temperature applications such as thermo-photovoltaics, heat-assisted magnetic recording, etc. [45].

[1] A metasurface or planar metamaterial is a 2-dimensional metamaterial.

1.1.3 Chalcogenide Functional Metamaterials

The realization of low-loss metamaterials can extend the range of application of metamaterials; however the possibility of constitutive materials with active tunability and switching of electromagnetic characteristics enables the extension of metamaterial paradigm from passive devices to functional metamaterials or metadevices increasing even further the potential impact of metamaterials [14]. Hence, substantial efforts are now focused on achieving tunable, switchable, nonlinear and sensing functionalities [14]. However, conventional metals used for metamaterials such as Au, Ag, Al or Cu [11] possess optical properties that are neither compositionally adjustable nor particularly responsive to external excitations[15]. Therefore, the development of new material systems beyond noble metals is nowadays a crucial research topic [15].

Many alternatives are being explored such as conductive oxides, nitrides, superconductors, graphene and other 2D materials and among them chalcogenides (binary and ternary sulphides, selenides and tellurides) are promising, because they can combine multiple functionalities like nonlinear properties, memory function and switchability in the same metadevices [14, 22]. Indeed, they are one of the more versatile material system showing high-index dielectric, epsilon-near-zero, topological insulator and plasmonic behaviour depending on composition and spectral range. In addition to that, they can be reversibly switched (electrically or optically) in a non-volatile fashion and they are also thermoelectric materials. Most of these properties are compositionally tunable [34, 46] and in order to explore the relationships between properties and composition, high-throughput methodology is used. This method consists on coevaporation of pure elements for the synthesis of solid-state material combinatorial libraries and further parallel characterization to optimize the synthesis for specific applications [47]. This will be described extensively in Chapter 2.

Chalcogenides have long been recognized in the field of optics and photonics for their exceptional transparency at IR wavelengths (far beyond the low-loss transmission range of silica or heavy oxide glasses) and as highly optically nonlinear materials [48]: the near- to mid-IR spectral range encompasses important atmospheric windows (3-5 μm and 8-12 μm) and the molecular fingerprints of numerous (bio)chemicals, e.g. greenhouse gases, water pollutants, and pharmaceuticals, presenting a wealth of sensing, light-guiding and imaging applications. Chalcogenides are known for the magnitude of their intrinsic third-order optical nonlinearities, and present some of the largest known nonlinear figures of merit ($F = n_2/\beta\lambda$, where n_2 is nonlinear refractive index, β is the two-photon absorption coefficient and λ is

wavelength) at telecoms wavelengths, making them extremely attractive for ultrafast, low-power all-optical signal processing and efficient wavelength conversion applications.

Moreover, the absorption of electromagnetic radiation in chalcogenides can produce photo-induced changes in their properties as a result of photoillumination [49]. Some of the most common and useful forms of photoinduced changes in chalcogenides are [49-52]:

- Photocrystallization [53] or amorphization [54]
- Photopolymerization [55]
- Photocontraction or expansion [56]
- Photo-vaporisation [57]
- Photodissolution of metals [58]
- Photodarkening [59]
- Photobleaching [59]
- Photoinduced anisotropy [60, 61]

In particular, the photocrystallization or amorphization property has been the basis for rewritable optical data storage technologies (i.e. CD, DVD and Blu-ray discs), and more recently developed electronic (random access) memory and memristor devices [62, 63], all of which exploit their unique capacity for fast, reversible, non-volatile switching between amorphous and crystalline states with markedly different properties (refractive index, resistivity, etc.). It has been observed of chalcogenides that they are "perpetually underestimated in terms of their practical potential" [64] and indeed they have much to offer in the domain of plasmonics.

Chalcogenide glasses were first suggested in 2010 as active dielectric media for plasmonic switching [65], whereby changes in the real and/or imaginary part of their refractive index induced by an external control excitation (optical, thermal, electronic, etc.) at an interface with a noble metal would switch or modulate the surface plasmon propagation or resonance characteristics of the interface. A variety of chalcogenide phase-change active plasmonic and photonic metamaterial devices, for potential applications including electro- and all-optical signal switching, polarization modulation, beam steering and active focusing, nanophotonic memory, tunable optical filters, and multispectral imaging, have since been computationally analysed and experimentally demonstrated. A few examples of chalcogenide phase change functional metamaterials are reported in Figure 1.3: so far, the most used chalcogenide material is germanium antimony telluride (Ge:Sb:Te or GST) which was widely exploited in rewritable optical disk storage technology and non-volatile electronic memories due to its good thermal stability, high switching speed and large number of achievable rewriting

cycles [22]. When GST is combined with other plasmonic nanostructured materials, it enables the tuning of the metamaterial resonance frequency, because GST dielectric permittivity changes significantly between the amorphous and the crystalline phase (Figure 1.3). Recently, it was also shown that metamaterials can be fabricated directly on GST films and these metamaterials support resonances (without the help of other plasmonic or dielectric materials) in the near-IR that can be spectrally shifted by optically-induced crystallization which are able to deliver reflection and transmission switching contrast ratios up to 5:1 (7 dB) [66].

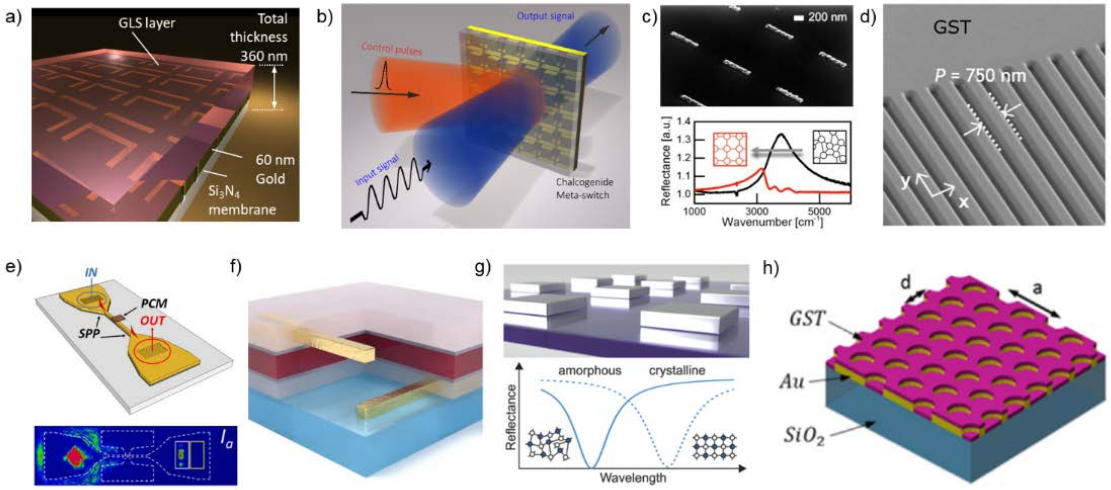

Figure 1.3: Examples of chalcogenide phase change functional metamaterials. a) Artistic impression of a hybrid device structure comprising a planar gold plasmonic metamaterial on a silicon nitride membrane, covered with GLS (gallium lanthanum sulphide) chalcogenide glass, that demonstrate the concept of nanoscale electro-optic switching [67]. b) All-optical, non-volatile, chalcogenide glass metamaterial switch based on a GST (germanium antimony telluride) film [68]. c) SEM image of aluminium nanoantennas (top) on top of a GST layer used for tuning the resonance frequency of the nanoantennas (bottom) in the mid-IR [69]. d) All-chalcogenide nano-grating metasurface, oblique incidence scanning electron microscopy image of a 750 nm period grating fabricated by focused ion beam milling in a 300 nm thick amorphous GST film on silica [66]. e) Plasmonic waveguide with a GST strip in the middle for the active control of the propagation of surface plasmon polaritons at an Au/SiO_2 interface [70]. f) Tunable and switchable mid-IR plasmonic chiral metamaterial enabled by GST that is thermally actuated [71]. g) Switchable perfect absorber device consisting of an array of square aluminium nano antennas stacked above a GST spacer layer and an aluminium mirror [72]. h) Au extraordinary optical transmission nanostructures combined with GST for ultrafast and broadband tuning of resonances [73].

Moreover, chalcogenides can themselves be plasmonic materials in the optical domain: $Bi_{1.5}Sb_{0.5}Te_{1.8}Se_{1.2}$ (BSTS) is one of several chalcogenide crystalline compositions noted as topological insulators (TIs) – semiconductors with topologically-protected metallic surface states arising through strong spin-orbit interactions. It has been shown recently [33], via the observation of nanostructurally engineered plasmonic metasurface resonances in the

350-550 nm spectral range, that single-crystal BSTS is also a good plasmonic material in the blue-UV domain – these properties being attributed to a combination of bulk charge carriers from inter-band transitions and surface charge carriers in a nanoscale topologically-protected surface layer. Other chalcogenide compositions (including Bi:Te, Sb:Te and Bi:Sb:Te) can be plasmonic in both amorphous and polycrystalline form over a UV/visible/near-IR spectral range that depends strongly on chemical composition [74], as will be discussed in what follows.

Finally, the spectral dispersion of their relative permittivity ε is such that many chalcogenides are so-called "epsilon-near-zero" (ENZ) media, i.e. have values of $\varepsilon_1 \approx 0$, at certain (again compositionally-controllable) wavelengths. Such materials can provide for a variety of unusual and intriguing electromagnetic wave and light-matter interaction phenomena and this will be described in more details in section 4.2. However, levels of absorption in natural ENZ systems has thus far made the observation of such effects at optical frequencies impossible. Chalcogenides may offer a solution [74] and this will be the subject of Chapter 4.

1.2 Motivation and Project Aim

Light-based technologies known as photonics have revolutionized our society in many aspects and numerous applications such as displays, laser surgery, manufacturing, metrology and security services all depend upon our ability to master light. The improvement of performance of all light-enabled devices necessitates the control of light at nanoscale with only few technologies available so far. Among them, metamaterials can offer a highly compact and novel technological solution for the realization of all-optical devices; in fact, metamaterials have seen a spectacular growth from the early days when research was focused mainly on double negative refractive index phenomena [75]. Nowadays the field of metamaterials embraces many new research areas and metamaterials approach enables a progressive understanding of the wave-matter interaction and our ability to artificially manipulate it, specifically at small length scales [15]. Despite the large variety of phenomena observed with metamaterials, there are still open issues related to their efficiencies. In particular, noble metals that are the most used plasmonic materials suffer from high losses in the optical spectral range and usually lack active tunability needed for switching the electromagnetic characteristics of metamaterials. This highly motivates the search for better materials that can support optical resonances with subwavelength confinement and can also combine multiple functionalities like nonlinear properties, memory function and switchability in the same device [14, 22].

On the other hand, the discovery and development of new materials is a time consuming and a highly empirical task [76], since the connection between the material functionalities with its chemical structure and microstructure is not always straightforward. For this reason, combinatorial and high throughput methodologies that were initially implemented in the pharmaceutical industry have been adapted for the purposes of materials science and they have been used here to explore chalcogenides as a new material system to manufacture metamaterials in the UV-visible and near-IR spectral range.

1.3 Thesis Synopsis

The structure of this thesis is organized in six chapters. In the first chapter, a general overview of the main topics faced during my PhD project is given together with the motivation and project aim.

Chapter 2 gives a general introduction of the combinatorial and high-throughput methodology highlighting how this approach has enabled a significant acceleration of research and development through parallel synthesis and characterization of solid-state material libraries. This method is applied here for the exploration of novel material platforms in order to overcome the limitations of traditional plasmonic metals and develop new functional metamaterial devices. In this context, chalcogenides—alloys based upon chalcogen elements (sulphur, selenium and tellurium) present a variety of technologically useful compositionally tunable properties and therefore are of enormous interest in the field of nanophotonics. Here, using the bismuth antimony telluride (BST) chalcogenide family, I show that combinatorial high-throughput mapping techniques allow the entire compositional space of a given compound to be systematically explored for optical, plasmonic and epsilon-near-zero properties across UV to IR wavelengths. This presents an ultra-fast method of optimization/exploration of complex compounds for a variety of tailor-made nanophotonic applications.

Chapter 3 discusses the optical and phase change properties of Bi:Te, one of the corresponding binary alloys of BST. In particular, I show that amorphous thin films of Bi:Te exhibit a plasmonic response at near-UV to visible frequencies, with the real part ε_1 of its relative permittivity taking a negative values over a composition-dependent range of wavelengths extending from as low as 250 nm to as high as 978 nm. We demonstrate this plasmonic response via the fabrication and characterization of planar metamaterial structures. Moreover, we study also the phase change properties of this alloy, namely the

change of optical properties related to the phase transition from amorphous to crystalline phase as a function of composition.

Chapter 4 focuses on the epsilon-near-zero (ENZ) properties of the Sb:Te binary alloy, since this material presents a UV-visible ENZ point with relatively low loss for some specific compositions. At the beginning of the chapter a general overview of ENZ phenomena in metamaterials is provided; then, we consider the case of an array of subwavelength apertures in a metal film filled with a low-epsilon medium at optical frequencies (Sb_2Te_3) where an increase in transmission over a broad range of plasmonic frequencies is observed, and found to be enabled by "laminar" flow of energy through the chalcogenide inclusions. For a low-epsilon medium with causality-bound dispersion of the real and imaginary parts of relative permittivity, a peak in transmission emerges at the wavelength of unity refractive index as losses decrease, while counterintuitively the absorption of the composite structure increases. After presenting the simulation of nano-slots metasurfaces, we describe the corresponding experimental realization by using a slightly different metasurface design, namely we fabricated an array of elliptical nano-slits instead of nano-slots.

In chapter 5, we explore the optical properties of BST and GST (germanium antimony telluride, $Ge_2Sb_2Te_5$) in order to implement reconfigurable metamaterials operating from UV to high-energy-visible (HEV) frequencies. This class of metamaterials would benefit applications in sensing, high-density optical memory, beam-steering, adaptive optics and light modulation**.** In particular, we demonstrate for the first time a non-volatile switchable dielectric metamaterial operating in the UV-HEV spectral range. Nano-grating metamaterials in a layered composite of low-loss ZnS/SiO_2 and the chalcogenide phase-change medium GST exhibit reflection resonances at UV-HEV wavelengths that are substantially modified by light-induced (amorphous-crystalline) phase transitions in the chalcogenide layer. Despite the presence of the lossy GST, resonance quality factors up to $Q \approx 15$ are ensured by the transparency (low losses) of ZnS/SiO_2 in the UV-HEV spectral range and values of Q increase as the refractive index of $Ge_2Sb_2Te_5$ decreases, upon crystallization. Notably however, this switching leaves resonance spectral positions unchanged.

In chapter 6, conclusions and outlooks for the future research are reported: the main objective pursued in this thesis was the exploration of chalcogenides as a new material platform to manufacture metamaterials in the UV-visible and near-IR spectral range. Specifically, binary and ternary alloys of BST have been investigated showing high-index dielectric, epsilon-near-zero, topological insulator and plasmonic behaviour depending on composition and spectral range. The study of the relationships between properties and composition has been achieved through a high-throughput methodology that consists on

coevaporation of pure elements for the synthesis of solid-state material combinatorial libraries and further parallel characterization to optimize the synthesis for specific applications.

1.4 Summary

Photonics have revolutionized our society in many aspects and numerous applications such as displays, laser surgery, manufacturing, metrology and security services all depend upon our ability to master light. Photonic metamaterials - media artificially structured at the nanometre scale - provide extraordinary optical properties not found in nature that can offer a highly compact and novel technological solution for the realization of all-optical devices. In this work, I explored opportunities provided by changes of complex optical properties of chalcogenide alloys related to compositional variation and structural phase change to develop switchable and tunable plasmonic and dielectric metamaterials.

Chapter 2

Chalcogenide Semiconductor Alloys for Photonic Applications

2.1 Introduction

In this chapter, a general introduction of the combinatorial and high-throughput methodology is given highlighting how this approach has enabled a significant acceleration of research and development through parallel synthesis and characterization of solid-state material libraries. This method is applied here for the exploration of novel material platforms in order to overcome the limitations of traditional plasmonic metals and develop new functional metamaterial devices. In this context, chalcogenides—alloys based upon chalcogen elements (sulphur, selenium and tellurium) present a variety of technologically useful compositionally tunable properties and therefore are of enormous interest in the field of nanophotonics. Here, using the bismuth antimony telluride (BST) chalcogenide family, I show that combinatorial high-throughput mapping techniques allow the entire compositional space of a given compound to be systematically explored for optical, plasmonic and epsilon-near-zero properties across UV to IR wavelengths. This presents an ultra-fast method of optimization/exploration of complex compounds for a variety of tailor-made nanophotonic applications.

2.2 Combinatorial and High-Throughput Methodology

The discovery and development of new materials plays an important role in the technological progress as shown by the way silicon has revolutionized the microelectronics industry. Conventionally, this is a serial process where different compositions are explored in a one-by-one method that can evaluate only one composition at a single time. Hence, historically materials development is considered a time-consuming and a highly empirical task [76] since the connection between the material functionalities with its chemical structure and

microstructure is not always straightforward. However, in the last three decades, an innovative approach has been developed in the pharmaceutical industry in the form of combinatorial chemistry and high-throughput screening [77]. More recently, this method was adapted for the purposes of materials science enabling a significant acceleration of research and development through parallel synthesis and characterization of solid-state material libraries, namely a large number of compounds with different compositions are synthesized and characterized together in parallel [46, 47, 77-79]. This approach has a huge versatility and it can be used to tackle materials issues at different levels in a plethora of topics going from catalytic powders and polymers to electronic and biofunctional materials [77]. The combinatorial approach to solid-state applications has proven to be effective and successful by the discovery of new compounds in crucial technological fields like optical, dielectric and magnetic materials [77]. Specifically this approach was also applied to the optimization of an important class of photonic metamaterials supporting Fano resonances [80] that became a prime platform for new switching, gain and sensing applications, and slow light and polarization control devices [81]. Despite the obvious advantages of reducing the time and costs necessary to optimize results that are fundamental points for industry applications, combinatorial techniques are very useful in order to address fundamental questions of materials science [77, 79]. In fact, this methodology has a central role in finding new materials phases with enhanced physical properties as well as quickly mapping composition-structure-property relationships in complex material systems [82]. In particular, the application of the combinatorial approach to thin-film synthesis techniques enables the creation of combinatorial libraries and composition spreads [77]. There have been great progresses in this area, specifically in the physical vapour deposition (PVD) for high-throughput (HT) synthesis of solid-state material libraries.

The PVD method for HT synthesis is a process that combines co-evaporation of pure elements from multiple sources on temperature controlled substrates with independently controlled source shutters in ultra high vacuum (UHV) condition [47]. This method enables the synthesis of inorganic thin films made of several different elements for which the composition varies spatially across the substrate. Hence, a range of compositions can be obtained in a single deposition run with only one substrate. Compared to conventional PVD deposition method, the HT-PVD technique has the benefits of speed, simplicity, accurate control of the compositional ranges and the synthesis of wide ranges of composition in non-equilibrium phases. Moreover, this methodology enables the direct synthesis of amorphous phases and control of crystallization, it can be combined with plasma atom source to directly produce

stoichiometric oxides, hydrides and nitrides and can be used to produce more complex compound materials. Furthermore, it has the capability to fabricate supported nano-particles, it is compatible with small MEMS (microelectromechanical systems) array chip screening and provides a high purity material synthesis.

One of the key advantage of HT-PVD approach is the very low kinetic barrier (a kinetic barrier or activation energy is the energy which must be available for a chemical reaction to take place, namely the minimum energy necessary to convert reactants into products) to solid state phase formation (Figure 2.1), namely the as-deposited compositional gradient film is characterized by several metastable states that correspond to different material phases. In this case, the kinetic barriers between the different states are relatively small resulting in the possibility to obtain the corresponding thermodynamical products after a thermal annealing (for instance), even if this phase is not the most stable from thermodynamical considerations (minimum of potential energy). Instead, other traditional fabrication methods like sequential deposition, ball milling[2] and 'shake and bake'[3] produce specific phases already separated by high kinetic barriers that preclude the conversion between different phases.

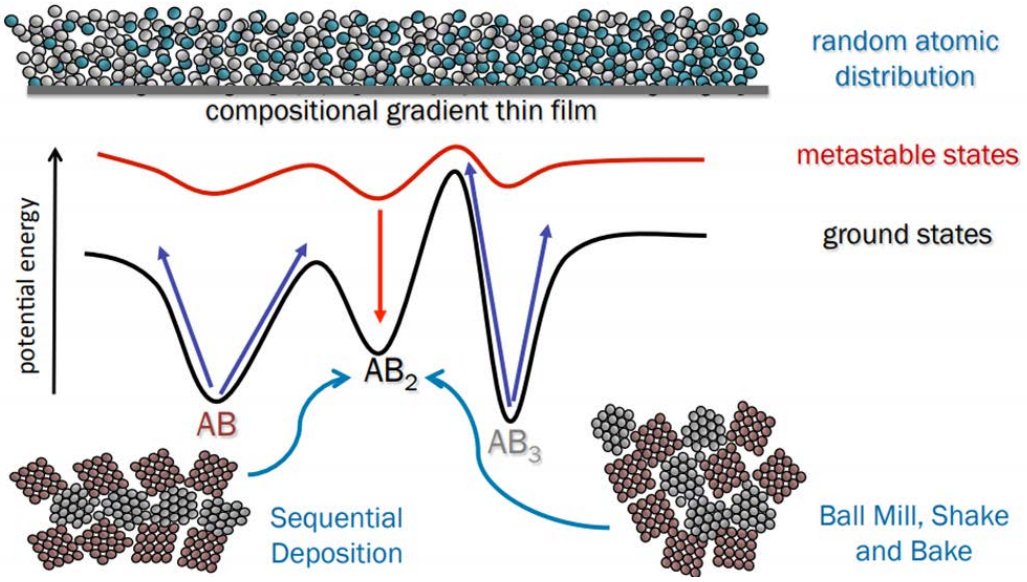

Figure 2.1: Low kinetic barrier to materials phases of HT-PVD compared to traditional fabrication methods like sequential deposition, ball milling and 'shake and bake'.

[2] Ball milling is a top-down process used for the fabrication of nanostructured materials and it consists on using a grinder called ball mill to grind and blend materials.

[3] 'Shake and bake' is a top-down process based on solid state reactions used for the fabrication of nanostructured materials that consists on mixing together powdered reactants and heating them in a furnace for long periods.

The HT-PVD system used in this research project has a base pressure of 1 *x* 10^{-10} mbar and it can be equipped with a maximum of six off-axis sources that could be either electron-beam or Knudsen cells depending on the given source material (a Knudsen cell is a material source based on the principle of molecular effusion used to evaporate material in molecular beam epitaxy). The sources are arranged in 6-fold symmetry and each element can be deposited with a gradient that can be adjusted independently of the other sources. In fact there is a so-called "wedge shutter" for each source which partially shadow the elemental deposition sources and by changing the position of this wedge shutter is possible to produce material fluxes which vary across the substrate (Figure 2.2). By optimising the position of these wedge shutters is possible to control the gradient of the deposition profile [47].

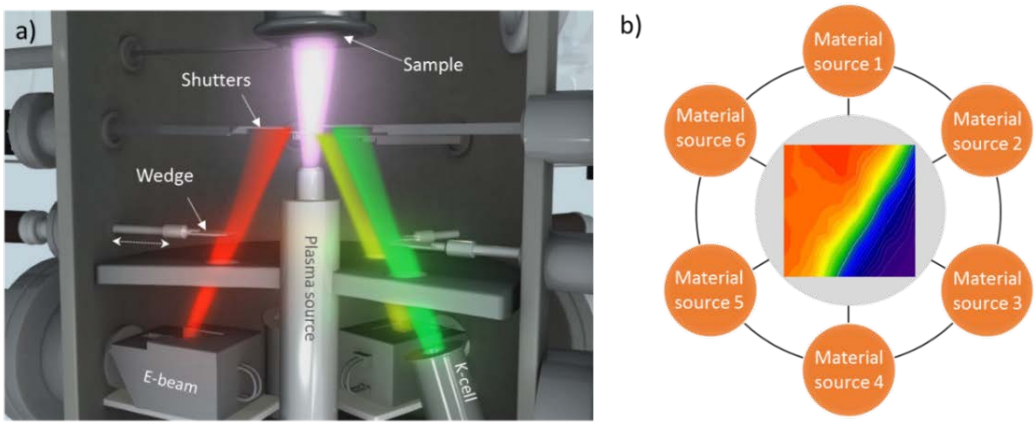

Figure 2.2: High-throughput schematic of deposition system [47]. a) Cross-section of the deposition chamber: material sources (e-beam and K-cells) are at the bottom; wedge shutters are used to control the gradient of the deposition profile and shutters enable a precise control of the starting and ending point of the deposition; the sample sit at the top of the chamber. b) Schematic representation of the deposition system showing that the material sources are arranged in a 6-fold symmetry.

2.3 BST Chalcogenide Platform

My work has focused on investigation of the properties of BST system, a ternary alloy that is part of the chalcogenides material family. Among the many different compounds inside this material system, we decide to investigate the properties of BST, because this compound has been predicted and experimentally demonstrated to be a topological insulator [83]; BST films are well known as thermoelectric materials [84] and this system is also a phase change material for certain composition with a crystallization time lower than 50 ns and a crystallization temperature as low as 103^{o}C for specific compositions [52]. Moreover, BST has a narrow band gap (in its crystalline phase), high density of states near the band edges and low total thermal conductivity [85]. Recently, the optical properties of this ternary system

were investigated in the mid-IR range [86]; here we study the optical properties of BST in the UV to near-IR range across the widest compositional spread reported so far, and link these properties to the chemical composition of BST via the high-throughput approach.

Despite the complexity of this material system, its optical properties can be described in a straightforward way using the Lorentz oscillator model (section 2.4). By changing the values of the model parameters, it is possible to control the spectral position of the second crossover point (λ_2) and so the extension of the plasmonic range (Figure 2.4).

This model provide a good qualitative description of the dielectric function of chalcogenides, because the plasmonic properties of BST and p-block materials in general, have their origin on the excitation of strong interband transitions, as opposed to conventional plasmonic materials like noble metals where plasmonic properties derive from the excitation of free charges.

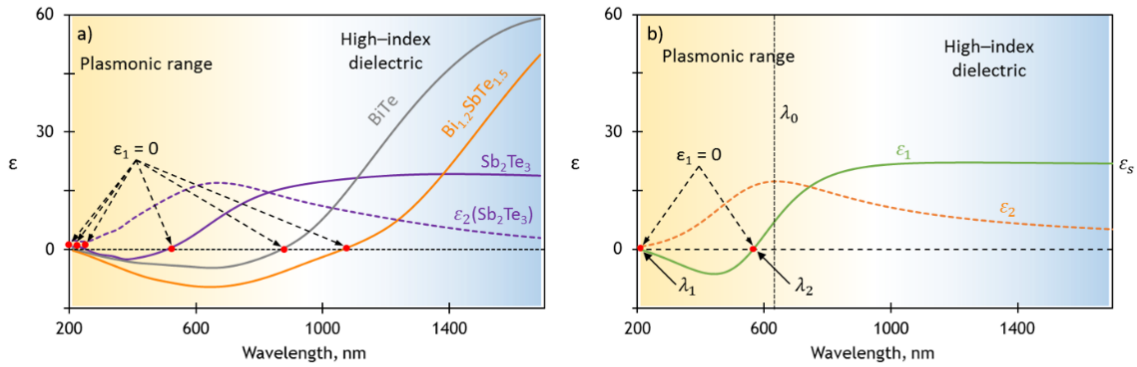

Figure 2.3: Dielectric properties of BST compounds vs Lorentz oscillator model of optical response. (a) Dispersion of ε_1 for selected compositions of BST; (b) Dispersion of ε_1 and ε_2 from the Lorentz model.

2.4 Lorentz Oscillator Model

The Lorentz dispersion model is a classical theory used to describe the interaction between light and matter. In particular, it enables the explanation of frequency dependent absorption and dispersion due to bound charges. In fact, the main assumption of this model is that an atom with electrons bound to the nucleus behaves very similarly to a small mass bound to a large mass via a spring [87]. By using this analogy, an electron bound to the nucleus reacts to an electromagnetic field by vibrating like a damped harmonic oscillator; hence, the motion of this electron is described by the following equation:

$$m\frac{d^2\boldsymbol{r}}{dt^2} + m\Gamma\frac{d\boldsymbol{r}}{dt} + m\omega_0^2\boldsymbol{r} = -e\boldsymbol{E}_{loc} \qquad (2.1)$$

Where *m* is the mass of the electron and *e* is the magnitude of the elementary charge. The first term in Eq. (2.1) is the acceleration force; the second one is the viscous damping force and gives rise for an energy loss mechanism. The third term represents the Hooke's restoring force where ω_0 is the resonant frequency of the oscillator and the last term ($-e\boldsymbol{E}_{loc}$) is the electric field driving force. $\boldsymbol{E}_{loc}$ is a microscopic field called local electric field and it is usually calculated as an average over several atomic sites. In general, $\boldsymbol{E}_{loc}$ is different from the external macroscopic field $\boldsymbol{E}$; however, we assume that $\boldsymbol{E}_{loc} = \boldsymbol{E}$, since even with this simplification the model contains all the essential features to describe the optical properties. Therefore, by assuming that the electric field varies in time as $e^{-i\omega t}$, the solution to Eq. (2.1) is:

$$\boldsymbol{r} = -\frac{e\boldsymbol{E}}{m(\omega_0^2 - \omega^2 - i\Gamma\omega)} \tag{2.2}$$

From this result, the microscopic induced dipole moment can be calculated:

$$\boldsymbol{p} = -e\boldsymbol{r} = \frac{e^2\boldsymbol{E}}{m(\omega_0^2 - \omega^2 - i\Gamma\omega)} \tag{2.3}$$

However, the following relationship exists between the induced dipole moment and the electric field:

$$\boldsymbol{p} = \varepsilon_0\alpha\boldsymbol{E} \tag{2.4}$$

Where α is the atomic polarizability. By considering N atoms per unit volume, the macroscopic polarization is:

$$\boldsymbol{P} = N\langle\boldsymbol{p}\rangle = \varepsilon_0 N\alpha\boldsymbol{E} = \varepsilon_0\chi\boldsymbol{E} \tag{2.5}$$

Where χ is the macroscopic electric susceptibility. The macroscopic quantities ***E*** and ***P*** are related also through the electric displacement field ***D***:

$$\boldsymbol{D} = \varepsilon_0\varepsilon\boldsymbol{E} = \varepsilon_0\boldsymbol{E} + \boldsymbol{P} = \varepsilon_0(1+\chi)\boldsymbol{E} \tag{2.6}$$

Where ε is the dielectric function. From Eq. (2.6) and the definitions in Eqs. (2.3) and (2.5), we obtain the expression of ε in terms of the oscillator parameters:

$$\varepsilon = 1 + \frac{(-e^2N\boldsymbol{r})}{\varepsilon_0\boldsymbol{E}} = 1 + \frac{\omega_p^2}{(\omega_0^2 - \omega^2) - i\Gamma\omega}, \qquad with\ \omega_p^2 = \frac{Ne^2}{\varepsilon_0 m} \tag{2.7}$$

Where ω_p is the plasma frequency. After that, it is possible to introduce the static dielectric constant ε_s ($\varepsilon(\omega \to 0)$) and the high frequency limit ε_∞ that are defined in the following way [88]:

$$\begin{cases} \varepsilon_s = \varepsilon(\omega \to 0) = \varepsilon_\infty + \dfrac{\omega_p^2}{\omega_0^2} \\ \varepsilon_\infty = \varepsilon(\omega \to \infty) \end{cases} \tag{2.8}$$

ε_∞ takes into account the contribution of high energy transitions; generally, $\varepsilon_\infty = 1$, but it can be greater than 1 if oscillators in higher energies exist. By using the definitions in Eq. (2.8), the dielectric function can be expressed as:

$$\varepsilon = \varepsilon_\infty + \frac{(\varepsilon_s - \varepsilon_\infty)\omega_0^2}{(\omega_0^2 - \omega^2) - i\Gamma\omega} = \varepsilon_\infty + \frac{A\omega_0^2}{(\omega_0^2 - \omega^2) - i\Gamma\omega} \tag{2.9}$$

Where *A* is defined as $(\varepsilon_s - \varepsilon_\infty)$ and it represents the oscillator strength. ε is a complex quantity and it can be separated in its real and imaginary parts:

$$\varepsilon = \varepsilon_1 + i\varepsilon_2 = \varepsilon_\infty + \frac{A\omega_0^2(\omega_0^2 - \omega^2)}{(\omega_0^2 - \omega^2)^2 + (\Gamma\omega)^2} + i\frac{A\Gamma\omega_0^2\omega}{(\omega_0^2 - \omega^2)^2 + (\Gamma\omega)^2} \tag{2.10}$$

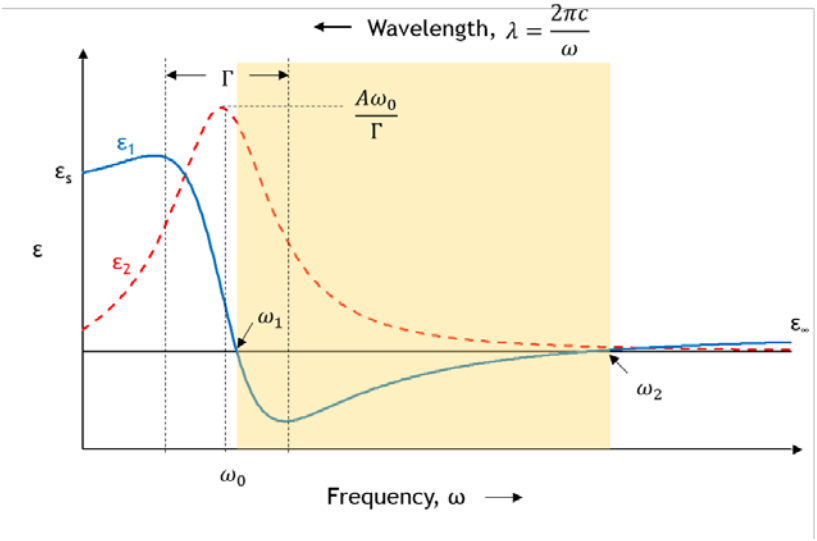

Figure 2.4: Frequency dependence of ε_1 and ε_2 calculated from the Lorentz oscillator model.

The behaviour of ε_1 and ε_2 is shown in Figure 2.4; despite the simplicity of this derivation, the Lorentz model contains three important features that are of great interest in the current research field of optics that are high index dielectrics, plasmonics and epsilon-near-zero materials.

Figure 2.4 shows that in the low frequency regime ($\omega << \omega_0$) ε_2 tends to zero while ε_1 is positive and tends to ε_s. In this region, losses are low and the material behaves as high index dielectric if ε_s has a high value since the refractive index *n* is defined as $n = \sqrt{\varepsilon_1}$ when its imaginary part, *κ*, is low.

When the frequency approaches the resonant frequency of the oscillator (ω_0), ε_2 increases and reaches the maximum at $\omega = \omega_0$. In this region, ε_2 has the form of a damped resonance curve with Γ the full width at half maximum. Since ε_1 and ε_2 are linked via Kramers-Kronig relationships, the bell-shaped curve of ε_2 gives rise to a peculiar behaviour of ε_1, namely it decreases with increasing frequency. This is called anomalous dispersion and ε_1 can be

negative due to the peak of ε_2 at ω_0. ε_1 stays negative for a certain spectral region that is called plasmonic range (highlight region in Figure 2.4). This region extends from ω_1 (corresponding to λ_2, Figure 2.3) up to the frequency ω_2 (corresponding to λ_1, Figure 2.3). At these two spectral points called epsilon-near-zero points, $\varepsilon_1 = 0$. The values of these points can be calculated analytically from Eq. (2.10); however, the analytical solutions are quite complicated to deal with. Instead, convenient approximate formulas can be derived. In particular, for the calculation of ω_1, a good approximation is that $\omega_1 \approx \omega_0$ and so we can neglect the term $(\omega_0^2 - \omega^2)^2$ at the denominator in Eq. (2.10). Hence, we obtain the following formula:

$$\omega_1 = \sqrt{\frac{A\omega_0^4}{A\omega_0^2 - \varepsilon_\infty \Gamma^2}} \tag{2.11}$$

The corresponding value of ε_2 at ω_1 is:

$$\varepsilon_2(\omega = \omega_1) = \frac{A\Gamma\omega_0^2\omega_1}{(\omega_0^2 - \omega_1^2)^2 + (\Gamma\omega_1)^2} \approx \frac{A\omega_0^2}{\Gamma\omega_1} \tag{2.12}$$

For the calculation of ω_2, we can assume that $\omega_2 \gg \omega_0$ and so we obtain:

$$\omega_2 = \sqrt{\frac{A\omega_0^2 - \varepsilon_\infty\Gamma^2}{\varepsilon_\infty}} = \sqrt{\frac{\omega_p^2 - \varepsilon_\infty\Gamma^2}{\varepsilon_\infty}} \approx \omega_p \tag{2.13}$$

With ε_2 at ω_2 equals to:

$$\varepsilon_2(\omega = \omega_2) = \frac{A\Gamma\omega_0^2\omega_2}{(\omega_0^2 - \omega_2^2)^2 + (\Gamma\omega_2)^2} \approx \frac{A\Gamma\omega_0^2}{\omega_2^3 + \Gamma^2\omega_2} \approx A\Gamma\frac{\omega_0^2}{\omega_p^3} \tag{2.14}$$

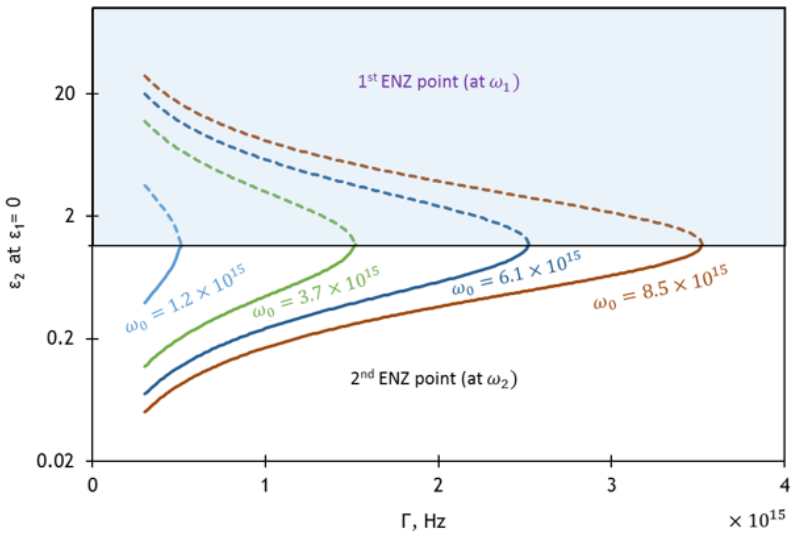

Figure 2.5: ε_2 behaviour at the crossover point. ε_2 at ε_1 equal to zero behaviour (in logarithmic scale) as a function of Γ (damping factor of the oscillator) for different values of ω_0 (resonant frequency of the oscillator). The dashed curves refer to the ENZ point at ω_1, instead the continuous lines are for the ENZ point at ω_2. The curves are calculated for $\varepsilon_\infty = 1$ and $\varepsilon_s = 2$.

The exact analytical forms of ε_2 at the crossover points (Eqs. (2.12) and (2.14)) are not straightforward to comprehend; for this reason, we study these expressions numerically and in Figure 2.5 we show the behaviour of ε_2 at ε_1 equal to zero as a function of Γ (damping factor of the oscillator) for different values of ω_0 (resonant frequency of the oscillator). We can clearly see that the curves calculated at ω_1 (dashed lines in Figure 2.5) decrease with increasing Γ for a fixed ω_0 and rise with growing ω_0; instead the curves computed at ω_2 (continuous lines in Figure 2.5) have opposite trends. Interestingly, these curves meet at a specific point and for higher values of Γ the plasmonic range disappears, namely ε_1 remains positive for all the spectral range and the material behaves as a dielectric.

2.5 High-Throughput Deposition and Characterization of BST

In order to study the properties of BST, thin films (thickness range from 17 nm up to 265 nm) were deposited with a HT-PVD system (described in section 2.2) equipped in this case with three off-axis sources (Figure 2.6). All elemental sources (Bi, Sb and Te) used have a ≥99.9999% purity and were co-deposited on a substrate held at room temperature by Knudsen-cells in a typical vacuum condition of 10^{-8} mbar. The system was calibrated to produce thin films (identically on each of several optically flat silicon and sapphire substrates) encompassing a large proportion of the BST ternary space and Bi/Sb:Te binaries. In particular, the properties of the binary compounds will be described in Chapter 3 for Bi:Te and in Chapter 4 for Sb:Te.

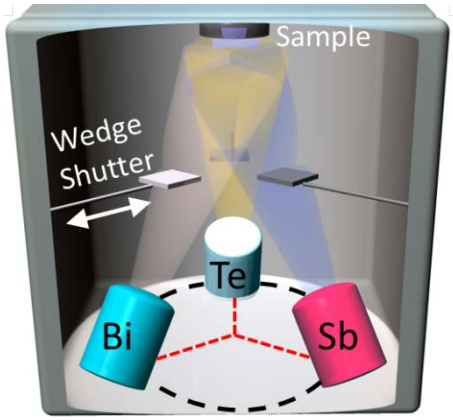

Figure 2.6: Schematic of the apparatus used for physical vapour deposition of ternary compositional gradient thin BST films, illustrating only the configuration of the most essential components of the ultra-high vacuum system - namely the computer-controlled (K-cell) evaporation sources for each constituent element, 'wedge shutters' (which control the density gradient of each element over the substrate), and the target substrate.

Thin films of BST were deposited on Si substrates for energy-dispersive x-ray spectroscopy (EDX), Raman spectroscopy and x-ray diffraction (XRD) for determination of composition and phase state, and on both silicon and sapphire (Al_2O_3) substrates for ellipsometric evaluation

of optical properties and 4-point probes measurements of sheet resistance. All substrates had dimensions of 34 mm × 34 mm; BST films are deposited over an area 28 mm × 28 mm; analyses are performed over an array of 10 × 10 points within the central 19 mm × 19 mm region (point-to-point separation 2.1 mm).

Film thickness was measured using a stylus profilometer along the external edges of the film and interpolated over the central characterization domain.

Compositional analyses were performed using an Oxford Instruments INCA EDX system on a JEOL JSM-5910 SEM with an automated stage programmed for the 10 × 10 sampling point array.

XRD was performed on as-deposited films using a D8 Bruker diffractometer equipped with a GADDS (General Area Detector Diffraction System) detector and an Incoatec IμS x-ray source (Cu, 1.54059 Å) with an x-ray beam of 0.25 mm in diameter.

Raman spectra were acquired at room temperature using a Horiba XploRA system equipped with a 532 nm laser having a maximum power of 25 mW and a spectral resolution of 3 cm^{-1}. The measurement time was 120 s and the scans were performed using a 100x objective with a laser spot diameter of 0.72 μm.

Resistivity was evaluated from a combination of sheet resistance and film thickness measurements. Sheet resistance was measured in 4-point probe (4PP) configuration a on a Signatone probe station, using two Keithley 2636 SourceMeters.

Optical properties were determined by variable angle spectroscopic ellipsometry (VASE) using a J. A. Woollam M2000 ellipsometer covering the spectral range from 210 to 1686 nm with an automated stage programmed for the 10 × 10 sampling point array.

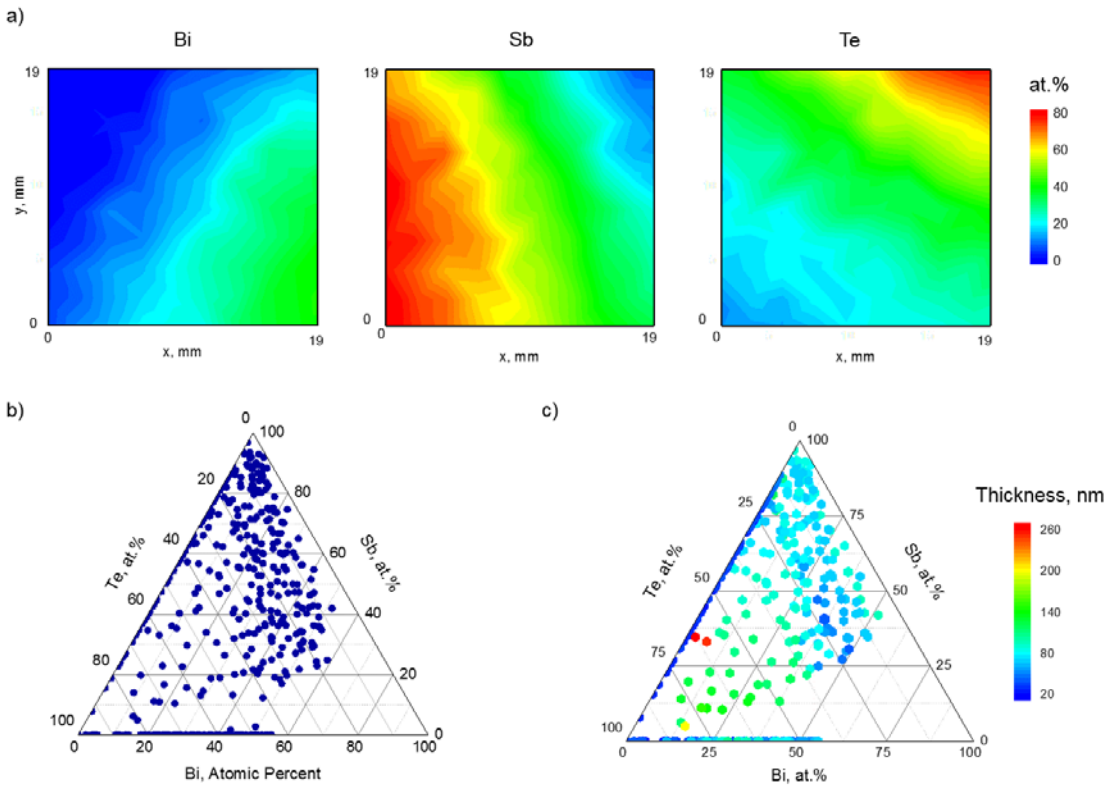

Figure 2.7: Compositional spread covered in this work for the BST system measured by EDX. a) Distributions of Bi, Sb and Te over the surface of a representative BST compositional gradient sample, evaluated by energy dispersive x-ray spectroscopy b) Compositions of the synthesized combinatorial samples of BST shown in a ternary compositional plot. c) Thickness (nm) of the BST alloy thin films plotted as a function of composition.

Figure 2.7b displays the compositional spread that we covered in this work for the BST system measured by EDX. Due to the nature of the deposition method, compositions change smoothly across the sample; therefore the points of composition measured by EDX do not represent the compositional increments that can potentially be screened, but only the envelope of material compositions synthesized [46]. Spatial distributions of single elements are shown as relative atomic percentages in colour maps for one of the deposited samples (Figure 2.7a) and the whole covered compositional spread in a ternary compositional plot (Figure 2.7b). The overall compositional range covers 0-55 at.% Bi, 7–97 at.% Sb, and 3–92 at.% Te. The compositional spread of a thin film library can be varied considerably and reproducibly on a single substrate by optimizing the deposition rate of the elements and the appropriate setting of the wedge shutters [47]. In this case, we adopted the strategy of covering most of the ternary BST material system for primary screening in order to find the most suitable properties for various nanophotonics and plasmonics application.

The thickness distribution as a function of composition is reported in Figure 2.7c; the minimum thickness is 17 nm for the binary alloy Sb:Te and the maximum is 265 nm for

Bi_3SbTe_{16}. The variations in thickness are due to the synthesis method and are intrinsic to the use of three off-axis sources with a wedge growth method [46, 47].

2.5.1 XRD analysis vs Composition

XRD analysis is a fundamental method in material science and the application of this technique on high-throughput samples can reveal the phase and crystal structure distribution across different compositions. This structural information can influence the corresponding optical properties and we would like to test if a correlation between the crystal structure phase and optical properties of BST exists.

Firstly, we present XRD measurements mapped to the corresponding chemical composition in Figure 2.8; XRD analysis was performed at room temperature on the as-deposited samples. The compositional map is divided in three areas:

- Amorphous: XRD diffractograms showing very broad or no peaks (Figure 2.9); amorphous solids have structures characterized by an almost complete lack of periodicity (or long-range order) and a tendency to order only in the sense that the atoms are fairly tightly packed together and show a statistical preference for a particular interatomic distance (short-range order) [89];
- Polycrystalline: XRD diffractograms showing narrow peaks; polycrystalline solids are characterized by long-range order inside each crystallite and this periodicity results in diffracted beams when they interact with x-rays;
- Mixture of amorphous and polycrystalline phases: XRD diffractograms showing small and damped peaks; in this case the polycrystalline phases are immersed in an amorphous matrix, hence the diffracted peaks have a lower intensity.

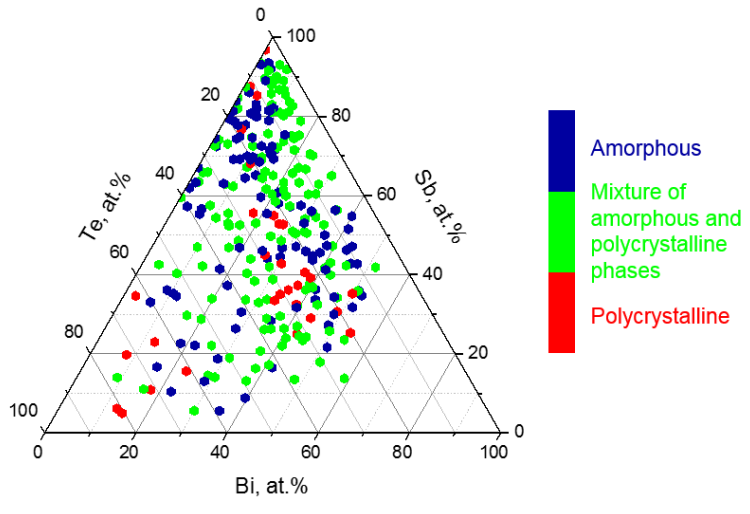

Figure 2.8: Ternary compositional map of the phases for as-deposited BST thin films. This map is obtained by combining EDX measurements with XRD diffractograms.

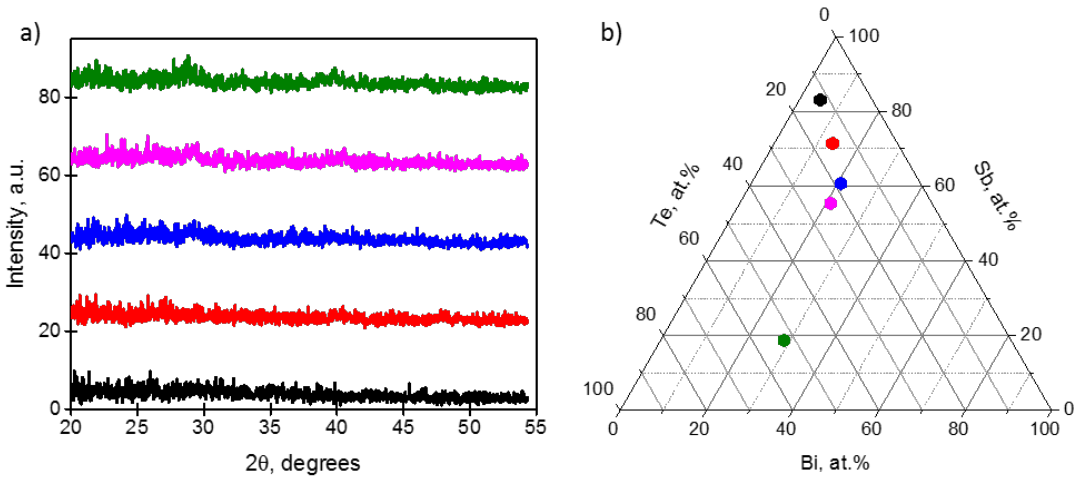

Figure 2.9: a) XRD diffractograms for selected compositions (shown in panel b) that are in the amorphous phase as deposited.

The diffractograms for the polycrystalline compositions reveals similar features along Te tie-lines of the BST ternary space. Hence, we grouped these XRD spectra in four different groups and their corresponding compositions has been plotted in a ternary map labelled by different colours in Figure 2.10.

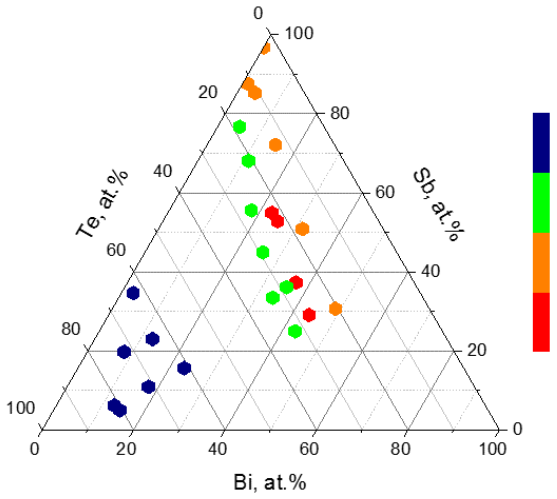

Figure 2.10: Ternary compositional map showing selected compositions grouped along Te tie-lines according to similar features on their corresponding diffractograms.

The actual diffractograms are presented in Figure 2.11 divided by colours according with Figure 2.10. The identification of crystalline phases from these diffractograms is

challenging [82], since effects like texturing (defined as the degree to which the crystallites in a polycrystalline film are similarly oriented [90]) can lead to missing Bragg reflections and variations in the relative intensities of the observed peaks compared to conventional powder diffraction [46]. Solid solutions lead to compositionally dependent lattice dimensions, which result in shifting diffraction peaks, and long-range layered structures over the restricted dimension of a thin film make them difficult to identify [46]. Moreover, low energy evaporative PVD synthesis with the substrate at low temperature favours the formation of nonequilibrium phases [46]; hence, the comparison with expected phases reported in literature is not trivial.

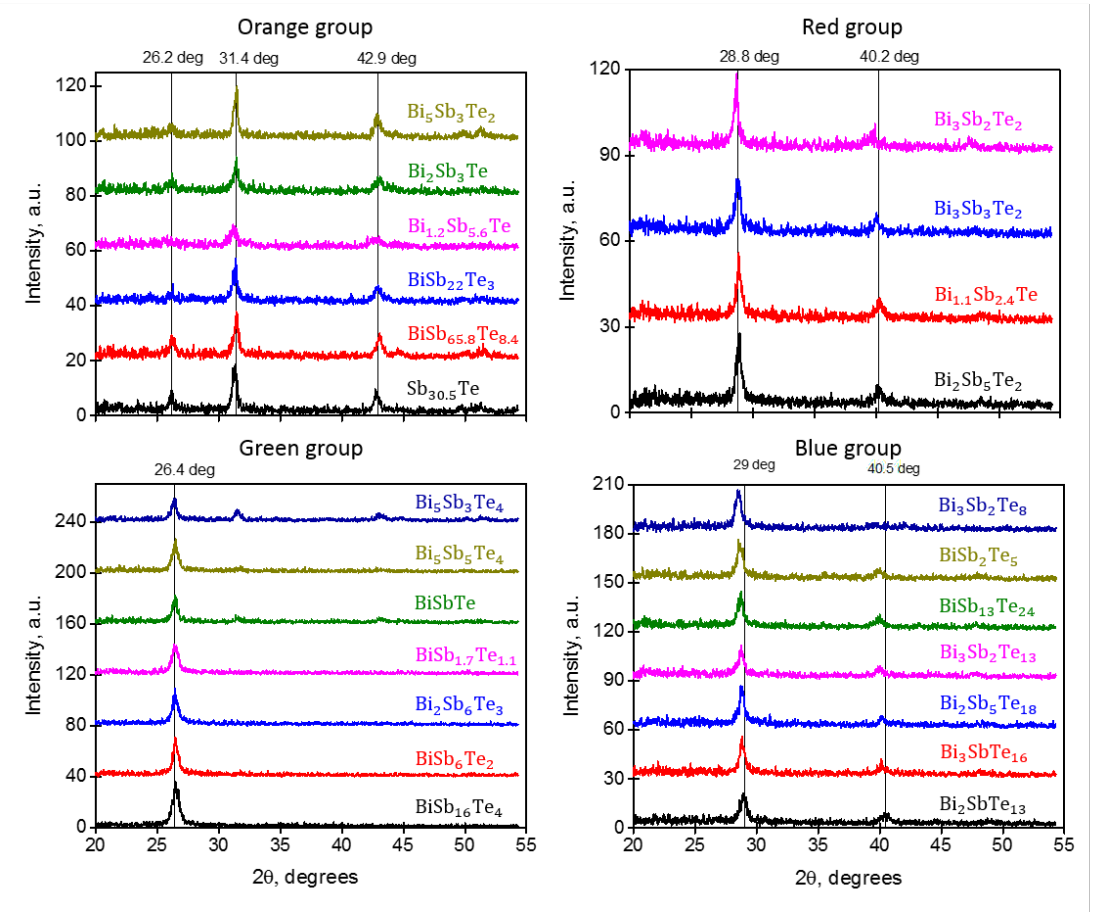

Figure 2.11: XRD diffractograms for selected compositions along Te tie-lines of the BST ternary space. Data are grouped based on similar features visible on the diffractograms. Inside each panel XRD diffractograms are plotted using a vertical offset and are labelled according to the corresponding composition.

Previous works reported that BST crystallized in a phase with space group $R\bar{3}m$ and it is composed of hexagonal close-packed atomic layers which are periodically arranged along the *c*-axis in five layers [52, 91, 92]. A qualitative comparison between literature data and our measured diffractograms suggests that these BST films crystallizes on this phase. We also observe that the peak at 29^{o} for XRD diffractograms of the blue group moves toward smaller

angles (2θ) as Te content increases meaning a longer interplanar distance (*d*) (according to Bragg's law: $2dsin\theta = \lambda$). This is in agreement with ref. [34] where they notice that lattice parameters of chalcogenides like Bi_2Te_3 rise with Te due to its larger ionic radius.

2.5.2 Raman Spectroscopy vs Composition

Raman spectroscopy can provide additional structural information to support XRD measurements. For instance, information about amorphous and polycrystalline compositional areas can be further refined, because Raman spectra characteristic of crystalline solids (long-range order) contain sharp lines, since in a crystal only optical phonons at the Brillouin zone are Raman active [93]. Instead, with the loss of long-range order in an amorphous solid, the Raman selection rules for crystalline solids no longer hold [93]. Hence, all the phonons of the Brillouin zone become Raman active and the corresponding Raman spectrum is very broad, because it contains contributions from the full vibrational density of states [94].

Moreover, the peaks visible on Raman spectra for crystalline solids correspond to specific lattice vibrations, thus Raman spectroscopy can provide structural information about chemical bonds and spatial arrangements of atoms in the solid. In this context, group theory is particularly useful, because it enables the classification of lattice vibrations by symmetry and provides also selection rules for these vibrational modes.

In order to obtain a further insight into the crystalline structures presented in the previous section, here we consider XRD diffractograms and Raman together with EDX measurements.

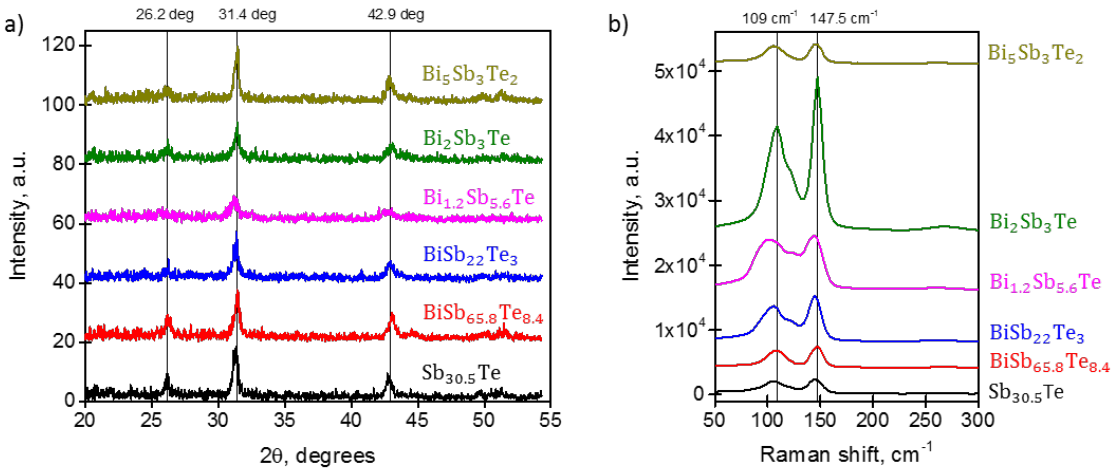

Figure 2.12: XRD diffractograms in a) and corresponding Raman spectra in b) for selected compositions along Te tie-line of the BST ternary space (orange group in Figure 2.10). Inside each panel XRD diffractograms and Raman spectra are plotted using a vertical offset and are labelled according to the corresponding composition.

Firstly, we analyse compositions along the tie-line with Te content (at. %) close to 10 % defined as orange group in Figure 2.10; XRD diffractograms show three peaks with the highest one at 31.4°. The corresponding Raman spectra (Figure 2.12b) presents two peaks, one at 109 cm^{-1} and the other at 147.5 cm^{-1}. The comparison with literature data reveals that these peaks correspond to Sb-Sb vibrations. In fact, elemental *c*-Sb has two atoms per unit cell and so group theory given the symmetry of $R\bar{3}m$ space group predicts three zone-centre optical modes (3σ – 3 where σ is the number of atoms in the primitive unit cell), i.e., a singly degenerate A_{1g} mode (totally symmetric) and a doubly degenerate E_g mode [95]. This tells that for these compositions (rich in Sb) Sb tends to segregate and form a crystallized phase buried in an amorphous matrix of Bi and Te. The composition with stoichiometry $Bi_{1.2}Sb_{5.6}Te$ has a reduced long-range order, because both XRD and Raman spectra present broad peaks more typical of amorphous solids than crystalline materials.

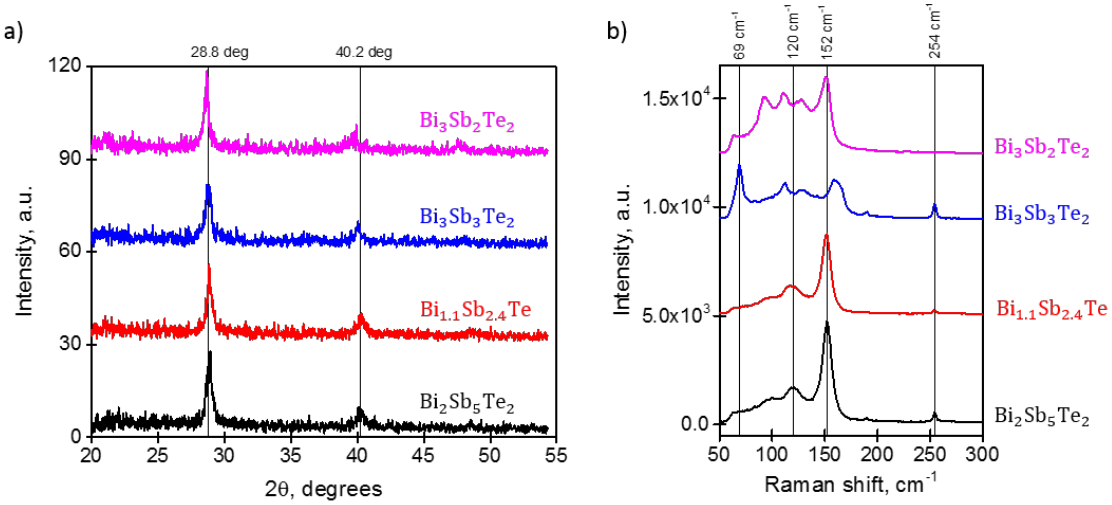

Figure 2.13: XRD diffractograms in a) and corresponding Raman spectra in b) for selected compositions along Te tie-line of the BST ternary space (red group in Figure 2.10). Inside each panel XRD diffractograms and Raman spectra are plotted using a vertical offset and are labelled according to the corresponding composition.

Secondly, we consider compositions with Te content (at. %) close to 20 % (red group in Figure 2.10). The corresponding XRD diffractograms in Figure 2.13a show two peaks with the highest one at 28.8°. The respective Raman spectra with higher content in Sb ($Bi_2Sb_5Te_2$ and $Bi_{1.1}Sb_{2.4}Te$) present similar spectra to the ones observed for the orange group compositions (Figure 2.12). Instead, $Bi_3Sb_3Te_2$ Raman spectrum has two clear peaks and some smaller peaks are also visible. In particular, the peak at 69 cm^{-1} can be related to Bi-Bi vibrations [96], in fact elemental *c*-Bi is isostructural with Sb and group theory predicts a singly degenerate A_{1g} mode at 96.8 cm^{-1} and a doubly degenerate E_g mode at 69.2 cm^{-1}. The peak at 160 cm^{-1} is probably due to Sb-Te vibrations [97] while the one at 112 cm^{-1} could be related to Sb-Sb vibrations and the other at 127 cm^{-1} is typical of Bi:Sb alloys [98]. Raman spectrum for

$Bi_3Sb_2Te_2$ presents similar peaks, namely the one at 126 cm^{-1} is typical of Bi:Sb alloys and the one at 152 cm^{-1} is typical of Sb-Sb vibrations. In this case, it is observed also a small peak at 90 cm^{-1} that is probably due to Te-Te vibrations. In fact, elemental c-Te crystallizes in a trigonal crystallographic phase with space group $P3_121$ (152) or $P3_221$ (154) [99]. The primitive unit cell contains three atoms and group theory predicts three Raman active modes, namely an A_1 mode and two E modes [99]. The peak at 254 cm^{-1} is not reported in literature and its origin is not identified.

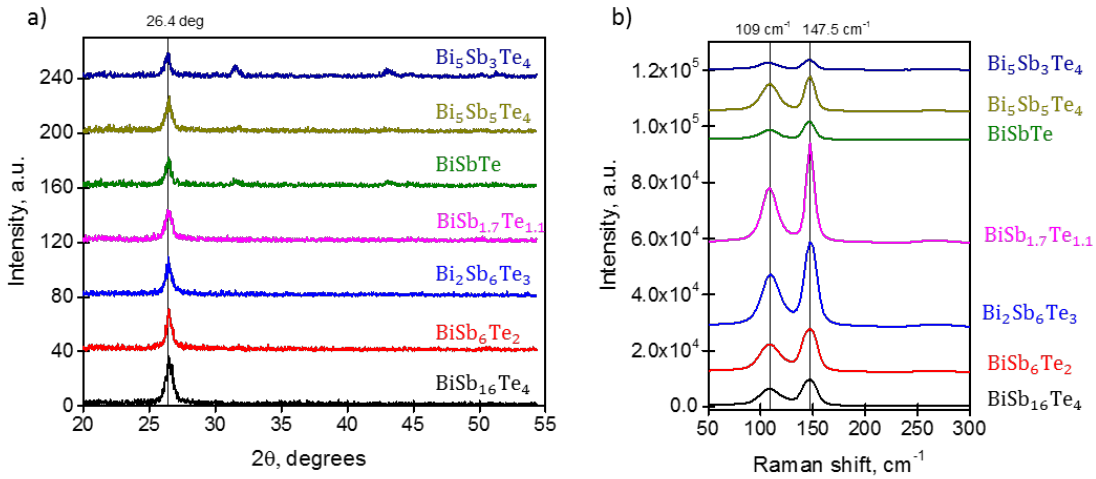

Figure 2.14: XRD diffractograms in a) and corresponding Raman spectra in b) for selected compositions along Te tie-line of the BST ternary space (green group in Figure 2.10). Inside each panel XRD diffractograms and Raman spectra are plotted using a vertical offset and are labelled according to the corresponding composition.

Thirdly, the green group shows only one peak at 26.4° on XRD diffractograms and Raman spectra are very close to the one observed for the orange group. Namely, two peaks at 109 cm^{-1} and 147.5 cm^{-1} are present revealing that also for these compositions Sb tends to segregate and form a crystallized phase buried in an amorphous matrix of Bi and Te.

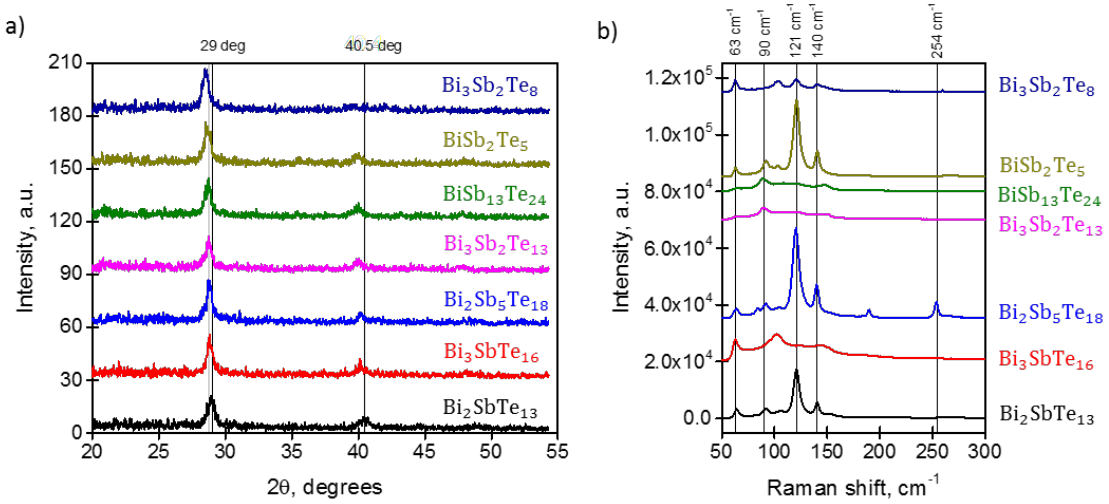

Figure 2.15: XRD diffractograms in a) and corresponding Raman spectra in b) for selected compositions along Te tie-line of the BST ternary space (blue group in Figure 2.10). Inside each panel XRD diffractograms and Raman spectra are plotted using a vertical offset and are labelled according to the corresponding composition.

Finally, we consider the blue group that has a Te content (at. %) varying from 60 % to 80 %. XRD diffractograms show two peaks with the highest one that shift from 29° to smaller angles as Te content is increased (Figure 2.15a). The corresponding Raman spectra present three peaks at 90 cm^{-1}, 120 cm^{-1} and 140 cm^{-1} ascribable to Te-Te vibrations [99], instead the small peak at 63 cm^{-1} is probably due Bi-Te vibrations.

Table 2.1: Summary of literature data extracted from Raman spectra of elemental crystals of Bi, Sb, Te, compound crystals of Bi_2Te_3, Sb_2Te_3, Bi:Sb alloys and their corresponding solid solutions $(Bi_{(1-x)}Sb_x)_2Te_3$ (0 < x< 1) [91, 97-102].

Material	Space group	Raman modes	
		Symmetry	Frequency, cm^{-1}
c-Bi [96]	$R\bar{3}m$ (166)	E_g	69.2
		A_{1g}	96.8
c-Sb [103]	$R\bar{3}m$ (166)	E_g	110
		A_{1g}	149.8
Bi:Sb [98]	$R\bar{3}m$ (166)	E_g (Bi)	~75
		A_{1g} (Bi)	~100
		E_g (Sb)	~115
		A_{1g} (Sb)	~150
		-	125
c-Te [99]	$P3_121$ (152) or $P3_221$ (154)	E	92.2
		A_1	120.4
		E	140.7

Material	Space group	Raman modes	
		Symmetry	Frequency, cm^{-1}
Bi_2Te_3 [104]	$R\bar{3}m$ (166)	E_g^1	30
		A_{1g}^1	56
		E_g^2	97
		A_{1g}^2	128
Sb_2Te_3 (d = 20 nm) [97]	$R\bar{3}m$ (166)	E_g^1	46
		A_{1g}^1	70
		E_g^2	110
		A_{1g}^2	162
$Bi_{0.5}Sb_{1.5}Te_3$ (d = 150 nm) [100]	$R\bar{3}m$ (166)	E_g^1	-
		A_{1g}^1	70 [91]
		E_g^2	112
		A_{1u}^2	126.9
		A_{1g}^2	156.7

A summary of literature data extracted from Raman spectra of elemental crystals of Bi, Sb, Te, compound crystals of Bi_2Te_3, Sb_2Te_3, Bi:Sb alloys and their corresponding solid solutions $(Bi_{(1-x)}Sb_x)_2Te_3$ ($0 < x < 1$) [91, 97-102] used for the interpretation of our measured Raman spectra is reported in Table 2.1.

2.5.3 Resistivity Measurements vs Composition

Resistivity measurements mapped to corresponding chemical composition are reported in Figure 2.16. DC resistivity (ρ) variations reveals a variation of resistivity in the range comprised between 4×10^{-2} Ωcm and 10^{-4} Ωcm: the largest value of ρ is observed for a relatively low concentration of Bi, close to the binary Sb_2Te_3, and values of resistivity decrease with increasing Bi concentration (Figure 2.16b). This trend essentially reflects the extent of the alloys' metallic character, with Bi and Sb being semimetals while Te is a semiconductor with a small band gap (0.33 eV).

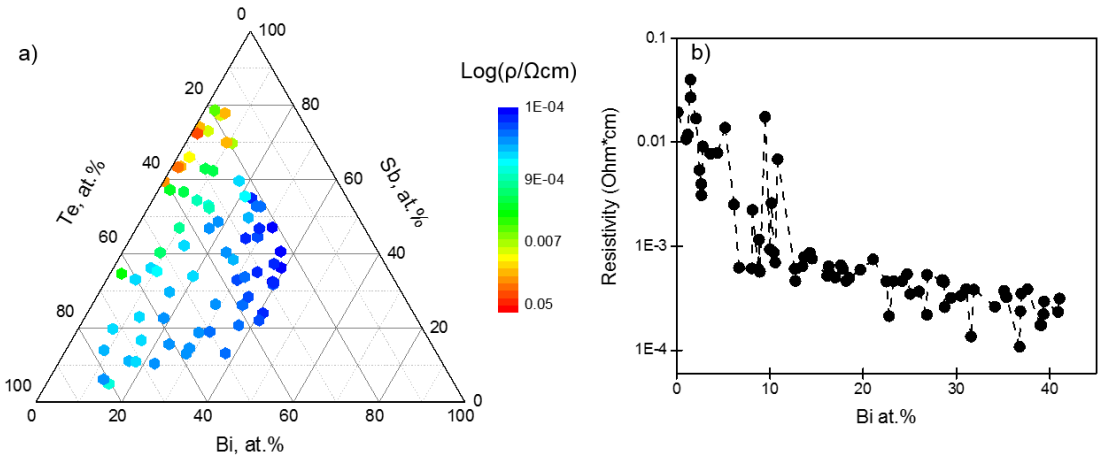

Figure 2.16: a) Resistivity obtained by combining 4 point probe (sheet resistance) and thickness measurements as a function of composition with corresponding resistivities along the indicated tie-line shown in b).

2.5.4 Compositional Tuning of Optical Properties

In this section, we map the optical properties of BST as a function of its composition. Therefore, we analyse the spectral dispersion of complex refractive index ($N = n + i\kappa$) and dielectric function ($\varepsilon = \varepsilon_1 + i\varepsilon_2$) obtained from ellipsometry measurements: first we show the typical dispersion curves (Figure 2.17) for some compositions in the BST ternary space and then we plot these properties for all the analysed compositions at certain specific wavelengths (Figure 2.19).

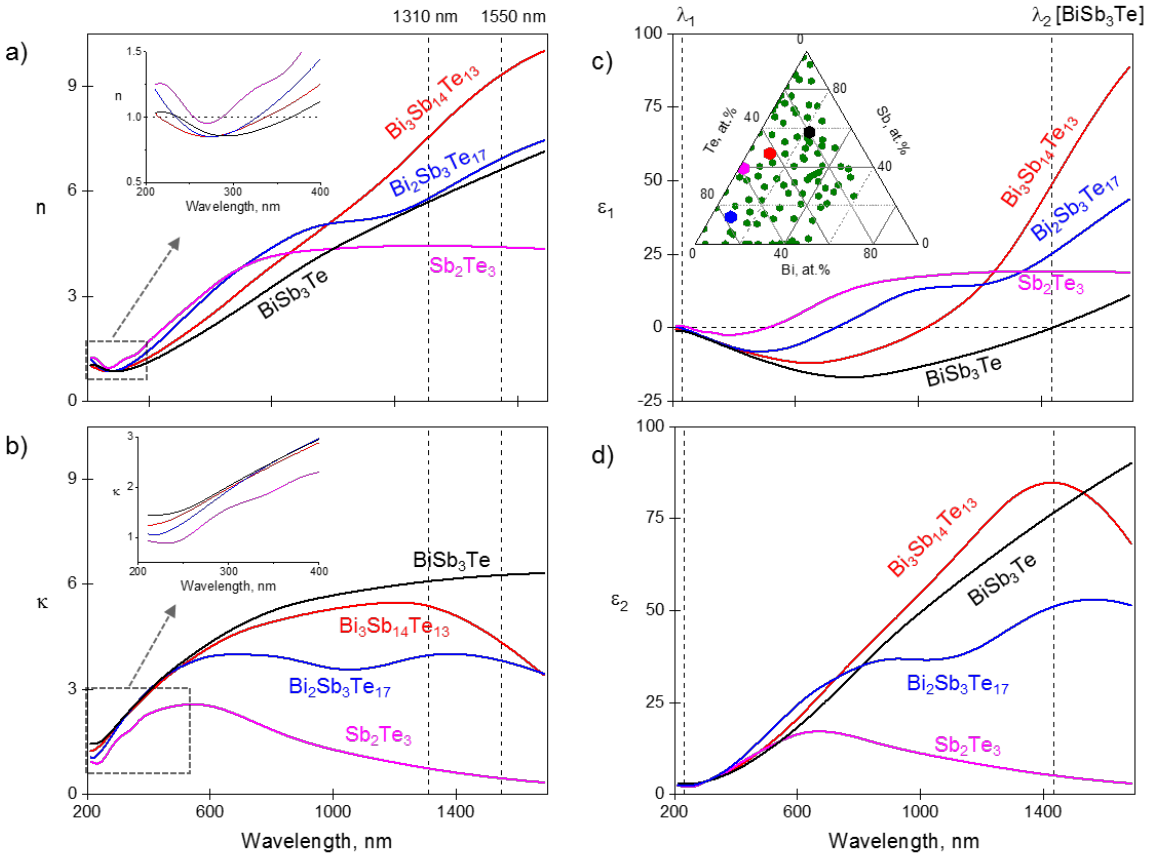

Figure 2.17: Compositional variation in spectral dispersion of BST optical properties. Spectral dispersion of a) refractive index n, b) extinction coefficient κ, and c, d) the real and imaginary parts ε_1 and ε_2 respectively of relative permittivity for a selection of BST alloy compositions (as labelled), measured by variable-angle spectroscopic ellipsometry. Insets to a) and b) show detail in the 200-400 nm wavelength range. The inset to c) shows the stoichiometric range encompassed in the present study – each green point denoting the measured elemental ratio at one of the compositional gradient sampling points; black, red, magenta and blue dots denote the compositions for which spectra are plotted, using lines of the same colour, in the four main panels (a-d). The film thicknesses are: 53.9 nm for $BiSb_3Te$ (black line), 92.3 nm for $Bi_3Sb_{14}Te_{13}$ (red line), 128.6 nm for $Bi_2Sb_3Te_{17}$ and 30.7 nm for Sb_2Te_3 (magenta line).

Figure 2.17 shows a representative selection of BST permittivity and refractive index spectra, from which it can be seen that:

- The real part of the refractive index *n* (Figure 2.17a and inset) is characteristically low - close to if not less than 1 (i.e. the refractive index of vacuum) - in the near-UV spectral range, offering interesting possibilities in low/high-index hybrid photonic (nano)structures;
- *n* is in contrast characteristically high - reaching values in excess of 11 - at near-IR wavelengths, offering promise for telecoms frequency all-dielectric metamaterial applications;

- Similarly, the extinction coefficient κ (Figure 2.17b) is typically lowest at the short near-UV end of the measured spectral range and increases with wavelength, in some cases across the entire measured visible to near-IR range, in others to a maximum at some point within that range beyond which it then decreases;
- The real part of relative permittivity ε_1 (Figure 2.17c) is characteristically equal to zero at an almost compositionally-invariant near-UV wavelength λ_1 of around 250 nm; the corresponding imaginary part of relative permittivity ε_2 (Figure 2.17d) typically takes its minimum value for a given composition at or around this point;
- The spectral position λ_2 of the second ε_1 zero-crossing, and thereby the range of wavelengths over which ε_1 is negative (i.e. over which an alloy is plasmonic), is a strong function of stoichiometry, as are the associated losses (values of ε_2) (Figure 2.17c and d). It should be noted here that the near-UV/near-IR plasmonic properties of BST and p-block semiconductors in general (i.e. compounds of elements in groups 13 [IIIA] to 18 [VIIIA] of the periodic table, with valence electrons in the p-orbital), differ from those of the noble metals in that they derive not from the excitation of free charges (a mechanism that becomes relevant in such materials only at much longer wavelengths) but rather from the excitation of strong interband transitions, with a possible contribution in some cases from topological conductive surface states [105].

To look more systematically at some of these behaviours: Figure 2.18a displays λ_2 – the longer wavelength $\varepsilon_1 = 0$ point (i.e. the upper limit of the plasmonic, negative ε_1 range) as a function of composition. It is seen that this point red-shifts, all the way from 495 nm out to 1685 nm, with decreasing Te content and with increasing Bi content. ($Bi_5Sb_3Te_4$ exhibits the broadest plasmonic range, from 210 nm, lowest limit of ellipsometer, to 1680 nm). The corresponding values of ε_2 shown in Figure 2.18b follow a similar trend as observed for ε_1, being lowest for the Te-rich binaries and increasing steeply with decreasing Te and increasing Bi content. Losses, i.e. values of ε_2, at the (almost compositionally invariant) near-UV $\varepsilon_1 = 0$ wavelength λ_1 Figure 2.18c) are uniformly much lower than at λ_2. They vary only by a factor of two over the entire measured compositional range but again tend to increase with decreasing Te and increasing Bi content. High-tellurium Sb:Te binaries present the lowest values of ε_2 where $\varepsilon_1 = 0$ and as such may be useful in studies of ENZ phenomena at optical frequencies (Chapter 4).

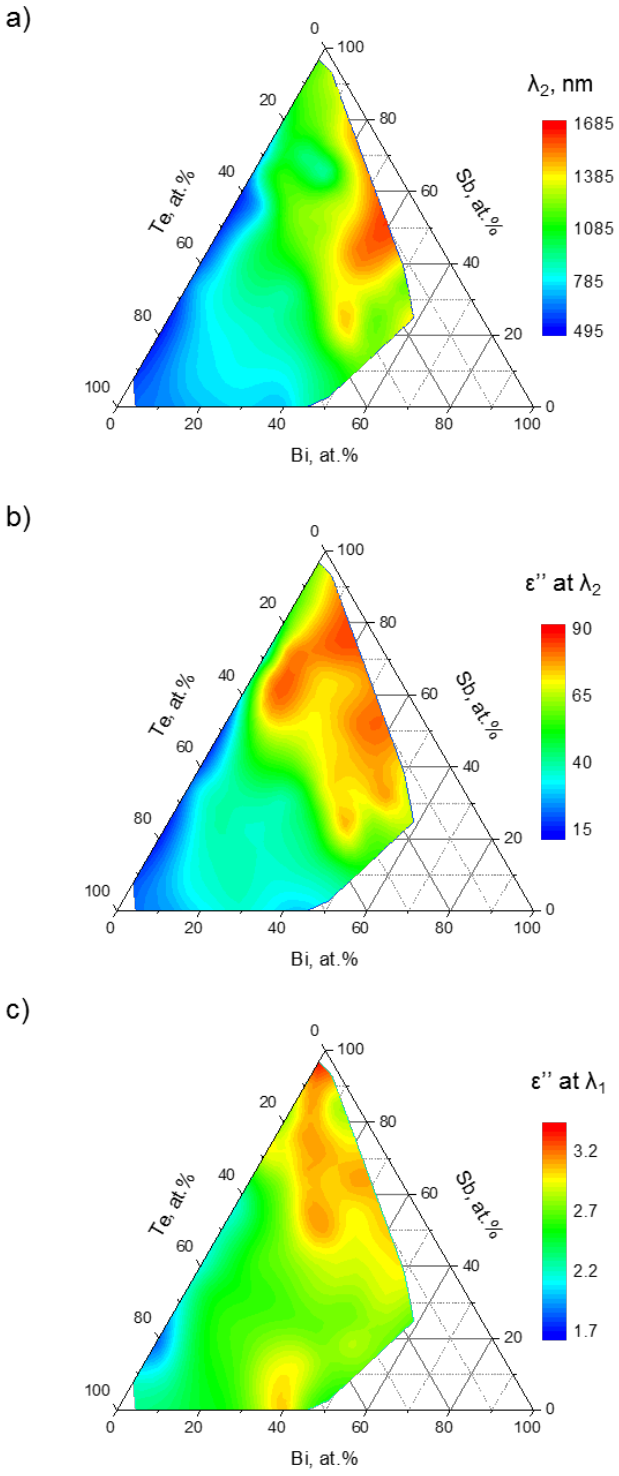

Figure 2.18: ε_1 = 0 properties of BST. a) Visible to near-IR ε_1 = 0 wavelength λ_2, below which an alloy is plasmonic (i.e. has a negative value of ε_1) as a function of composition, and b) the corresponding value of ε_2. c) Compositional dependence of the value of ε_2 at the near-UV ε_1 = 0 wavelength λ_1 (~250 nm for all compositions).

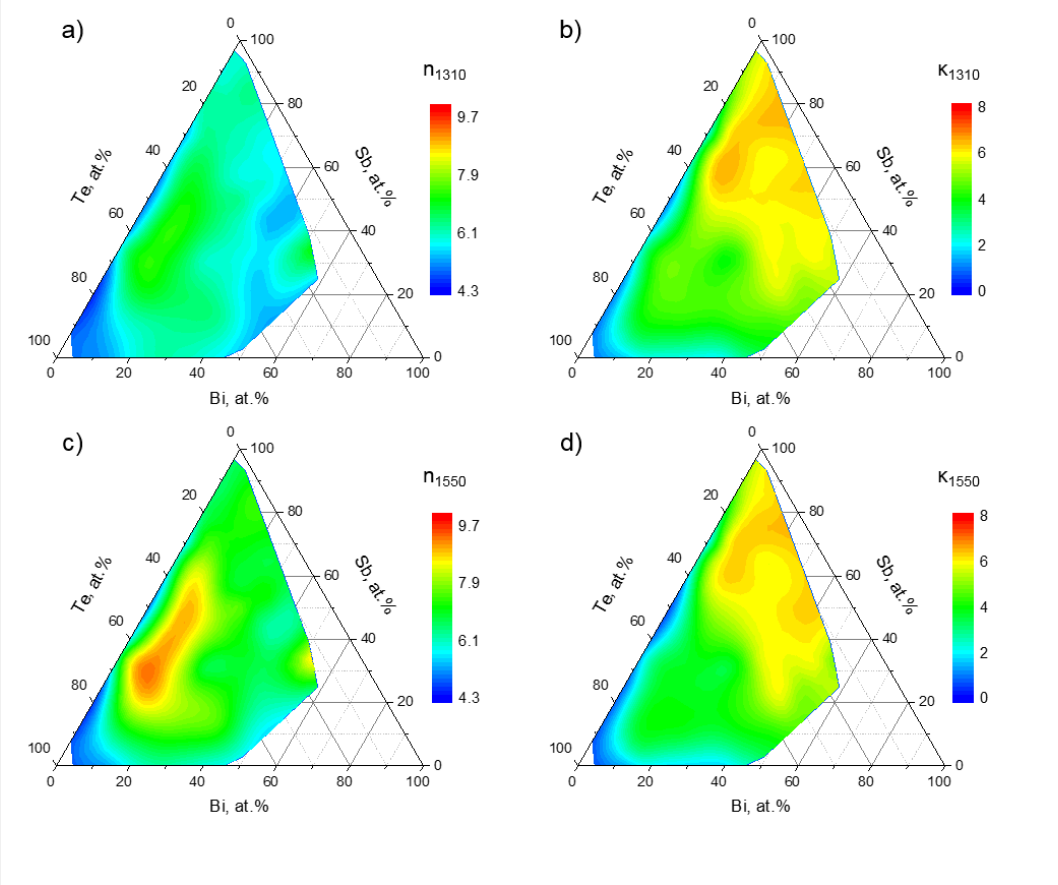

Figure 2.19: Optical properties of BST at telecoms wavelengths. Compositional dependence of (a, c) refractive index n and (b, d) extinction coefficient κ at (a, b) 1310 and (c, d) 1550 nm.

Figure 2.19 shows the compositional dependence of BST refractive index at near-IR telecommunications wavelengths of 1310 nm and 1550 nm. The real part of the refractive index reaches a value as high as 8 at 1310 nm (Figure 2.19a) in tellurium-rich (>40 at.%), antimony-lean (<50 at.%) alloys containing 10-40 at.% bismuth. Even higher values of *n* (close to 9) are observed at 1550 nm for ternary compositions containing 10-20 at.% Bi and 20-70 at.% of either Sb or Te (Figure 2.19c). These exceptionally high values of *n* tend to be accompanied by high values of *κ*, however a range of typically (near-)binary compositions is revealed that present still high values of *n* (around 6-7) with values of *κ* less than 1, which could support strong resonances when structured as all-dielectric metamaterials.

To assess the various alloys manufactured here for their potential in nanophotonic and metamaterial applications we evaluate three different figures of merit: the first, F_1, characterizes the material's ability to support surface plasmon-polaritons (SPP) at an interface with vacuum and is defined as the SPP dissipation length $d_{SPP} = 1/Im\{k_{SPP}\}$ ($Im\{k_{SPP}\}$ being the imaginary part of the SPP wavevector calculated as $k_{SPP} =$

$k_0\sqrt{\varepsilon_{BST}\varepsilon_{air}/(\varepsilon_{BST}+\varepsilon_{air})}$, where $k_0 = \omega/c$ is the free space wavevector) in units of its SPP wavelength $\lambda_{SPP} = 2\pi/Re\{k_{SPP}\}$ [34, 106]:

$$F_1 = \frac{d_{SPP}}{\lambda_{SPP}} = \frac{Re\{k_{SPP}\}}{2\pi Im\{k_{SPP}\}} \tag{2.15}$$

The second figure of merit, F_2, characterizes a material's ability to support localized surface plasmon resonances (LSPR) in spherical nanoparticles and is defined as the ratio of resonant frequency to width of the resonance line [27]:

$$F_2 = \frac{|\varepsilon_1|}{\varepsilon_2} = \frac{|n^2 - \kappa^2|}{2n\kappa} \tag{2.16}$$

The third figure of merit, F_3, characterizes a material's ability to support low loss propagating waves within its volume (as an indicator of suitability as a platform for all-dielectric metamaterials supporting high-quality Mie resonances) and is defined as the dissipation length of a transverse electromagnetic wave $d = \lambda_0/4\pi\kappa$ in a dielectric with refractive index $N = n + i\kappa$, in units of its wavelength $\lambda = \lambda_0/n$:

$$F_3 = \frac{d}{\lambda} = \frac{n}{4\pi\kappa} \tag{2.17}$$

These figures of merit, plotted in Figures 2.20-2.22 alongside values for the noble metals and a selection of nitrides and conductive oxides considered to be among the most promising alternative plasmonic [18, 107-110] media, and semiconductors most frequently employed as platforms for all-dielectric metamaterials, reveal that:

- BST chalcogenides are (within the measured compositional range) uniformly better host materials for SPP's - have higher values of F_1 (Figure 2.20) - than titanium nitride and transparent conductive oxides (specifically aluminium- and gallium-doped zinc oxide, and indium tin oxide) over the near-UV to near-IR spectral range. They are moreover comparable if not superior to gold at wavelengths below 580 nm and silver below 365 nm. Over the entire spectral range of interest here the highest values of F_1 (coming within a factor of ~2 of that of Al at around 800-900 nm) are provided by the ternary alloy $Bi_5Sb_3Te_2$. This value is more than sufficient to support long-range SPPs in an insulator-metal-insulator waveguide as shown in Figure 2.23.

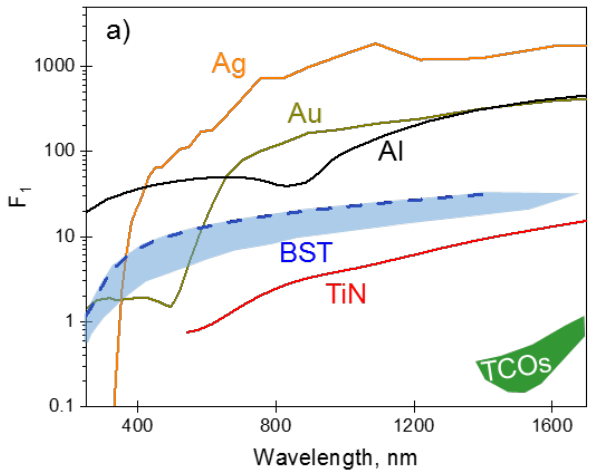

Figure 2.20: Performance of BST alloys for supporting propagating surface plasmon polaritons. Spectral dispersion of figure of merit F_1 relating to the ability of BST and a selection of other materials (as labelled) to support propagating surface plasmon polaritons at a vacuum interface. Blue areas encompass all ternary and binary BST compositions analysed within the present study (see inset to Figure 2.17c). Dashed blue lines correspond to the particular compositions achieving maximum values of the figures of merit within the near-UV/near-IR spectral range under consideration. Data for other materials is taken from literature as follows: Ag and Au from Ref. [107]; Al from Ref. [109]); TiN from Ref. [110]; TCOs - AZO, GZO and ITO from Ref. [111].

- In regard to LSPRs, on the basis of F_2 (Figure 2.21), BST alloys are better than silver below ~330 nm, gold below ~512 nm, TiN below ~690 nm, and TCOs below ~1400 nm. $Bi_5Sb_3Te_2$ is again among the best compositions, presenting a value of F_2 for near-UV/visible wavelengths that is comparable to that of TiN over the near-IR range and to TCOs at the upper limit of the spectral range under consideration. It achieves a maximum value of F_2 equal to 1.64 at 350 nm, which is more than sufficient to support high quality resonances [105]. This is further illustrated by the numerically simulated optical response of subwavelength period nano-grating metasurfaces of varying composition presented in Figure 2.24: the resonance observed in reflection mode has a higher quality-factor for $Bi_5Sb_3Te_2$ compared with other compositions that have a lower F_2.

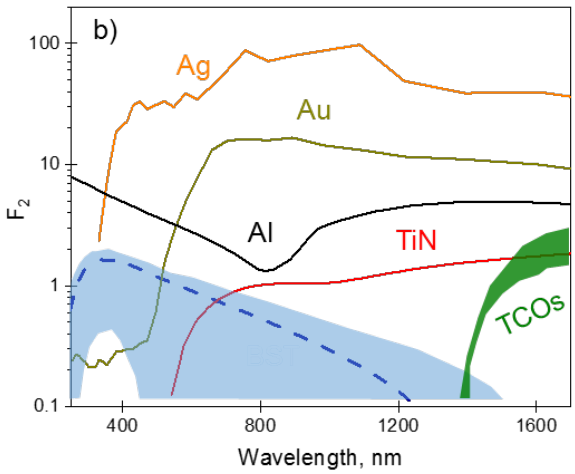

Figure 2.21: Performance of BST alloys for supporting localized, spherical nanoparticle surface plasmons. Spectral dispersion of figure of merit F_2 relating to the ability of BST and a selection of other materials (as labelled) to support localized, spherical nanoparticle surface plasmons. Blue areas encompass all ternary and binary BST compositions analysed within the present study (see inset to Figure 2.17c). Dashed blue lines correspond to the particular compositions achieving maximum values of the figures of merit within the near-UV/near-IR spectral range under consideration. Data for other materials is taken from literature as follows: Ag and Au from Ref. [107]; Al from Ref. [109]); TiN from Ref. [110]; TCOs - AZO, GZO and ITO from Ref. [111].

- As a high-index dielectric, BST comes into its own at near-IR wavelengths, with values of F_3 (Figure 2.22) exceeding those of TCOs above ~1220 nm. The highest figures of merit are offered by the binary composition Sb_3Te_8 – values come within a factor of 2 of those of germanium (at around 700-800nm), though by virtue of losses are much lower than those of silicon. This value of F_3 is sufficient to support high dielectric Mie resonances as presented in Figure 2.25.

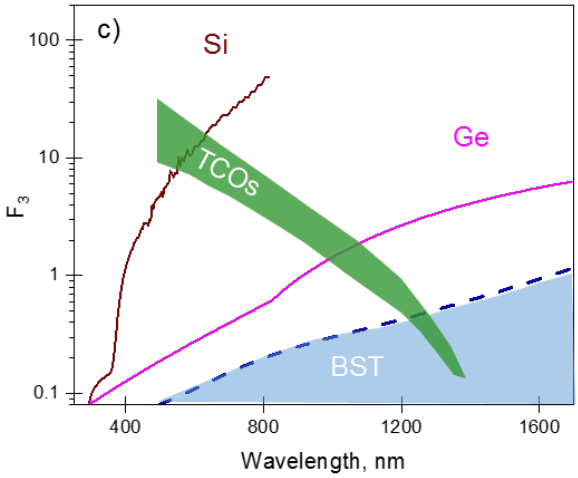

Figure 2.22: Performance of BST alloys as high-index dielectric media. Spectral dispersion of figure of merit F_3 relating to the ability of BST and a selection of other materials (as labelled) to support low-loss propagating light waves. Blue areas encompass all ternary and binary BST compositions analysed within the present study (see inset to Figure 2.17c). Dashed blue lines correspond to the particular compositions achieving maximum values of the figures of merit within the near-UV/near-IR spectral range under consideration. Si data is taken from Ref. [112]; Ge optical constants were measured by variable-angle spectroscopic ellipsometry for a Ge film with a thickness of 160 nm deposited by resistive evaporation.

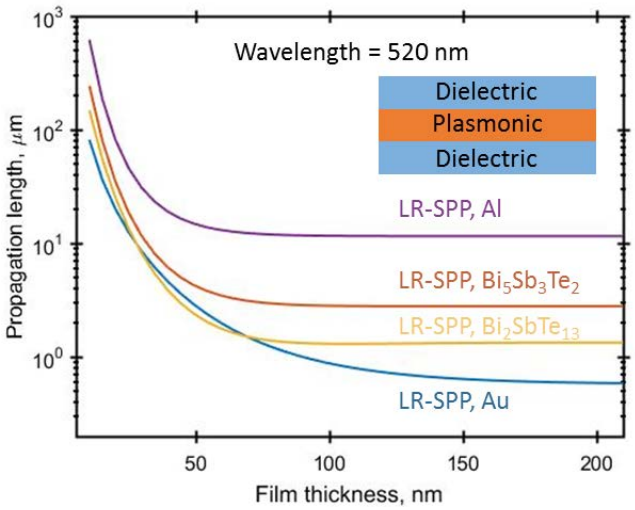

Figure 2.23: Propagation lengths at the excitation light wavelength of 520 nm calculated for an insulator-metal-insulator waveguide (dielectric is air in this case) considering different plasmonic materials: Al, BST and Au. These propagation lengths are calculated for the long-range surface plasmon polaritons (LR-SPPs) using the explicit dispersion relations derived in ref. [113]. $Bi_5Sb_3Te_2$ is the composition with the highest value of F_1 equal to 11.3 at 520 nm; instead, the value of F_1 for Bi_2SbTe_{13} is 6.8 at 520 nm.

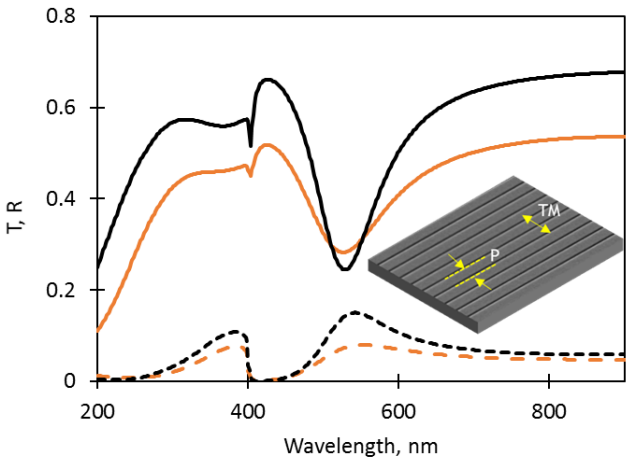

Figure 2.24: Numerically simulated optical response of plasmonic subwavelength period nano-grating metasurfaces of varying composition. Comparison of transmission (dashed lines) and reflection (continuous lines) spectra calculated from FDTD simulation for subwavelength nanogratings with period of 400 nm, thickness 140 nm and groove width of 50 nm with incident light polarized in the direction opposite to the grating grooves (TM mode) between BST compositions with different values for the figure of merit for localized surface plasmon resonances (F_2): black curves refers to the BST composition ($Bi_5Sb_3Te_2$) with the highest FOM value of 1.64 at 350 nm, instead, orange curves are related to a BST composition (Bi_2SbTe_{13}) with a FOM of 0.9 at 330 nm.

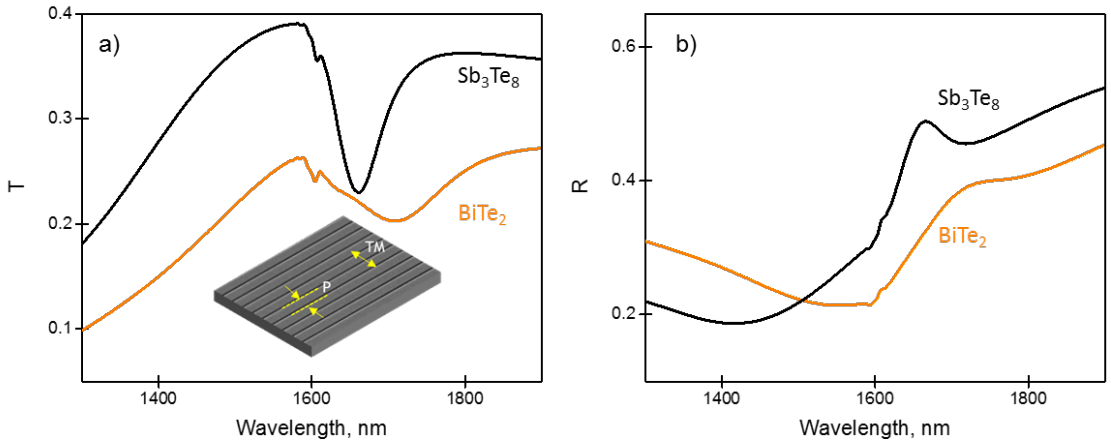

Figure 2.25: Numerically simulated optical response of all-dielectric subwavelength period nano-grating metasurfaces of varying composition. Comparison of transmission spectra calculated from FDTD simulation for subwavelength nanogratings with period of 1100 nm, thickness 160 nm and groove's width of 100 nm with incident light polarized in the direction opposite to the grating grooves (TM mode) between BST compositions with different values of F_3: black curves refers to the composition (Sb_3Te_8) with the highest value of F_3 equal to 1.13 at 1685 nm, instead, orange curves are related to $BiTe_2$ that has a F_3 of 0.31 at 1685 nm.

2.6 Summary

In conclusion, from a systematic study enabled by high-throughput physical vapour deposition and characterization techniques, we derive stoichiometric dependences of the spectrally dispersive photonic properties of binary and ternary bismuth antimony telluride (BST) chalcogenide alloys. According to composition, it is found that as-deposited thin films can be low-index/low-epsilon and plasmonic materials from the near ultraviolet to the visible range and high-index dielectrics in the near-infrared spectral region.

We consider three different figures of merit to assess the BST alloys manufactured here and compared their properties with other well-known materials for nanophotonic and metamaterial applications. Based on that, BST chalcogenides have higher values of F_1 (Figure 2.20) - than titanium nitride and transparent conductive oxides (specifically aluminium- and gallium-doped zinc oxide, and indium tin oxide) over the near-UV to near-IR spectral range. Moreover, they are comparable if not superior to gold at wavelengths below 580 nm and silver below 365 nm. Over the entire spectral range of interest here, the highest values of F_1 (coming within a factor of ~2 of that of Al at around 800-900 nm) are provided by the ternary alloy $Bi_5Sb_3Te_2$. This value is more than sufficient to support long-range SPPs in an insulator-metal-insulator waveguide as shown in Figure 2.23. On the basis of F_2 (Figure 2.21), BST alloys are better than silver below ~330 nm, gold below ~512 nm, TiN below ~690 nm, and TCOs below ~1400 nm. $Bi_5Sb_3Te_2$ is again among the best compositions, presenting a value of F_2 for near-UV/visible wavelengths that is comparable to that of TiN over the near-IR range and to TCOs at the upper limit of the spectral range under consideration. It achieves a maximum value of F_2 equal to 1.64 at 350 nm, which is more than sufficient to support high quality resonances [105]. This is further illustrated by the numerically simulated optical response of subwavelength period nano-grating metasurfaces of varying composition presented in Figure 2.24: the resonance observed in reflection mode has a higher quality-factor for $Bi_5Sb_3Te_2$ compared with other compositions that have a lower F_2. As a high-index dielectric, BST comes into its own at near-IR wavelengths, with values of F_3 (Figure 2.22) exceeding those of TCOs above ~1220 nm. The highest figures of merit are offered by the binary composition Sb_3Te_8 – values come within a factor of 2 of those of germanium (at around 700-800nm), though by virtue of losses are much lower than those of silicon. This value of F_3 is sufficient to support high dielectric Mie resonances as presented in Figure 2.25. Within the compositional range accessible to the present study, $Bi_5Sb_3Te_2$ is identified as the best plasmonic stoichiometry (highest figures of merit for both propagating and localized surface plasmon modes). Near-IR refractive indices as high as n = 11.5 are found in certain ternaries but Sb_3Te_8 presents the

highest ratio of refractive index to extinction coefficient (as a figure of merit for high-index dielectric applications). All compositions have a near- or sub-unity minimum value of refractive index in the near-UV range (the lowest measured value being n = 0.7 at 296 nm for $BiSb_3Te$); $Bi_2Sb_5Te_{18}$ provides a value of epsilon $|\varepsilon|$ that is nearest to zero ($|\varepsilon|$ = 2.27 at 230 nm).

BST is of course only one member of a large extended family of chalcogenide materials, which remain to be explored for their nanophotonic applications potential. High-throughput combinatorial techniques, as presented here, can enables rapid, systematic surveys of optical, electronic and structural properties, and thereby optimization via compositional design of material characteristics towards specific application requirements.

Chapter 3

Plasmonic and Phase Change Properties of Bi:Te for Metamaterials Application

3.1 Introduction

From the ternary space described in the previous chapter, here I focus on Bi:Te, one of the corresponding binary alloys of BST. In particular, I show that amorphous thin films of Bi:Te exhibit a plasmonic response at near-UV to visible frequencies, with the real part ε_1 of its relative permittivity taking a negative values over a composition-dependent range of wavelengths extending from as low as 250 nm to as high as 978 nm. We demonstrate this plasmonic response via the fabrication and characterization of planar metamaterial structures. Moreover, we study also the phase change properties of this alloy, namely the change of optical properties related to the phase transition from amorphous to crystalline phase as a function of composition.

3.2 Fabrication of Nanostructures

Bismuth telluride (Bi_2Te_3) is widely known as an excellent thermoelectric material (thermoelectrics are materials able to generate small voltages due to a temperature difference; the underlying physical mechanism is called Seebeck effect), possessing a thermoelectric figure of merit (defined in literature as *ZT*) close to 1 (one of the highest value reported in literature) [114]. Moreover, Bi_2Te_3 is a narrow band gap semiconductor with high density of states near the band edges and low thermal conductivity. It has attracted renewed interest since its discovery as a 3D topological insulator [115], and in the form of chemically grown crystalline nanoplates has been observed to support surface plasmon modes in the visible wavelength range [116]. Its UV/visible plasmonic response is demonstrated here in the first instance by variable angle spectroscopic ellipsometry measurements of relative permittivity (ε), such as presented in Figure 3.1a: the real part (ε_1) takes a negative value, as

is required to support surface plasmons at an interface with a dielectric, between wavelengths λ_1 and λ_2 at which it is equal to zero (250 nm and 660 nm respectively in the example shown – a composition of 34% Bi and 66% Te, evaluated by energy-dispersive x-ray spectroscopy – see Figure 3.3a). As already defined in the previous chapter, here in Figure 3.1b we consider explicitly the plasmonic figure of merit F_1 (defined as Eq. (2.15) in section 2.5.4) – for amorphous Bi:Te alongside a number of other, noble metals and a recently-proposed alternative plasmonic media [111]. Bi:Te cannot match the values of F_1 exhibited by aluminium or silver at visible wavelengths (though Figure 3.1b ignores the fact that their surfaces will oxidize/tarnish in air), but its F_1 value is higher than that of titanium nitride across the entire visible range (TiN being plasmonic only down to 500 nm), and to gold from 550 nm down to 350 nm.

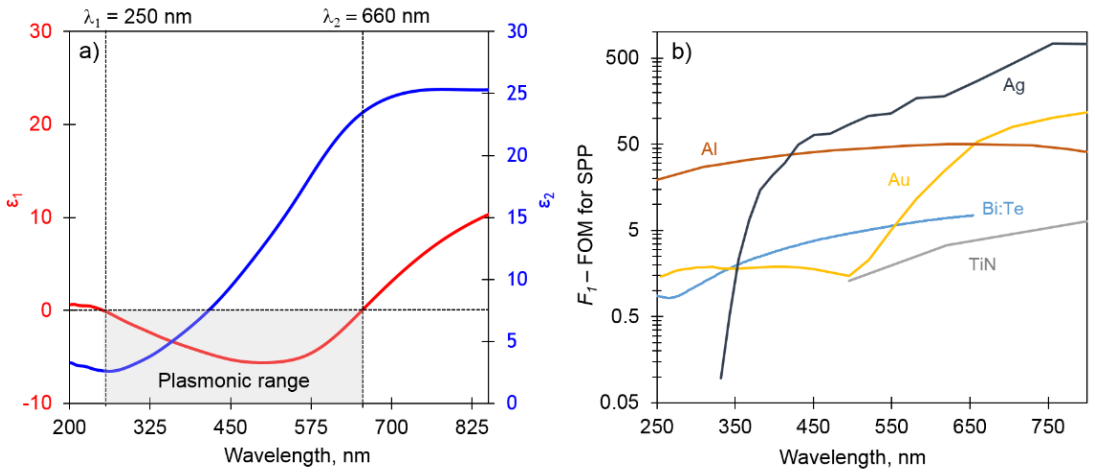

Figure 3.1: UV and visible plasmonics in amorphous Bi:Te. a) Spectral dispersion of the relative permittivity of as-deposited amorphous bismuth telluride evaluated by variable angle spectroscopic ellipsometry for a 134 nm thick film of Bi[34%]:Te[66%] on a sapphire substrate. b) Spectral dispersion of plasmonic figure of merit (F_1 defined in Eq. (2.15)), section 2.5.4) for amorphous as-deposited Bi(34%):Te(66%) and a selection of other plasmonic materials - as labelled; calculated using material parameters from Ref. [107, 108].

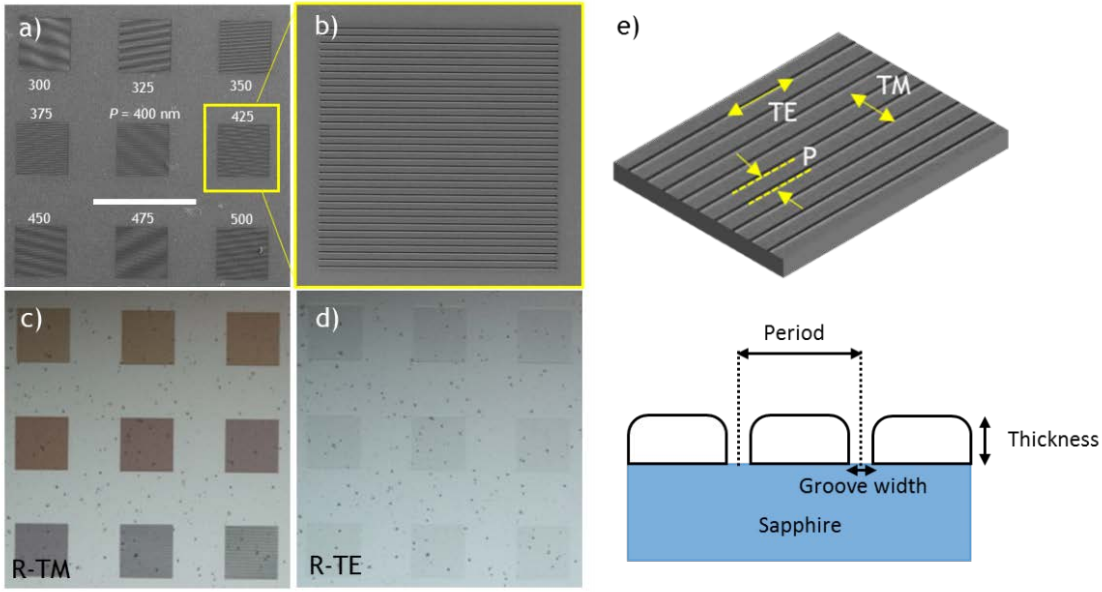

Figure 3.2: Amorphous bismuth telluride metasurfaces. a, b) Scanning electron microscopy images of nano-grating metasurfaces in 134 nm Bi(34%):Te(66%) with periods ranging from 300 – 500 nm (as labelled; scale bar in (a) = 40 µm). c, d) Corresponding reflection mode optical microscopy images for c) TM and d) TE polarized incident light. e) Schematic representation of the nano-grating metamaterial structure.

The plasmonic character of amorphous Bi:Te is demonstrated through the fabrication of planar metasurfaces presenting absorption resonances in the visible range, specifically sub-wavelength period (i.e. non-diffractive) grating structures akin to those recently proposed for applications such as active nanophotonics photodetectors [117] and colour-tunable photovoltaics [118]. Optically thick (transmission <1%) Bi:Te films were deposited on optically flat sapphire substrates (pre-baked at 150 °C for 30 minutes) by using the high-throughput PVD system described in Chapter 2. Film thickness is measured using a stylus profilometer. The amorphous nature of the as-deposited films is verified by x-ray diffraction (Figure 3.3). For comparison, the corresponding angular spectrum for the polycrystalline state (after annealing at 200°C for 30 minutes) is also presented. In the as-deposited thin film, only a weak peak can be observed at 27°, this can be attributed to the presence of Bi and Te nano-grains embedded in amorphous bismuth telluride matrix. In fact, the XRD peak of Bi (012) plane is located at 27.18° and the peak of Te (101) plane is found at 27.56° [119].

Nano-grating metasurface patterns, with a fixed linewidth *L* of nearly 100 nm and periods *P* ranging from 300 nm to 500 nm, each covering an area of approximately 20 µm × 20 µm, were etched through the Bi (34%):Te(66%) layer by focused ion beam (FIB) milling [118].

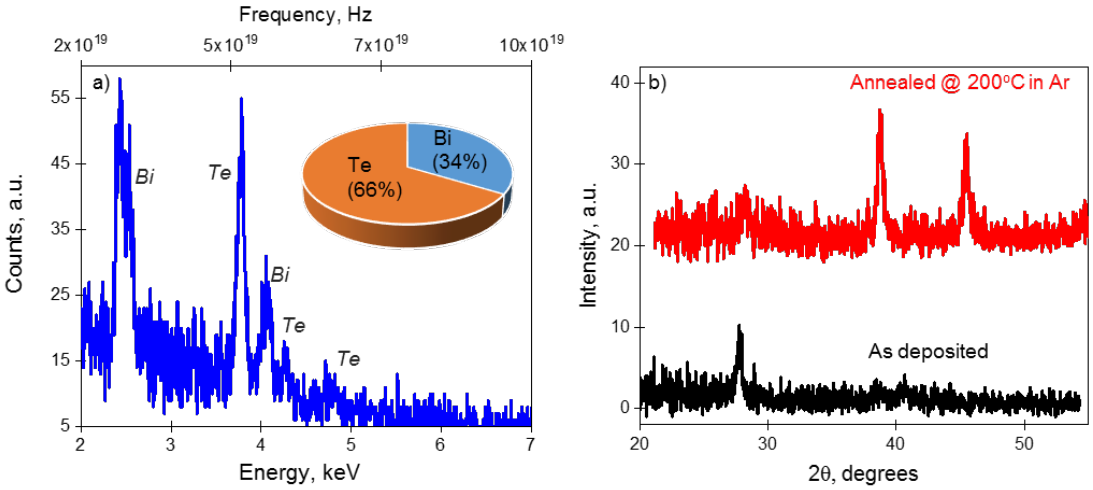

Figure 3.3: Composition and structural phase of vapour deposited Bi:Te thin films. a) Alloy composition (Bi:Te at.% ratio) is determined by energy-dispersive x-ray spectroscopy. The example shown is for a composition of Bi 34% and Te 66%. Quantitative analysis of elements in any sample requires the measurements of the peak intensities; once these intensities have been determined, a comparison is made with standards of known composition and matrix corrections are applied in order to obtain the concentration of each element inside the analysed sample [120]. b) The amorphous nature of the as-deposited films is verified by x-ray diffraction. For comparison, the corresponding angular spectrum for the polycrystalline state (after annealing at 200°C for 30 minutes) is presented (vertically offset for clarity). In the as-deposited thin film, only a weak peak can be observed at 27°, this can be attributed to the presence of Bi and Te nano-grains embedded in amorphous bismuth telluride matrix. In fact, the XRD peak of Bi (012) plane is located at 27.18° and the peak of Te (101) plane is found at 27.56° [119].

3.3 Results and Discussion: Optical Spectra and Simulations

Normal-incidence optical characteristics of the Bi:Te nano-grating metasurfaces were subsequently quantified using a microspectrophotometer (CRAIC QDI2010) with a sampling domain size of 15 µm × 15 µm, for incident polarizations parallel and perpendicular to the grating lines (TE and TM orientations of the grating respectively, as indicated in the inset to Figure 3.4a).

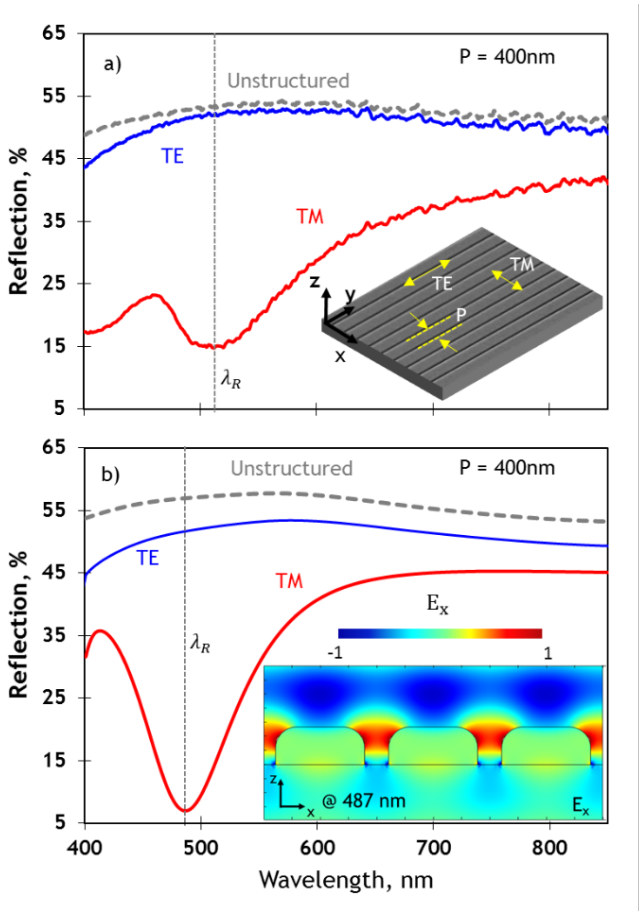

Figure 3.4 Optical response of amorphous Bi:Te nano-grating metasurface. a) Measured spectral dispersion of normal incidence reflectivity for a 400 nm period amorphous Bi (34%):Te (66%) nano-grating metasurface for TM and TE-polarized incident light, and the corresponding (polarization-independent) spectrum for unstructured Bi:Te. The inset schematic illustrates TM/TE polarization orientations and coordinate axes as used in numerical simulations. b) Numerically simulated spectral dispersion of normal incidence reflectivity related to the corresponding experimental spectra shown in panel a). The inset presents the numerically simulated distribution of the x-component of electric field in the xz plane at the 487 nm TM resonance wavelength of the P = 400 nm nano-grating metasurface.

Unstructured amorphous Bi:Te has spectrally near-flat reflectivity close to 50% across the near-UV to near-IR spectral range, as shown in Figure 3.4a. Nano-grating metasurface structures introduce plasmonic resonances for TM polarized light (incident electric field perpendicular to the grating lines) which manifest themselves as period-dependent "structural colours" (Figure 3.2c), while no resonances are observed for TE polarized light – indeed, under TE illumination the nano-grating domains are almost indistinguishable from unstructured Bi:Te (Figure 3.2d).

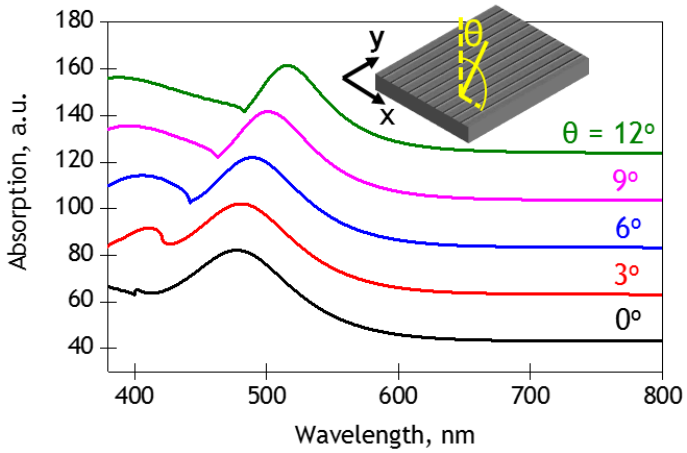

Figure 3.5: Metasurface resonances at off-normal incidence. Numerically simulated TM-polarization transmission spectra for a 134 nm thick Bi (34%):Te(66%) nano-grating metamaterial, with a period P = 400 nm and slot width L = 100 nm, for a selection of incident angles θ (as labelled; vertically offset in 20% steps for clarity). Nano-grating resonances are split as a result of the structures' sensitivity in this orientation to the incident angle of light (breaking of spatial symmetry with deviation from normal incidence). The microspectrophotometer used for experimental measurements (Figure 3.4) employs an objective with a numerical aperture of 0.28, thereby illuminating samples at incident angles θ ranging from zero to ~16°. Assuming an incident angle of 9° in simulations is found to give the best fit to experimental spectra.

The nature of the TM resonance is illustrated via 3D finite element (Comsol Multiphysics) numerical simulations: these employ ellipsometrically measured material parameters for Bi:Te (Figure 3.1a) and a free-space structure is adopted. They assume normally incident narrowband plane wave illumination in the *–z* direction and, by virtue of periodic boundary conditions, a grating pattern of infinite extent in the *xy* plane. The TM plasmonic resonance is characterized by a local enhancement of field in the milled slots of the nano-grating structure (Figure 3.4b, inset). The small spectral offset between measured and numerically simulated resonance (reflection minimum in Figure 3.4) wavelengths λ_R is ascribed primarily to the fact that experimental data is obtained with a focused microspectrophotometer probe beam as opposed to the (computationally assumed) normally incident plane wave. In fact, we study the influence of the incident angle on the metamaterial resonance and show the corresponding absorption spectra from normal incidence to an incident angle up to 12° in Figure 3.5. These simulations reveal that as the incident angle rises the absorption peak shifts continuously to longer wavelengths and we notice that an off-normal incident angle of 9° more realistically represent the focused probe beam produced by the microspectrophotometer's objective lens as reveal the comparison between experimentally measured and simulated spectra in Figure 3.6. Instead, there is no localization or enhancement of field under TE illumination. The spectral tuning of TM resonance wavelength with nano-grating period, shown in Figure 3.6a, is accurately reproduced by the

computational model (Figure 3.6b), with minor discrepancies between experiment and simulation being attributed to manufacturing imperfections and inhomogeneity (deviations from the ideal model geometry, such as slight over-milling of grating lines into the substrate) and some implantation of gallium into the Bi:Te during FIB milling, likely to effect a small change in refractive index.

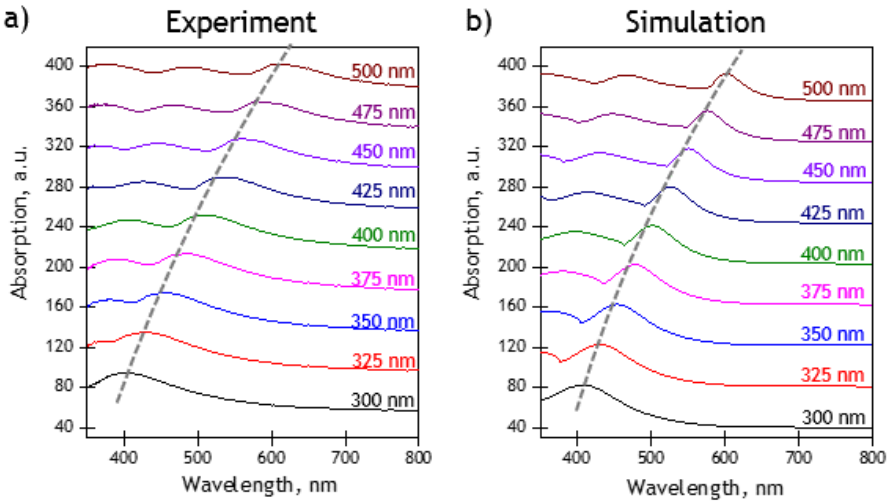

Figure 3.6: Structural tuning of amorphous Bi:Te metasurface resonance wavelength. a) Measured and b) numerically simulated spectral dispersion of Bi (34%):Te (66%) nano-grating metasurface TM-mode absorption for grating periods P ranging from 300 nm to 500 nm (as labelled; vertically offset in 40% steps for clarity). Numerical spectra are evaluated for an off-normal incident angle of 9°, as opposed to normal incidence, to more realistically represent the focused probe beam produced by the microspectrophotometer's objective lens – see Figure 3.5.

3.4 Compositional-Dependent Optical Properties

Thus far we have considered a single Bi:Te composition with atomic percent concentration of 34% Bi and 66% Te. Varying composition though has a profound effect on the optical properties of the alloy, providing an effective means of controlling the wavelengths at which $\varepsilon_1 = 0$, and therefore the spectral band over which the material is plasmonic (i.e. has a negative value of ε_1), as well as the corresponding losses (ε_2). By employing "wedge shutters" which partially shadow the elemental deposition sources [118], thin film samples are produced in which the Bi:Te at.% ratio varies continuously as a function of position over the substrate, from 1.6 to 17. This high-throughput approach enables for rapid, systematic mapping of material parameters, i.e. complex relative permittivity, measured by variable-angle spectroscopic ellipsometry as a function of position, to composition (Figure 3.7a, b).

While the near-UV ε_1 zero-crossing wavelength λ_1 and losses at this point are found to be largely invariant as a function of alloy composition, the longer zero-crossing wavelength λ_2, and associated losses are strong functions of the compositional ratio (Figure 3.7c, d): λ_2 red-shifts as the ratio increases, i.e. as the proportion of bismuth increases. In the present case it is tuned from 530 nm at a Bi:Te ratio of 0.06 to 978 nm at 0.60. As such the width of the alloy's plasmonic band increases with compositional ratio (Figure 3.7c) to encompass the entire visible spectral range at higher Bi:Te ratios, though losses (ε_2) at longer wavelengths also increase with said ratio (Figure 3.7d).

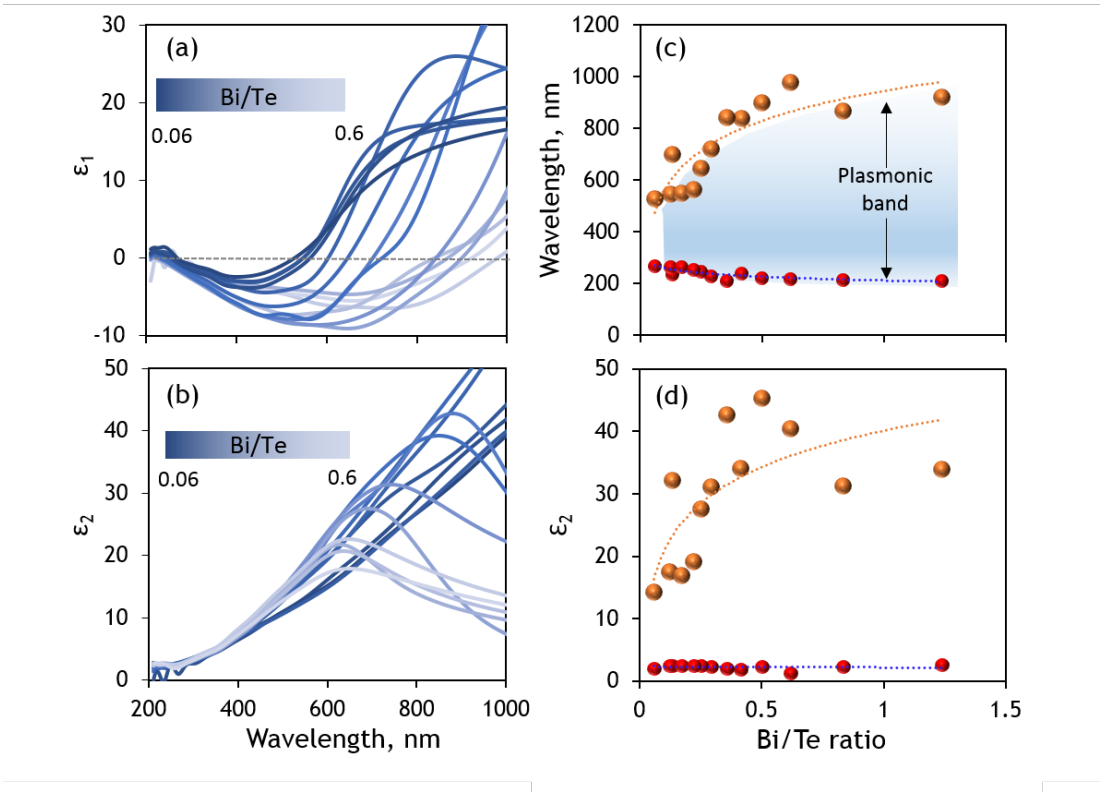

Figure 3.7: Compositional tuning of Bi:Te optical properties. a, b) Spectral dispersion of the a) real and b) imaginary parts of relative permittivity for as-deposited amorphous Bi:Te across a range of Bi:Te at.% compositional ratios, evaluated via variable angle spectroscopic ellipsometry. c, d) Dependence on Bi:Te ratio of c) the wavelengths at which the real part of relative permittivity $\varepsilon_1 = 0$, and d) corresponding values of ε_2. Red dots refer to the shorter wavelengths crossover point while orange dots refer to the longer wavelengths crossover point.

The composition-dependent properties of Bi:Te is further demonstrated via the fabrication of planar metasurfaces (described in section 3.2) across four different compositions. The optical response of these metasurfaces was measured using a microspectrophotometer (CRAIC QDI2010) and plasmonic resonances are observed in TM-mode absorption for a nano-grating period of 400 nm within 4 different compositions as shown in Figure 3.8a. The spectral position of these resonances varies from 495 nm to 550 nm by changing only the

compositions of the metasurfaces. Moreover, we observe a clear change in the Q-factor of these resonances from a maximum value of 7.5 to a minimum of 4.5. This variation of the Q-factor follows the same trend of F_2, defined as $F_2 = |\varepsilon_1|/\varepsilon_2$ (Eq. (2.16), section 2.5.4), as represented in Figure 3.8b, meaning that this figure of merit characterize the material's ability to support high-quality localized surface plasmon resonances (LSPR) not only in spherical nanoparticles, but also in metasurfaces. Hence, F_2 can be used to predict the performance of the corresponding metasurface starting from the constitutive parameters ε_1 and ε_2.

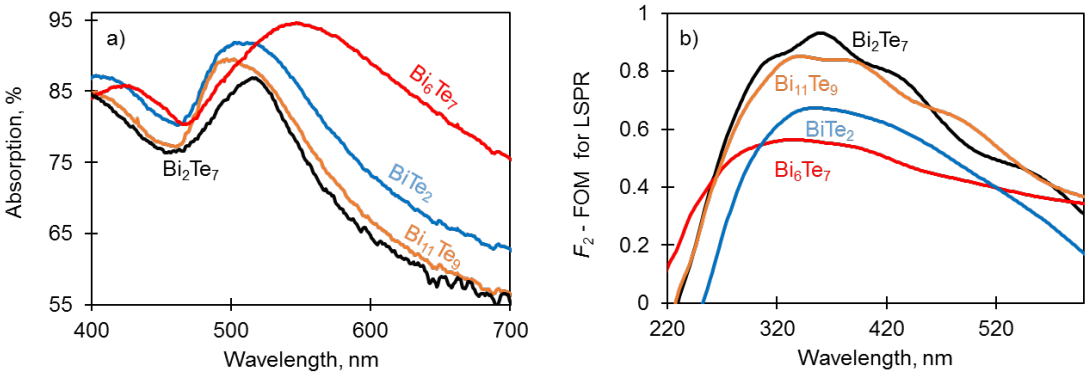

Figure 3.8: Optical response of amorphous Bi:Te nano-grating metasurfaces across different compositions. a) Measured spectral dispersion of Bi:Te metasurfaces in TM-mode absorption for a period of 400 nm within 4 different compositions. b) Dispersion of figure of merit for localized surface plasmon resonances (LSPR), defined as $F_2 = |\varepsilon_1|/\varepsilon_2$ (Eq. (2.16), section 2.5.4), calculated for the same Bi:Te compositions used for the fabrication of metasurfaces.

3.5 Phase Change Properties of Bi:Te Thin Films

In recent years, the extension of metamaterial paradigm from passive devices to functional metamaterials drove the exploration of phase change materials as constitutive media for active metamaterials [121]. Hence, this class of materials enables the creation of optical metasurfaces with adjustable parameters where their optical response can be modified by external stimuli such as heat, stress, electrical fields or optical pulses [121]. In this work, we adopt the definition of phase change materials from ref. [121], namely they are materials characterized by fast phase change transition (crystallization and amorphization) on laser irradiation that is associated with a significant non-volatile change of optical properties. Chalcogenides usually present this phase change property [52] and the physical origin of this large change of the dielectric function is associated with a change in the chemical bonding on the transition from the amorphous to the crystalline state [121]. Specifically, phase

change materials in the crystalline phase have a rocksalt-like crystal structure where each atom has an average coordination number of six [121, 122], but only three valence electrons meaning that these electrons are not sufficient to saturate all six covalent bonds. Hence, two nearest-neighbours atoms are linked by only one electron and this peculiar chemical bond is called resonant bonding [121, 122]. A very important feature of resonant bonding is that the electron density distribution is highly delocalized and so these electrons are highly polarizable resulting in materials with large optical dielectric constant. Instead, phase change materials in the amorphous state have a different atomic arrangement compared to the respective crystalline phase and ordinary covalent bonds are formed. Therefore, the electronic polarizability is much lower in the amorphous phase resulting in a material with a smaller dielectric constant. Overall, this mechanism explains why phase change materials in the crystalline form show a much higher reflectivity that the corresponding amorphous phase.

Bismuth telluride (Bi_2Te_3) is part of the chalcogenide materials family and recent first principle calculations have shown that this compound presents a resonant bonding in its crystalline phase, but due to a small structural distortion from the rocksalt-like structure the resonant bonding exists in a weakened form compared with other well-known phase change materials like GST ($Ge_2Sb_2Te_5$) and GeTe [122]. Moreover, another recent work demonstrated experimentally that bismuth telluride in the form of chemically grown crystalline nanoplates [116] and nanowires [123] is a phase change material since a pronounced change on electrical and optical properties is observed in the phase transition between the crystalline and the amorphous state. However, a different study based on experimental and first principle calculations illustrated that thin films of Bi_2Te_3 do not exhibit phase change properties [124].

Here we investigate the change on the optical properties of combinatorial thin film of Bi:Te with a composition ranging from 45 % < Te < 95 % and correspondingly 55 % < Bi < 5 % and this study is motivated by the inconsistency of the works reported so far in literature and the lack of data for Bi:Te system with different stoichiometry than Bi_2Te_3.

As already described in section 3.4, combinatorial thin films of Bi:Te were deposited via the high-throughput deposition system introduced in section 2.2. The structural properties of these films were investigated by XRD and Raman spectroscopy used in conjunction with EDX to determine the composition. Figure 3.9 reports the XRD diffractograms and corresponding Raman spectra for representative compositions of combinatorial as-deposited Bi:Te film. In the as-deposited combinatorial thin film, only a weak peak can be observed at nearly 27^o, this can be attributed to the presence of Bi and Te nano-grains embedded in amorphous bismuth telluride matrix. In fact, the XRD peak of Bi (012) plane is located at 27.18^o and the

peak of Te (101) plane is found at 27.56° [119]. The amorphous nature of these films is further confirmed by Raman spectra since they present only broad peaks typical of amorphous solids.

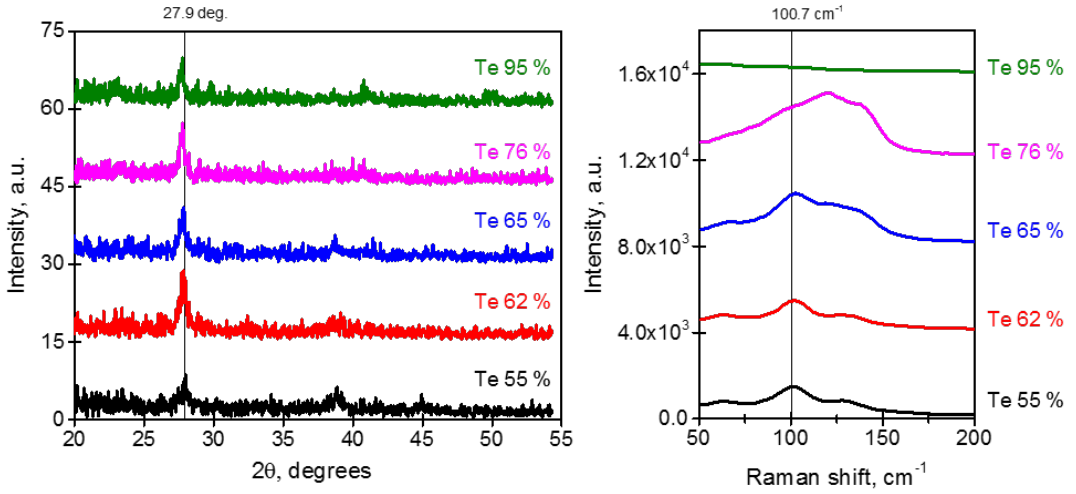

Figure 3.9: Structural properties of as-deposited combinatorial Bi:Te film for representative compositions. XRD diffractograms (on the left) and corresponding Raman spectra (on the right) for representative compositions of combinatorial as-deposited Bi:Te film. Inside each panel XRD diffractograms and Raman spectra are plotted using a vertical offset and are labelled according to the corresponding compositions. Each curve is labelled with the atomic percent concentration of Te, the respective Bi concentration can be calculated as $C_{Bi,\,at.\%} = (100 - C_{Te,\,at.\%})$.

The as-deposited combinatorial Bi:Te film is then annealed at 200°C for 30 minutes in a furnace flooded with argon. The corresponding XRD diffractograms and Raman spectra are reported in Figure 3.10 revealing the appearance of sharper peaks typical of polycrystalline phases for both measurements. Specifically, XRD diffractograms (Figure 3.10) show peaks at 38.8° and 45.5° attributable to diffraction from (1010) and (0015) crystal planes [125] for Te content (atomic percent) between 55% and 65%. Instead, at higher Te content we observe a peak at nearly 45° for Te concentration of 76% and peaks at 28.2° and closely to 39° for 95% Te. These peaks can be ascribed to crystalline Te [104]. Raman spectra (Figure 3.10) present the typical peaks of the Bi_2Te_3 crystal phase for Te concentration of 55% and 62%, namely these peaks are observed at 57.4 cm^{-1}, 96.8 cm^{-1} and 125.9 cm^{-1} corresponding to the A_{1g}^1, E_g^2 and A_{1g}^2 modes (see Table 2.1). At larger Te concentrations, the peaks at 57.4 cm^{-1} and 96.8 cm^{-1} are still visible for Te content of 65% and 76%, but other two peaks appear at 116 cm^{-1} and 135 cm^{-1} ascribable to pure Te [101]. For Te concentration of 95% only two broad peaks are observed at nearly 100 cm^{-1} and 125 cm^{-1} revealing that this composition seems partially crystallized. Nevertheless, annealing the combinatorial thin film at 200°C causes the crystallization of most of the compositions enclosed in the sample, in particular the ones close to Bi 40% and Te% that we want to study for the phase change properties. Furthermore, as reported in ref. [125], annealing at temperatures higher than 200°C resulted

in the appearance of large grain size polycrystalline structures that we prefer to avoid, because large grains can enhance the scattering and the absorption loss of the film reducing the quality of the film for optical application. Furthermore, annealing at higher temperatures can deplete the film of Te content, since Te atoms are lighter and more volatile than Bi atoms and so at high temperatures these atoms can sublimate [126]. For these reasons, we used a maximum temperature of 200°C and we checked the composition via EDX of the combinatorial Bi:Te film before and after the annealing observing that the composition remains the same of the as-deposited sample after the annealing.

Overall, it seems that in the compositional range investigated here, only the Bi_2Te_3 crystal phase is formed in agreement with ref. [104], since XRD diffractograms and Raman spectra show only the peaks typical of this crystallographic phase. The crystal structure for compositions with stoichiometry close to Bi_2Te_3 can be explained by the presence of antisite defects, namely Te atoms can occupy Bi lattice positions for Te-rich compositions and vice versa for Bi-rich compositions. For higher content of Te, it is possible that excess Te segregates out of the film to form regions of pure Te according to ref. [127] and Raman spectra reported in Figure 3.10.

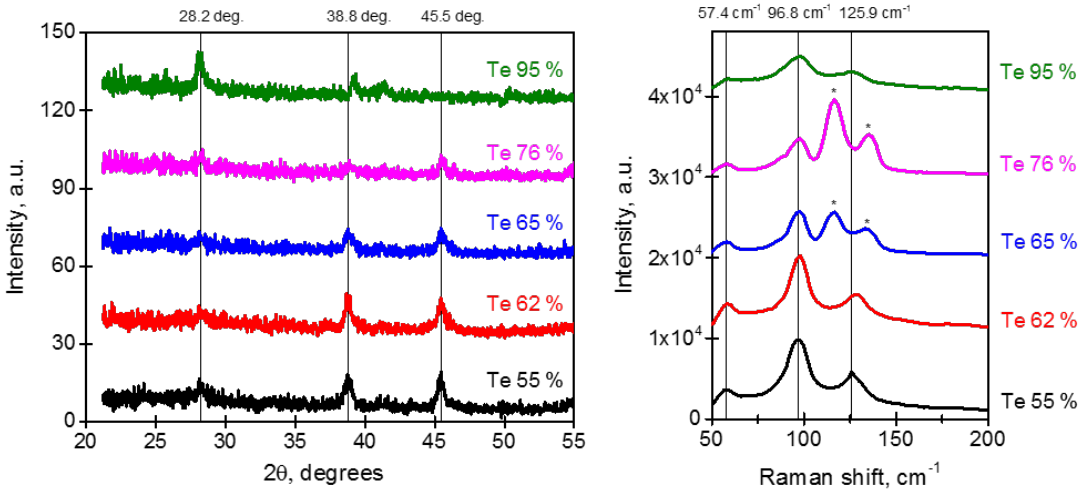

Figure 3.10: Structural properties of furnace annealed combinatorial Bi:Te film for representative compositions. XRD diffractograms (on the left) and corresponding Raman spectra (on the right) for representative compositions of combinatorial Bi:Te film annealed at 200°C for 30 minutes in argon flux. Inside each panel XRD diffractograms and Raman spectra are plotted using a vertical offset and are labelled according to the corresponding compositions. Each curve is labelled with the atomic percent concentration of Te, the respective Bi concentration can be calculated as $C_{Bi,\,at.\%} = (100 - C_{Te,\,at.\%})$.

The optical constants of the as-deposited and annealed Bi:Te film were extracted by variable-angle ellipsometry for wavelengths comprised between 210 nm and 1686 nm and are shown in Figure 3.11. The comparison between the dielectric function of amorphous (as-deposited)

and polycrystalline (annealed) phases across different compositions reveals a modest change in the optical properties; however, a larger change is observed for compositions around Te content of 75% (Bi 25%) suggesting that Bi:Te material system presents phase change properties for these compositions, but in a weaker form compared to other well-known phase change materials like $Ge_2Sb_2Te_5$ and GeTe [122]. Moreover, these phase change properties might be associated with Te segregation after the annealing that results in the formation of a material with two mixed phases, namely polycrystalline Bi_2Te_3 and polycrystalline Te.

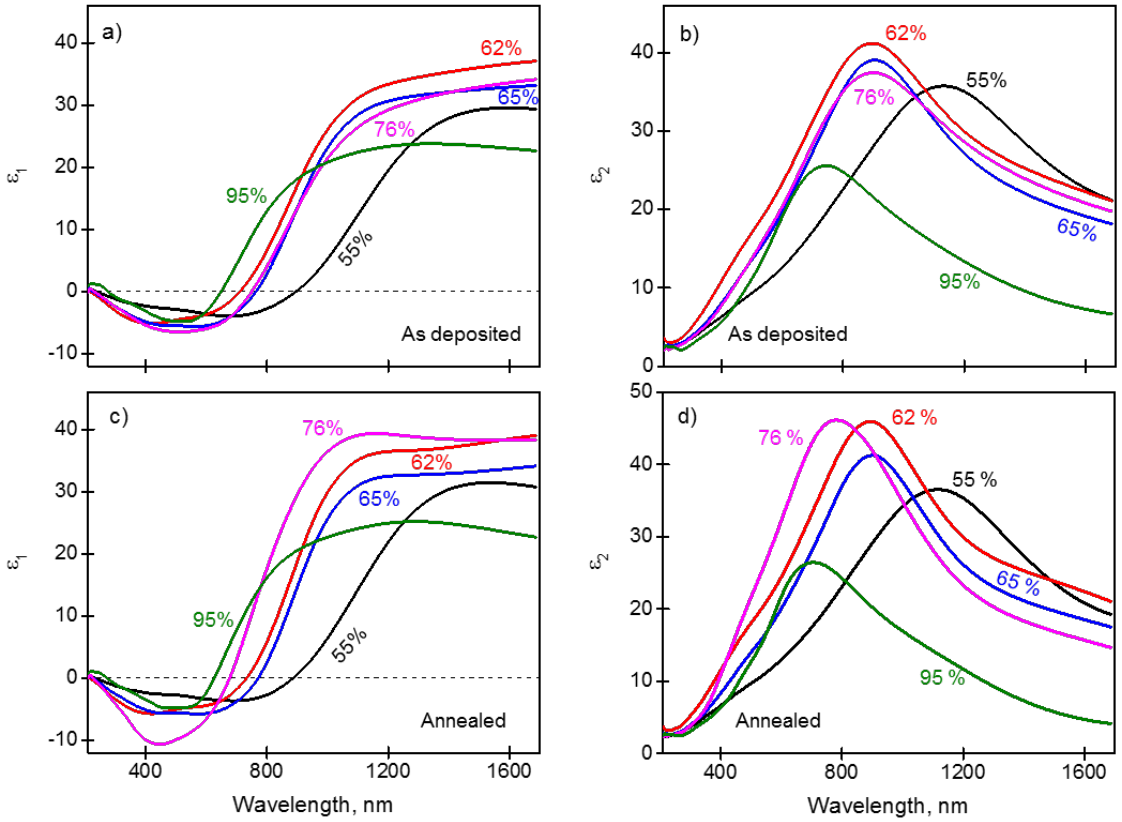

Figure 3.11: Dispersion of optical properties of as-deposited and furnace annealed combinatorial Bi:Te film for representative compositions. Real a) and imaginary b) part of the dielectric function across different composition of as-deposited combinatorial Bi:Te film. c, d) Corresponding real and imaginary part of the dielectric function for the annealed combinatorial Bi:Te film. Each curve is labelled with the atomic percent concentration of Te, the respective Bi concentration can be calculated as $C_{Bi,\,at.\%} = (100 - C_{Te,\,at.\%})$.

In order to quantify the change of the optical properties related to the phase transition of Bi:Te, we first extract the wavelengths at which the real part (ε_1) of the dielectric function is equal to zero (cross-over points) and we plotted them as a function of Te concentration (in atomic percent) for the as-deposited (Figure 3.12a) and annealed (Figure 3.12b)

combinatorial Bi:Te film. Overall, the trend observed in both cases is similar, namely the cross-over point tend to move toward shorter wavelengths as Te concentration is increased.

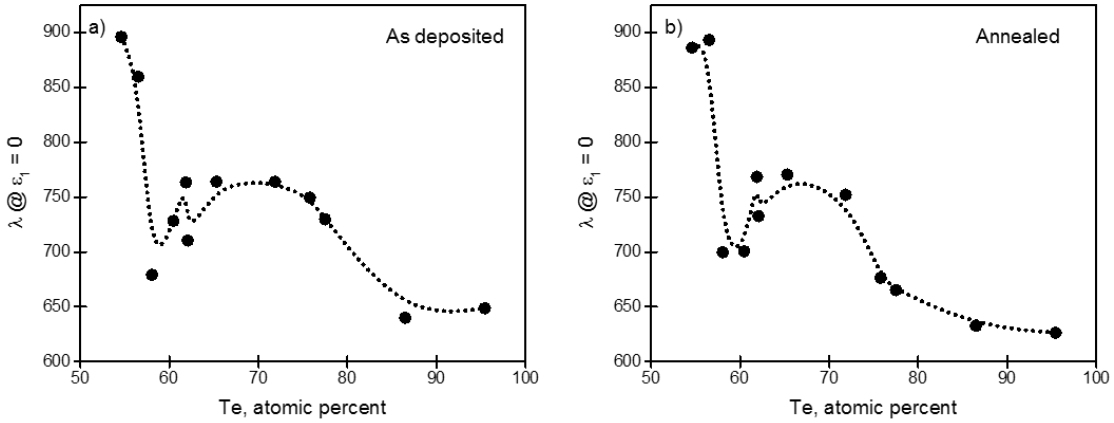

Figure 3.12: ENZ properties of combinatorial Bi:Te film vs composition. Wavelengths at which the real part *(ε_1)* of the dielectric function is equal to zero (cross-over points) plotted as a function of Te concentration (in atomic percent) for the as-deposited a) and annealed b) combinatorial Bi:Te film. The dotted lines are trending curves obtained using b-splines connecting the cross-over points extracted from the ellipsometrically measured dielectric functions across different compositions.

Secondly, we evaluate the plasmonic properties of Bi:Te alloy by calculating the maximum value of the figure of merit for localized surface plasmon resonances (LSPR), defined as $F_2 = |\varepsilon_1|/\varepsilon_2$ (Eq. (2.16), section 2.5.4), as a function of Te concentration (in atomic percent) for as-deposited (Figure 3.13a, black points) and annealed (Figure 3.13a, red points) combinatorial Bi:Te film. In both cases, the larger values of F_2 are observed for compositions in the range between 72% and 78% content of Te while the value of F_2 diminishes for compositions with lower and higher Te content. The change in F_2 associated with the phase transition from the amorphous to the crystalline state is assessed in Figure 3.13b and reveals that the maximum percentage change is of 55% for the composition with Bi 24% and Te 76%. We also observe some slightly negative values in Figure 3.13b for certain compositions that can be ascribed to some errors in the process of the extraction of the optical constants from ellipsometry revealing that for these compositions the change in the plasmonic properties is in the order of few percent.

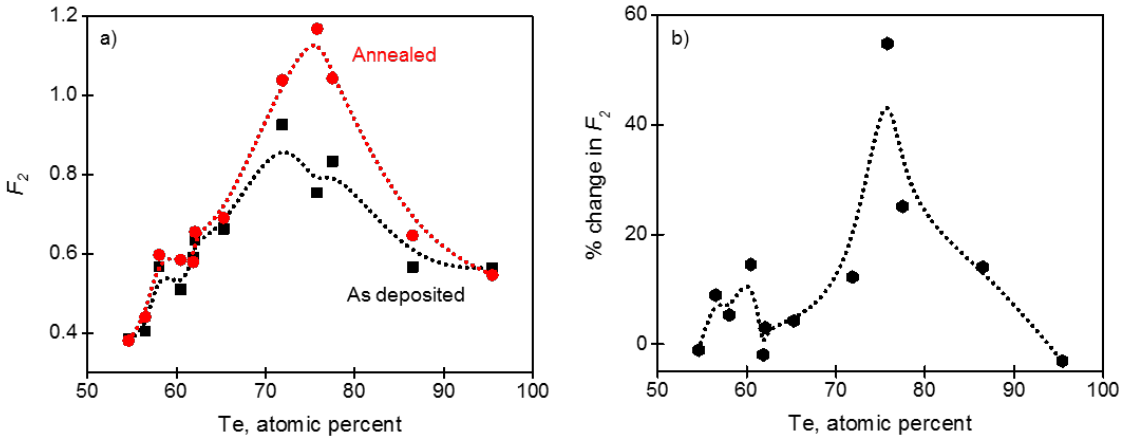

Figure 3.13: Plasmonic properties of combinatorial Bi:Te film vs composition. a) Maximum value of the figure of merit for localized surface plasmon resonances (LSPR), defined as $F_2 = |\varepsilon_1|/\varepsilon_2$ (Eq. (2.16), section 2.5.4), plotted as a function of Te concentration (in atomic percent) for as-deposited (black points) and annealed (red points) combinatorial Bi:Te film. b) Percentage change in F_2 between the as-deposited and annealed Bi:Te film plotted as a function of Te concentration (in atomic percent). The dotted lines are trending curves obtained using b-splines connecting the corresponding scatter points.

Thirdly, we estimate the change in the optical properties at longer wavelengths (λ > 1000 nm) where Bi:Te behaves as a lossy dielectric using the figure of merit for dielectric Mie resonances, defined as $F_3 = n/4\pi\kappa$ (Eq. (2.16) section 2.5.4), extracted at telecom wavelengths (Figure 3.14) plotted as a function of Te concentration (in atomic percent) for as-deposited (Figure 3.14a) and annealed (Figure 3.14b) combinatorial Bi:Te film. For both the as-deposited and annealed film we notice that F_3 is higher at 1550 nm than 1310 nm and it tends to increase as Te content rises, since pure crystalline Te is a good dielectric material in the near and mid-IR [40]. The change in F_3 related to the phase transition from the amorphous to the crystalline state is reported in Figure 3.13b and shows that the maximum percentage change is of 88% at 1550 nm for the composition with Bi 14% and Te 86%. Instead, for compositions with lower content in Te the percentage change in F_3 is smaller with a minimum value of 4% for Te 62% (Bi 38%).

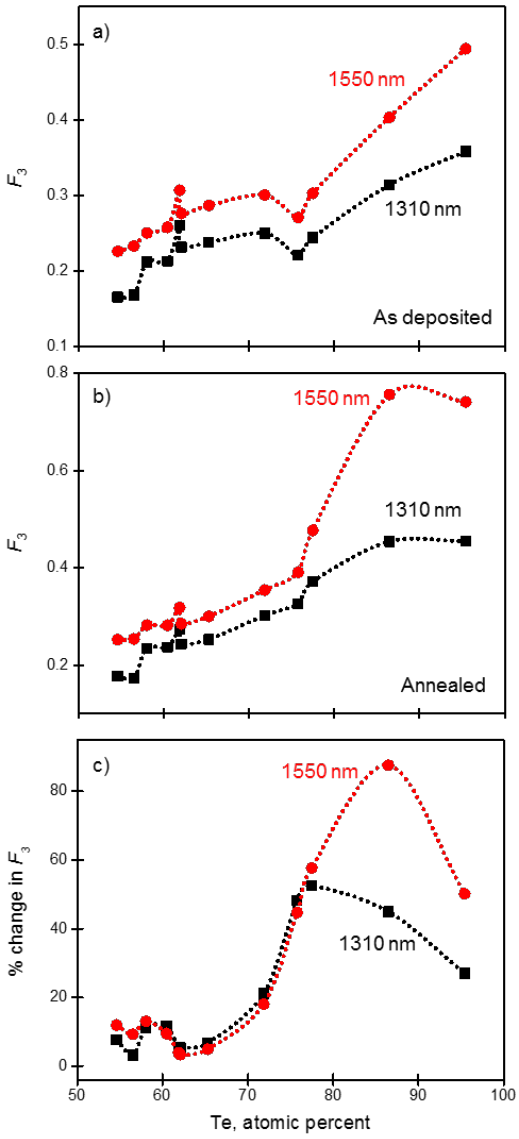

Figure 3.14: Dielectric properties of combinatorial Bi:Te film vs composition. Figure of merit for dielectric Mie resonances, defined as $F_3 = n/4\pi\kappa$ (Eq. (2.16) section 2.5.4), extracted at telecom wavelengths (1310 nm, black points and 1550 nm, red points) plotted as a function of Te concentration (in atomic percent) for as-deposited a) and annealed b) combinatorial Bi:Te film. c) Percentage change in F_3 between the as-deposited and annealed Bi:Te film plotted as a function of Te concentration (in atomic percent) for telecom wavelengths.

The application of Bi:Te as phase change material for functional metamaterial application is illustrated by the numerical simulation (using the same model described in section 3.3) of the optical response of Bi:Te nano-grating metasurfaces considering the optical constants obtained for the as-deposited (amorphous) and the annealed (polycrystalline) thin film with composition Bi 24% and Te 76% that is the one with the highest percentage change in F_2. Reflection spectra are reported in Figure 3.15 showing that the plasmonic resonance has a spectral shift of 15 nm.

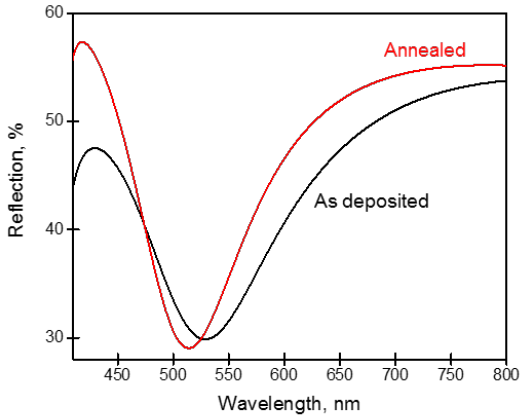

Figure 3.15: Phase change properties of Bi:Te nano-gratings metasurfaces. Comparison of reflection spectra numerically simulated for subwavelength nanogratings with period of 300 nm, thickness 134 nm and groove width of 50 nm with incident light polarized in the direction opposite to the grating grooves between as-deposited and annealed film with composition Bi 24% and Te 76%.

In conclusion, the study of the change on the optical properties of combinatorial thin film of Bi:Te with a composition ranging from 45 % < Te < 95 % and correspondingly 55 % < Bi < 5 % reveals an overall modest variation of the dielectric function related to the phase transition between the amorphous and the crystalline state. To quantify this change we evaluate the plasmonic properties of Bi:Te alloy by calculating the maximum value of the figure of merit for LSPR, F_2, for as-deposited and annealed combinatorial film; the maximum percentage change is 55% for the composition with Bi 24% and Te 76%. Furthermore, we estimate the change in the optical properties at longer wavelengths (λ > 1000 nm) using the figure of merit for dielectric Mie resonances, F_3, and the maximum percentage change related to the phase transition from the amorphous to the crystalline state is of 88% at 1550 nm for the composition with Bi 14% and Te 86%. Instead, for compositions with lower content in Te the percentage change in F_3 is smaller with a minimum value of 4% for Te 62% (Bi 38%).

These results suggest that Bi:Te material system presents phase change properties for these compositions, but in a weaker form compared to other well-known phase change materials like $Ge_2Sb_2Te_5$ and GeTe [122]. Moreover, these phase change properties might be associated with Te segregation after the annealing that results in the formation of a material with two mixed phases, namely polycrystalline Bi_2Te_3 and polycrystalline Te.

3.6 Summary

In summary, using high-throughput physical vapour deposition and characterization techniques, we demonstrate that amorphous Bi:Te can serve as a compositionally tunable material platform for UV/visible plasmonics. The plasmonic character of the chalcogenide is illustrated via the fabrication of subwavelength period nano-grating metasurfaces, which present a highly anisotropic optical response: under TM-polarized illumination (incident electric field perpendicular to the grating lines) plasmonic absorption resonances are manifested as period-dependent variations in the perceived colour of the nanostructured domains, while for TE-polarized light the metasurface domains are almost indistinguishable from unstructured Bi:Te.

Moreover, we study the phase change properties of this alloy revealing that the change on the optical properties with the phase transition between the amorphous and the crystalline state is a modest variation overall with an average change in F_2 of 11 % and in F_3 of 20 % at 1310 nm and 26 % at 1550 nm. However, a change of 55% in F_2 is observed for compositions around Te content of 76% (Bi 24%) suggesting that Bi:Te material system presents phase change properties for these compositions, but in a weaker form compared to other well-known phase change materials like $Ge_2Sb_2Te_5$ and GeTe [122]. Furthermore, these phase change properties might be associated with Te segregation after the annealing that results in the formation of a material with two mixed phases, namely polycrystalline Bi_2Te_3 and polycrystalline Te.

In conclusion, we have shown that Bi:Te alloy is a compositional adaptable material base for plasmonics and nanophotonics with compositionally controlled optical properties. While presenting a plasmonic response in an as-deposited amorphous thin film that holds a significant advantage over bulk and solution-processed crystalline chalcogenides (and various other “alternative plasmonic” media) in terms of device production process compatibility and scalability. Alongside established credentials as a thermoelectric medium [128], and the possibility of non-volatile electrically/optically-induced phase-change switching of properties [122, 123], it presents intriguing possibilities for the control of photons and electrons in thin film thermo/opto-electronics, including for aesthetic purposes (e.g. harnessing plasmonic “structural colour” in building-integrated thermoelectric devices).

Chapter 4

Epsilon-Near-Zero Properties of Sb_2Te_3

4.1 Introduction

In this chapter, we focus on the epsilon-near-zero (ENZ) properties of the Sb:Te binary alloy firstly introduced in Chapter 2, since this material presents a UV-visible ENZ point with relatively low loss for some specific compositions.

At the beginning of the chapter a general overview of ENZ phenomena in metamaterials is provided; then, we consider the case of an array of subwavelength apertures in a metal film filled with a low-epsilon medium at optical frequencies (Sb_2Te_3) where an increase in transmission over a broad range of plasmonic frequencies is observed, and found to be enabled by "laminar" flow of energy through the chalcogenide inclusions. For a low-epsilon medium with causality-bound dispersion of the real and imaginary parts of relative permittivity, a peak in transmission emerges at the wavelength of unity refractive index (i.e. $n = 1$) as losses decrease, while counterintuitively the absorption of the composite structure increases. After presenting the simulation of nano-slots metasurfaces, we describe the corresponding experimental realization by using a slightly different metasurface design, namely we fabricated an array of elliptical nano-slits instead of nano-slots.

4.2 Epsilon-Near-Zero Phenomena in Metamaterials

Modern metamaterials research field started with the study of negative refractive index [75] based on the theoretical work of V. G. Veselago [129]. Metamaterials paradigm opened up the way to explore optical phenomena in unusual refractive index condition and in this context, one of the most exciting research topic in metamaterials field was developed after the study of field dynamics in structures with near-zero constitutive parameters [130, 131]. These can be classified as epsilon-near-zero (ENZ) materials when relative permittivity (ε) is near zero ($\varepsilon \approx 0$), mu-near-zero (MNZ) when relative permeability (μ) is near zero ($\mu \approx 0$) and finally epsilon-and-mu-near-zero (EMNZ) when both ε and μ are near zero [132]. This class of

materials shows unique features enabling exceptional light-matter interactions and investigation of qualitatively different wave dynamics [132]. One of the most intriguing aspect of near-zero constitutive parameters is the relaxation of the link between the frequency and wavelength [133]. In general, the scattering response of a medium is determined by the spatial (wavelength) and temporal (frequency) features; however, by considering time-harmonic source-free Maxwell equations for the electric and magnetic field is possible to demonstrate the decoupling of electricity and magnetism [131, 132] with the consequential removal of the link between the frequency and wavelength. Moreover, this effect is associated with a "stretching" of the wavelength [132] since the phase velocity (*v*) is defined as:

$$v = f\lambda = \frac{c}{\sqrt{\varepsilon_r}} \tag{4.1}$$

Where *f* is the frequency, λ is the wavelength, ε_r is the relative permittivity and *c* is the speed of light in vacuum. Hence, as ε and/or μ approach zero, the phase velocity will became very high in value resulting in long wavelength at high frequency [133]. This feature has both an important fundamental interest and a profound technological impact since it enables the observation of unusual phenomena and the design of unconventional devices [132].

Recently Engheta *et al.* showed that the transmission of sub-wavelength waveguide channels can be enhanced by filling them with low-loss epsilon-near-zero (ENZ) media, whereby these channels can act as "wires" for light [134], in particular in interconnect and "metatronic" applications [135]. Moreover, a range of exciting phenomena affecting the quantum properties of emitters in ENZ materials has been predicted, including control of relaxation rate and cooperative emission [132, 136]. One of the most exciting wave property offered by ENZ metamaterials is the phenomenon of supercoupling that consists on the tunnelling of electromagnetic waves through a very narrow channel filled with an ENZ material [134]. The geometry that was first used to study this phenomenon is reported in Figure 4.1 and it consists of two 2D waveguides connected by a very narrow channel. It was demonstrated theoretically [134] and experimentally [137] that the electromagnetic wave is fully transmitted via the ENZ channel regardless the geometry of the structure [133].

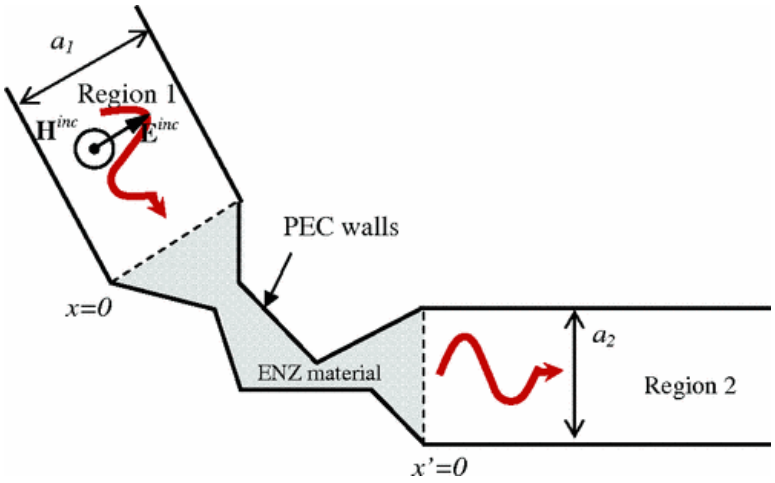

Figure 4.1: Geometry of a generic 2D waveguide structure with an ENZ material section. The waveguide walls in regions 1 and 2 are parallel to the x and x' directions, respectively. The interfaces of the ENZ material channel are planar and normal to the waveguide walls [134].

Although some proof-of principle experiments in the microwave parts of the spectrum have confirmed predictions of the unusual properties of ENZ media [137, 138], studies of the properties of ENZ materials in the optical part of the spectrum are hindered by their intrinsic losses [16, 132]. Hence, the research of new materials with near-zero parameters is currently crucial for the implementation of technological devices with unconventional properties. Several approaches have been explored in order to obtain structures exhibiting near-zero parameters (Figure 4.2), the first one is the use of continuous media with ENZ points at a certain spectral range. This class of materials has a permittivity that usually follow Drude or Drude-Lorentz dispersion models and the ENZ behaviour is observed at their plasma frequency since the real part of the permittivity goes to zero at this frequency [139]. Polaritonic materials such as silicon carbide show ENZ properties at mid-IR, doped semiconductors like transparent conducting oxides (for example aluminium-doped zinc oxide and indium tin oxide) exhibit this behaviour at near-IR, close to telecom wavelengths (1550 nm) and topological insulators such as $Bi_{0.5}Sb_{0.5}Te_{1.8}Se_{1.2}$ present an ENZ cross-over point at UV spectral range [33, 132]. The second method is based on metamaterial approach, namely exploit metamaterials mimicking the properties of continuous media with near zero parameters. For instance, a hollow rectangular waveguide around the cut-off frequency of its TE_{10} mode can be viewed as a material with effective zero permittivity and this concept was used to firstly demonstrate the supercoupling effect [137]. This approach was investigated even further showing for example the realization of plasmonic effects without negative dielectrics [140] and it was used also for structures operating at optical frequencies [141]. Alternative metamaterial methods have been explored such as wire-media that can be described by Drude model and by using stacked layers of materials with

opposite permittivity is possible to obtain an effective permittivity near to zero [132, 142]. The third approach can be viewed as a combination of the previous two methods, since it is based on using dielectric particles immersed in a ENZ continuous material to modify the medium's effective permeability while keeping constant its permittivity [138]. This is called "photonic doping" and could have a big potential in the realization of reconfigurable and flexible photonics [132].

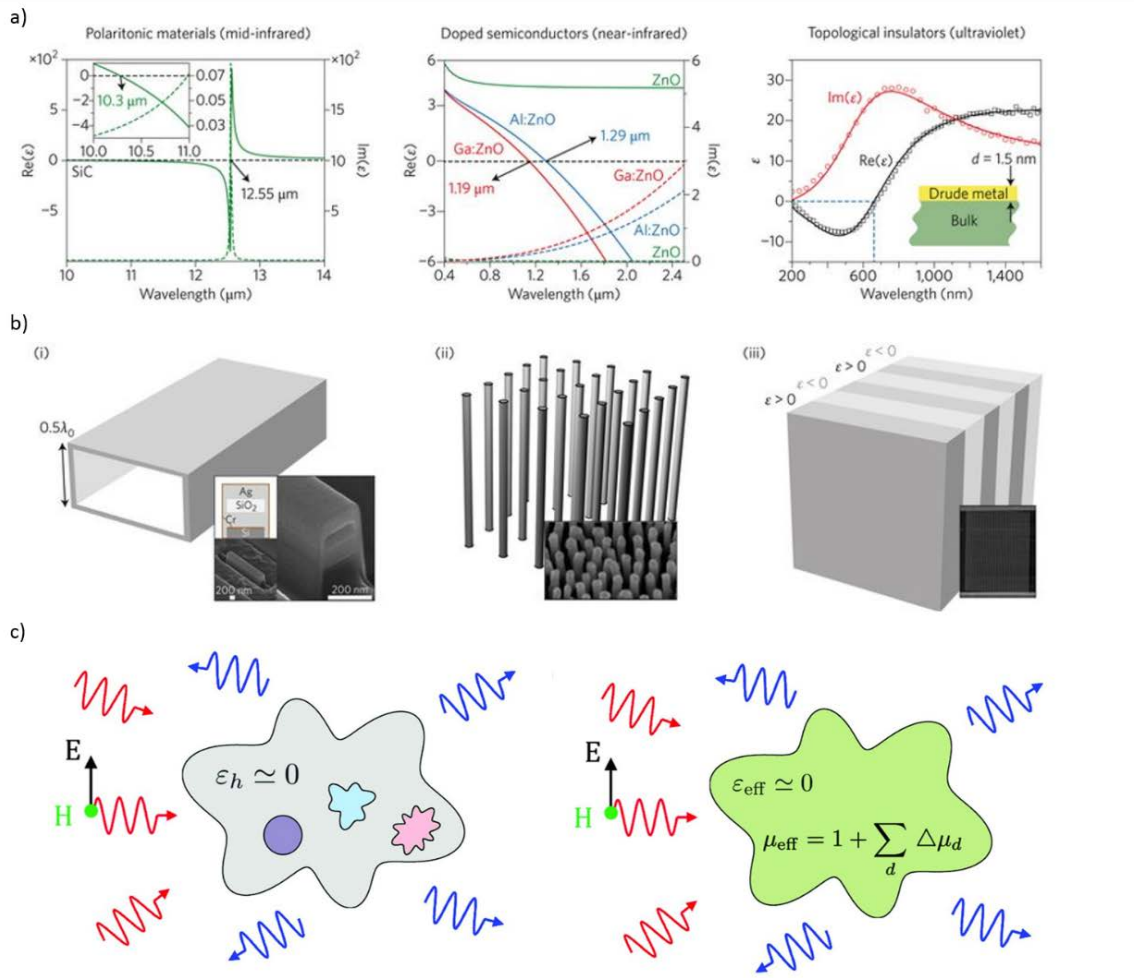

Figure 4.2: Different approaches explored to achieve structures exhibiting near-zero parameters. a) Continuous media including polaritonic materials such as SiC at mid-IR frequencies (left), doped semiconductors such as transparent conducting oxides (TCOs) at near-IR frequencies (centre) and topological insulators such as $Bi_{1.5}Sb_{0.5}Te_{1.8}Se_{1.2}$ (BSTS) at UV frequencies (right). b) Synthetic implementations including waveguides at cut-off (i), wire media (ii), multilayered structures (iii) (adapted from [132]). c) Photonic doping approach [138].

4.3 Nano-hole Arrays Filled with Chalcogenide Low-epsilon Media

Nano-structuring can provide an astonishing level of control over the optical properties of a thin metal film: depending on the dimensions and geometric design, one may achieve

extraordinarily strong transmission through optically thick films [143-145] or extraordinarily low transmission through optically thin (partially transparent) films [146-149]. Moreover, chiral nano-structuring in metamaterials can lead to optical activity [150, 151] and asymmetric transmission of polarized light in opposing directions [152, 153]. Metamaterial structuring of dielectric films can lead to the appearance of magnetic optical response [38], enable the creation of non-reflective "Huygens surfaces" [154], provide for the excitation of toroidal [155] and anapole [156] electromagnetic modes. Materials presenting an electromagnetic response that lies between those of metals and dielectrics also offer very interesting opportunities. In semiconductors inter- and intra-band transitions can lead to strong dispersion of optical properties with spectral domains of low and high loss, negative and positive real part of permittivity, plasmonic and "epsilon-near-zero" (ENZ) behaviours and, in some cases, distinctive topologically-protected surface optical properties can be observed [34]. As already described in Chapter 2, good examples of such highly dispersive materials are chalcogenide semiconductors wherein dielectric responses of different types can be seen across the visible and near-IR parts of the spectrum and optical properties can be "engineered" by controlling alloy composition [34, 46].

As already mentioned in the introduction, ENZ phenomena have been investigated mainly in the microwave parts of the electromagnetic spectrum, while the optical range is largely unexplored due to the intrinsic high losses of materials at optical wavelengths. Indeed, while values of the real part of relative permittivity ε_1 equal to zero are not uncommon (e.g. in silicon at 294 nm [20], chromium at 1.088 μm [21]), corresponding values of the imaginary part of permittivity ε_2 are typically high. So the question is whether there are circumstances, nanostructured geometries for example, in which materials with sufficiently low values of epsilon can manifest unusual behaviours at optical frequencies. In particular, a lossy air-ENZ interface was studied theoretically in ref. [157] showing that material loss can actually play a positive role which collimates the incident light beam and enhances the transmission and propagation inside the ENZ medium. Following that work, here we consider the transmission of electromagnetic radiation through subwavelength apertures in a plasmonic metal film - examining whether filling the gaps with an optical-frequency low-epsilon medium enhances their transmission at the epsilon-*nearest*-zero wavelength and how the losses inevitably present in a real low-epsilon medium affect the optical properties of such a composite film.

In what follows, beginning with the example of a real chalcogenide low-epsilon semiconductor - antimony telluride (Sb_2Te_3), we demonstrate that filling the apertures of a nanostructured metal film with such a material leads to more complex behaviour than simply an enhancement of transmission. Indeed, in some cases the opposite can occur, with

transmission suppressed at wavelengths where epsilon is near to zero while being enhanced at others. The complex changes in the composite's spectral response depend strongly on the interplay between the dispersion of the optical properties of the plasmonic nanostructure and the ENZ medium.

4.4 Simulation of Nano-Slot Metasurfaces

Antimony telluride is a binary chalcogenide alloy; a narrow-gap semiconductor known for its phase-change [158] and thermoelectric properties [159, 160], and lately attracting interest as a 3D topological insulator [115, 161]. In the UV/visible spectral range its amorphous form exhibits a plasmonic response – a negative value of the real part ε_1 of relative permittivity, as shown by the ellipsometric data presented in Figure 4.3a, which is obtained for a 30 nm film of Sb_2Te_3 prepared by physical vapour deposition on a silicon substrate as described in Chapter 2. The composition, i.e. the at.% ratio of 2:3, is confirmed by energy dispersive x-ray spectroscopy.

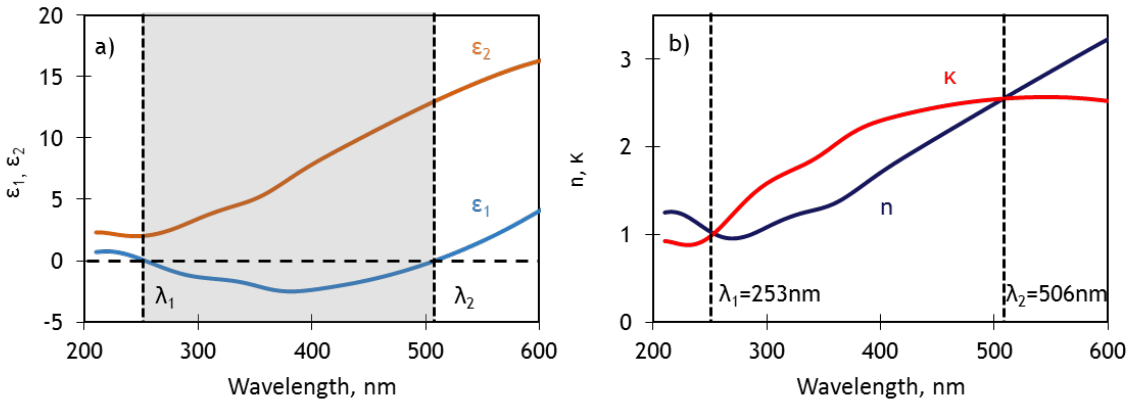

Figure 4.3: UV/visible plasmonic and ENZ properties of amorphous antimony telluride. a) Real (ε_1) and imaginary (ε_2) parts of complex relative permittivity and b) corresponding complex refractive index (n, κ) of as-deposited amorphous Sb_2Te_3 measured by variable-angle spectroscopic ellipsometry.

Of the two $\varepsilon_1 = 0$ crossing points, at wavelengths $\lambda_1 = 253$ nm and $\lambda_2 = 506$ nm, the former is of greater interest because losses (i.e. the value of ε_2) are much lower in the near-UV range. Moreover, near to this spectral point the real part of the chalcogenide's refractive index (Figure 4.3b) is close to 1. To study how optical transmission through nanoscale apertures is affected by this ENZ material, we analysed the optical properties of metasurfaces comprising arrays of parallel, deeply-subwavelength (10 nm width) slots through a 15 nm thick free-standing aluminium film, filled with amorphous Sb_2Te_3 (Figure 4.4), and for reference studies identical metasurface with empty slots. Full-wave electromagnetic simulations of nano-slot

metamaterial structures were performed using the finite element method in COMSOL Multiphysics. Structures are assumed to be free-standing in air and of infinite extent (by virtue of periodic boundary conditions) in the *xy* plane. In the first instance, the model employs ellipsometrically measured material parameters for real Sb_2Te_3 as presented in Figure 4.3 and parameters for aluminium from ref. [109] and it assumes normally incident, narrow-band, coherent illumination polarized in the *x*-direction (perpendicular to the nano-slots).

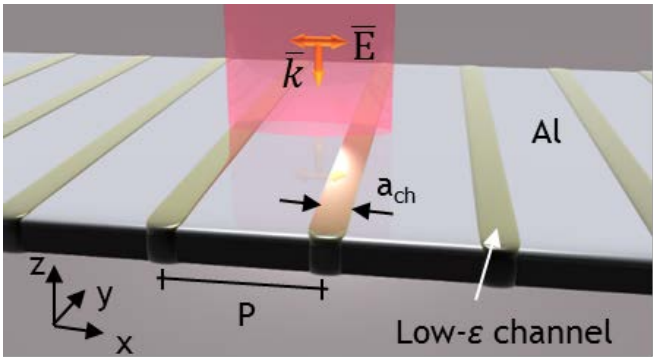

Figure 4.4: Aluminium nano-slot metasurface modelling. Schematic illustration of the numerically simulated metasurface, which comprises a periodic array of linear slots (width w << illumination wavelength λ, centre-to-centre spacing P < λ) in a semi-transparent aluminium film (thickness t = 15 nm) that may either be empty or, as show, filled with amorphous Sb_2Te_3. Incident light is polarized perpendicular to the slots.

4.5 Not-So-Extraordinary Transmission: Simulation

It is found (Figure 4.5) that filling the slots with Sb_2Te_3 brings about a broadband increase in transmission over spectral range extending from below λ_1 almost up to λ_2, and a corresponding decrease in reflectivity, even to longer wavelengths. The increase in transmission at the low-loss UV $\varepsilon_1 = 0$ point λ_1 is comparatively modest (an absolute change of <5%) and in fact represents a shallow dip in the broader trend of the Al/ Sb_2Te_3 composite film's transmission spectrum, which is matched by a shallow peak in reflection; larger increases in transmission are seen at longer wavelengths within antimony telluride's plasmonic ($\varepsilon_1 < 0$) band between λ_1 and λ_2.

The cross-sectional maps of electric field strength and powerflow shown in Figure 4.6 illustrate differences between the metasurface optical response for empty and Sb_2Te_3-filled slots. In an array of empty nano-slots, with no chalcogenide material present, "whirlpools" of optical energy are formed around the nano-slots at short, near-UV wavelengths, within which powerflow through the open aperture is in the backward direction relative to incident light. Such whirlpools are characteristic of resonant plasmonic nanostructures, having initially

been observed around plasmonic nanoparticles [162]. With increasing wavelength, at the λ^* = 380 nm plasmonic resonance losses and radiation backflow balance the inflow of energy, causing the transmission of the perforated Al film to fall to zero at this wavelength [146]. At longer wavelengths still, powerflow whirlpools are re-established, but with rotation in the opposite direction as to the short wavelength side of the λ^* resonance wavelength. The same inversion of the energy circulation direction is seen as the excitation wavelength is tuned across the plasmonic resonance of a metal nanoparticle [162].

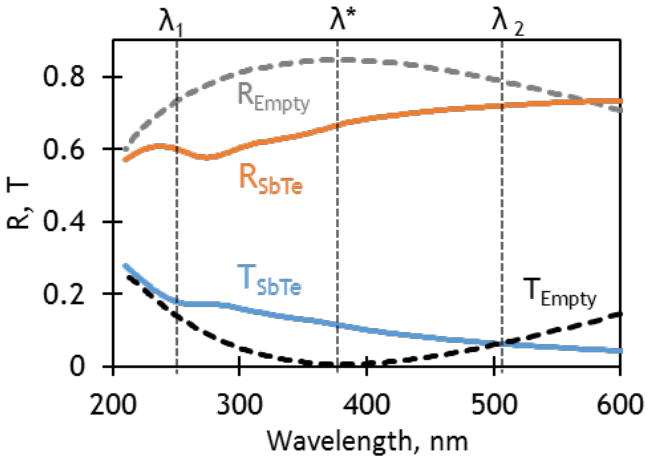

Figure 4.5: Spectral dispersion of reflection and transmission for a metasurface, of period P = 100 nm and w = 10 nm, with empty and Sb_2Te_3-filled slots (denoted by dashed and solid lines respectively).

When the slots are filled with Sb_2Te_3, we observe "laminar" flow of light through the film at all wavelengths, with minimal local field enhancement; no powerflow whirlpools are seen around the slots. (Here we adopt hydrodynamic terminology, where "laminar flow" describes a regime characterized by high momentum diffusion and low momentum convection with no turbulence. i.e. no whirlpools.) Light propagates from one side of the slot array to the other with the Sb_2Te_3-filled slots acting as conduits for light in which the magnitude of epsilon $|\varepsilon| = \sqrt{(\varepsilon_1^2 + \epsilon_2^2)}$ is low, i.e. nearer to zero than in aluminium. Transmission gradually decreases with increasing wavelength as losses in Sb_2Te_3 increase.

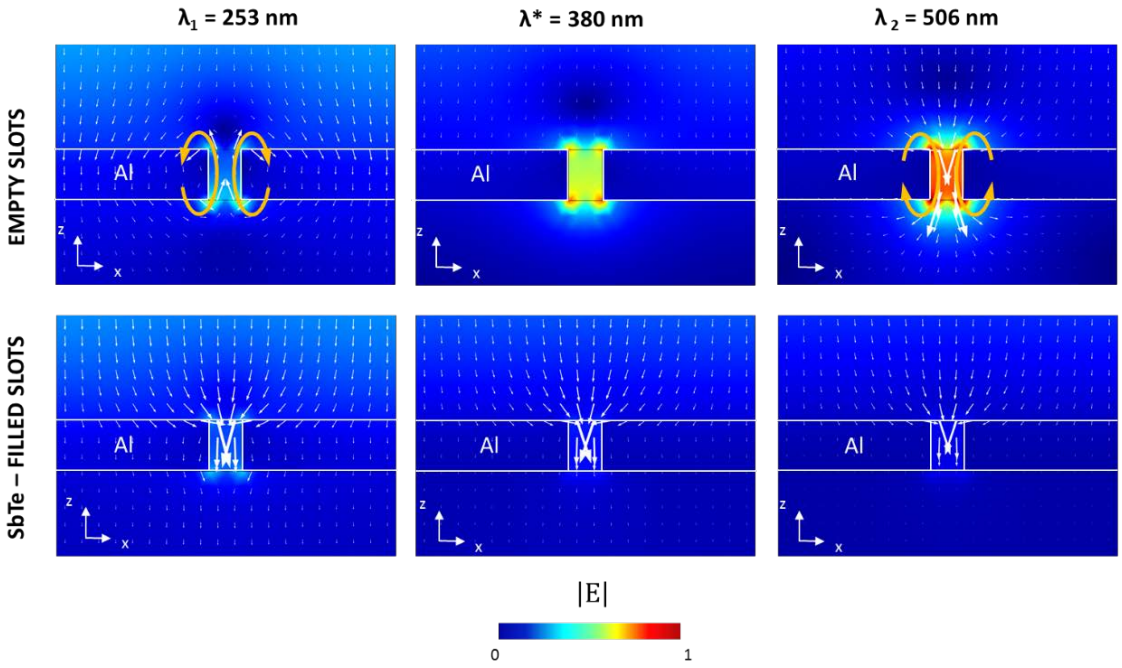

Figure 4.6: Comparison of electric field distribution between empty and Sb_2Te_3-filled slots. Spatial distribution of electric field in the xz plane, overlaid with arrows showing net (time-averaged) powerflow, for metasurfaces with empty slots and with Sb_2Te_3-filled (upper and lower rows respectively) at Sb_2Te_3's two ε_1 zero-crossing wavelengths, λ_1 = 253 (left) and λ_2 = 506 nm (right), and at λ^* = 380 nm (centre).

ENZ related phenomena like supercoupling are usually not influenced by the geometry of the structure (see paragraph 4.2); hence, we investigate the geometrical robustness of the optical properties of these metasurfaces by varying geometrical parameters. In particular, we vary the ENZ channel width while keeping the period constant and vice versa. Furthermore, we consider also different channel shapes.

The absolute level of transmission and reflection increases with decreasing the ENZ channel width, a_{ch}, when the period of the metasurface structure (centre-to-centre spacing of slits) is fixed (Figure 4.7a); instead absorption decreases (Figure 4.7b). When the period is varied and the channel width is fixed, transmission spectra are almost unchanged while reflection is increasing as the period is increased and absorption shows an opposite trend (Figure 4.7c, d). However, in accordance with expectation for an ENZ tunnelling effect [163], and in stark contrast to conventional metamaterial resonant phenomena, the spectral position of the transmission peak for these metasurfaces do not depend on either the channel width or periodic separation of the ENZ rods.

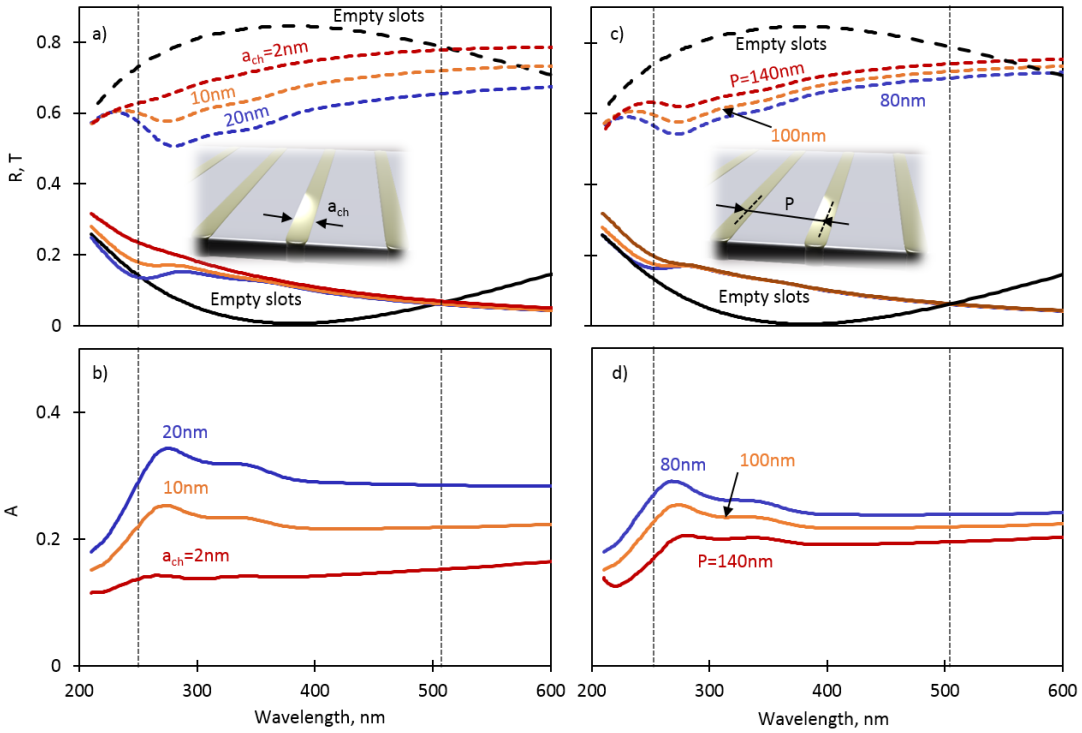

Figure 4.7: Optical spectra through aluminium nano-slot metasurfaces across geometrical parameters. Spectral dispersion of metasurface transmission, reflection (a, b) and absorption (c, d) for a selection of ENZ channel width at fixed period P = 100 nm (a, c), and for a selection of periodic spacing at fixed channel width ach = 10 nm (b, d). The black lines (dashed and continuous) in each case are spectra for empty nano-slot metasurfaces.

The independence of the enhanced transmission effect from variations in the geometry of the ENZ channels is further demonstrated by considering different shapes for the nano-gratings, where reflection and transmission spectra remain almost unchanged as shown in Figure 4.8.

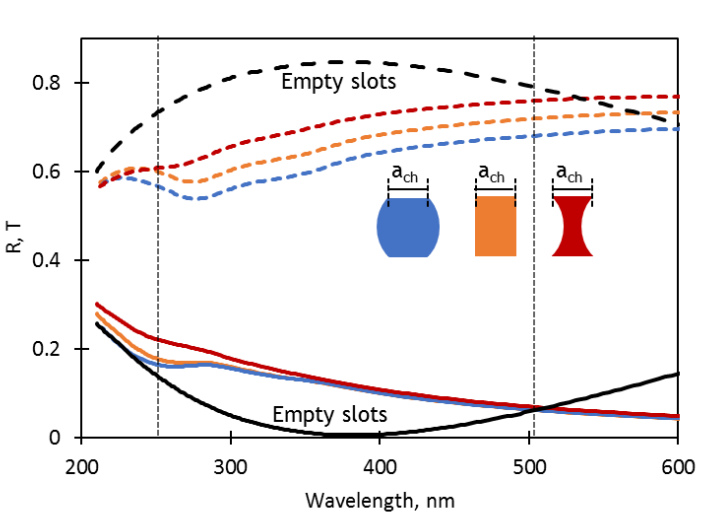

Figure 4.8: Optical spectra through aluminium nano-slot metasurfaces across different channel shapes.

Furthermore, we study how transmission of ENZ-filled nano-slots metasurfaces is enhanced and reflection reduced compared to empty nano-slots metasurfaces across all the plasmonic ENZ range (253 nm < λ < 506 nm) of amorphous Sb_2Te_3 for angles of incidence up to 40°. This is shown in Figure 4.9 where the reflection and transmission differences between metasurfaces with empty nano-slots and nano-slots filled with Sb_2Te_3 are plotted as a function of wavelength.

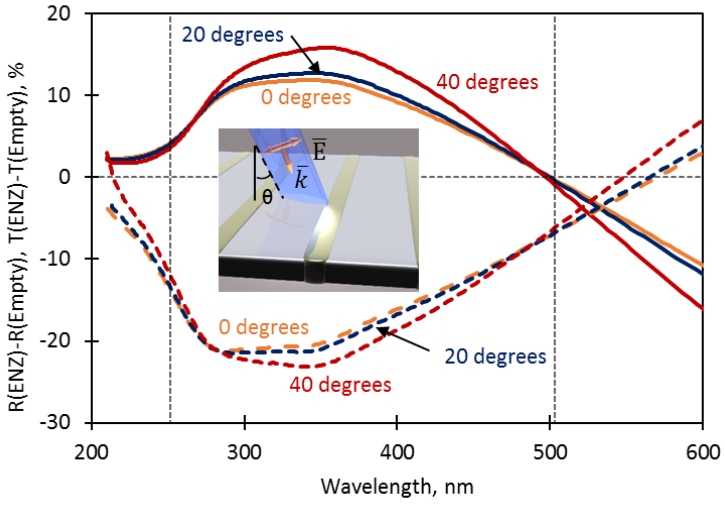

Figure 4.9: ENZ channel acceptance angle. Spectral dispersion obtained by the difference between reflection spectra (dashed lines) from metasurfaces with empty nano-slots and nano-slots filled with ENZ material different angle of incidence (θ) together with dispersion calculated by the difference between transmission spectra (continuous lines) from metasurfaces with empty nano-slots and nano-slots filled with ENZ material across different angle of incidence (θ). The inset shows a schematic illustration of the simulated metasurface for a certain angle of incidence θ.

After the study of ENZ-metasurfaces by varying the geometrical parameters of the nanostructure, we analyse what could conceivably be achieved with low-loss ENZ materials and to understand the role of losses in the transmission changes induced by filling the nano-slots with chalcogenide, it is instructive to consider the effects of reducing the value of ε_2 at the near-UV ε_1 zero-crossing wavelength λ_1. To this end we employ dispersions of ε_1 and ε_2 for a hypothetical chalcogenide material, derived from those of real Sb_2Te_3 by reduction of optical losses (ε_2) in a manner consistent with Kramers-Kronig relations. (Indeed, any departure from the Kramers-Kronig relations between the real and imaginary parts of permittivity would lead to an unphysical description of the material and related wave phenomena, compromising the fundamental causality of electromagnetism [164]). The measured spectral dispersion of antimony telluride's relative permittivity is reproduced very well by a single Lorentzian oscillator absorption model (described in section 2.4) (dashed "fit"

lines in Figure 4.10), with an oscillator frequency ω_0 of 3.2× 10^{15} Hz, a static dielectric constant ε_s of 23, a high-frequency dielectric constant ε_∞ of 3.1, and a damping factor of the oscillator Γ of 4.0 × 10^{15} Hz. These parameters are subsequently adjusted to produce modified dispersion curves (Figure 4.10) for hypothetical low-loss media in which ε_2 is reduced by a given factor at λ_1 while maintaining $\varepsilon_1 = 0$ at both of the (real Sb_2Te_3) zero-crossing wavelengths λ_1 and λ_2.

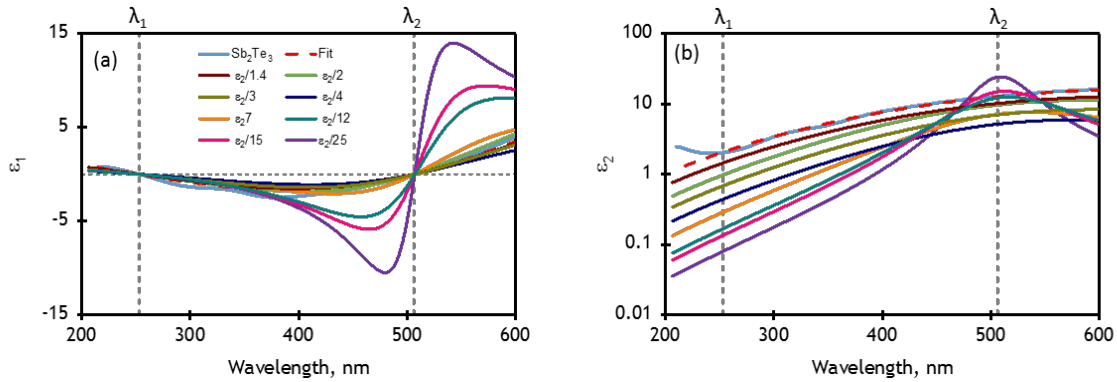

Figure 4.10: Reduction of losses in ENZ channels. a, b) Lorentzian oscillator fitting to the real and imaginary parts of measured relative permittivity for Sb_2Te_3 (as presented in Figure 4.3a); and Kramers-Kronig-compliant spectral dispersion of complex permittivity for hypothetical media having the same value of ε_1 in the UV range but lower losses: ε_2 reduced by factors of 1.4, 2, 3, 4, 7, 12, 15 and 25 at the $\varepsilon_1 = 0$ wavelength λ_1 = 253 nm (as labelled).

Figure 4.11 shows the dispersion of metasurface optical properties when the slots are filled with hypothetical materials having losses at λ_1 that are up to 25 times smaller than in vapour-deposited Sb_2Te_3. Associated oscillator model parameters values are presented in Table 4.1. Intriguingly, the reduction of ε_2 at the $\varepsilon_1 = 0$ wavelength λ_1 actually decreases transmission at this point, rather than increasing it as one might anticipate from analytical studies of ideal ENZ media (i.e. based upon the idea that electromagnetic waves may traverse sub-wavelength waveguide channels unimpeded when they are loaded with a low-loss ENZ medium [134, 137]). Indeed, the loss reduction results in the emergence of a pronounced peak in transmission (dip in reflection) at longer wavelengths where moreover, up to a point, metasurface absorption actually increases as losses in the chalcogenide inclusions decrease - the level of absorption saturates with around a factor of seven reduction in ε_2 while absorption linewidth continues to decrease as ε_2 decreases further.

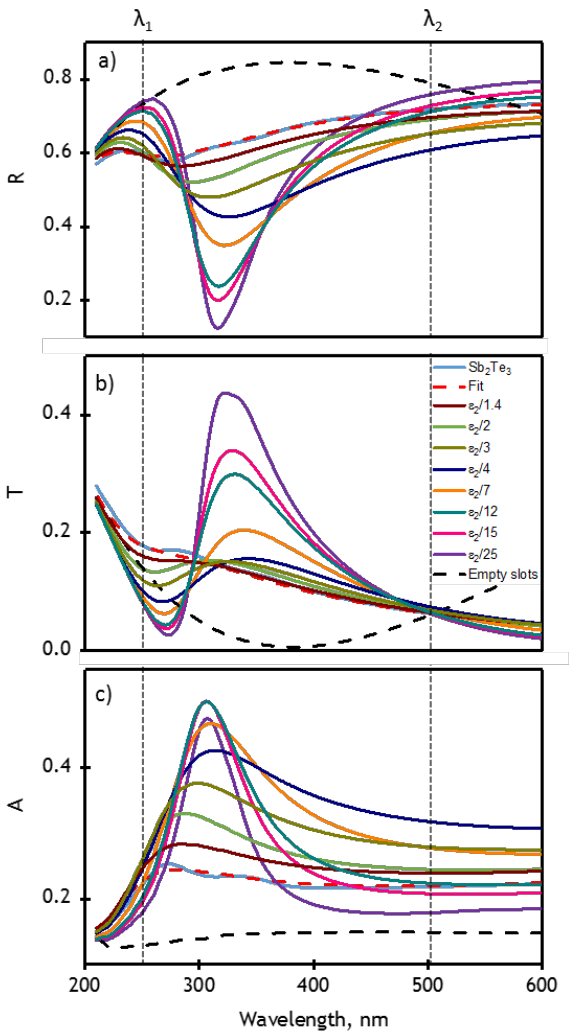

Figure 4.11: Reduction of losses in low-epsilon composite metasurfaces. Spectral dispersion of a) reflection, b) transmission, and c) absorption for the metasurface of Figure 4.4 with empty slots (dashed black lines), Sb_2Te_3-filled slots (light-blue lines), and slots filled with hypothetical reduced-loss variants of the chalcogenide with permittivites as presented in Figure 4.10 (ε_2 reduction factors as labelled).

These behaviours are consistent with the recent analytical finding [28] that increased losses can increase electromagnetic wave transmission at unstructured, singular air/ENZ interfaces, by facilitating better impedance matching. In the present case, metasurface transmission is determined by the balance among interfacial transmission and reflection coefficients for and propagation losses within the low-epsilon medium, against the backdrop of the nano-structurally engineered response. The spectral position of the emergent transmission resonance tends towards the wavelength at which the magnitude of refractive index $|N| = \sqrt{(n^2 + \kappa^2)}$ is equal to one, i.e. is matched to the incident medium (vacuum), as losses decrease [141] (see Figure 4.12a). The spectral position of the dip in transmission (peak in reflection) near to λ_1 is also a function of refractive index - tracking the wavelength at which

$|N|$ is minimized, which in turn is a function of the loss reduction factor (as shown in Figure 4.12b).

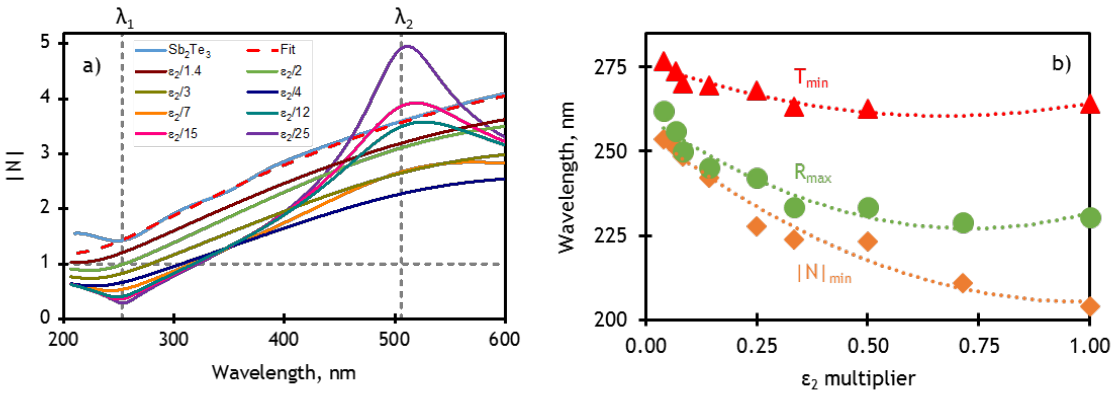

Figure 4.12: Refractive index of antimony telluride and reduced-loss variants. a) Spectral dispersion of the magnitude of complex refractive index $N = n + i\kappa$, including traces derived from the experimental data for synthesized Sb_2Te_3 (Figure 4.3b), the Lorentzian fitting to this data and the hypothetical reduced-loss variants (Figure 4.10a and b). b) Dependence upon the loss (ε_2) reduction factor of the wavelengths at which magnitude of refractive index is minimized and at which reflection and transmission are locally maximized and minimized respectively in the vicinity of λ_1.

This picture is further confirmed by looking at the cross-sectional maps of electric field strength and powerflow extracted for nano-slots filled with hypothetical reduced loss materials (as it was done before for the case of empty and Sb_2Te_3-filled slots). In fact, the reduction of transmission observed when ε_2 is decreased by 7 and 25 times (see Figure 4.11b) matched with the presence of whirlpools of optical energy observed around the nano-slots at short, near-UV wavelengths, with powerflow oriented in the backward direction relative to incident light (Figure 4.13). Instead, at longer wavelengths, these powerflow whirlpools disappear and a laminar flow regime of light is established through the film for all the three hypothetical materials (Figure 4.13). This fits well with the observed increase of transmission visible in Figure 4.11b around 300 nm. Since at these wavelengths losses (ε_2) are lower, the powerflow through the nano-apertures is higher (longer arrows in Figure 4.13); then at even longer wavelengths (around 500 nm) ε_2 increases, hence both powerflow and transmission are reduced.

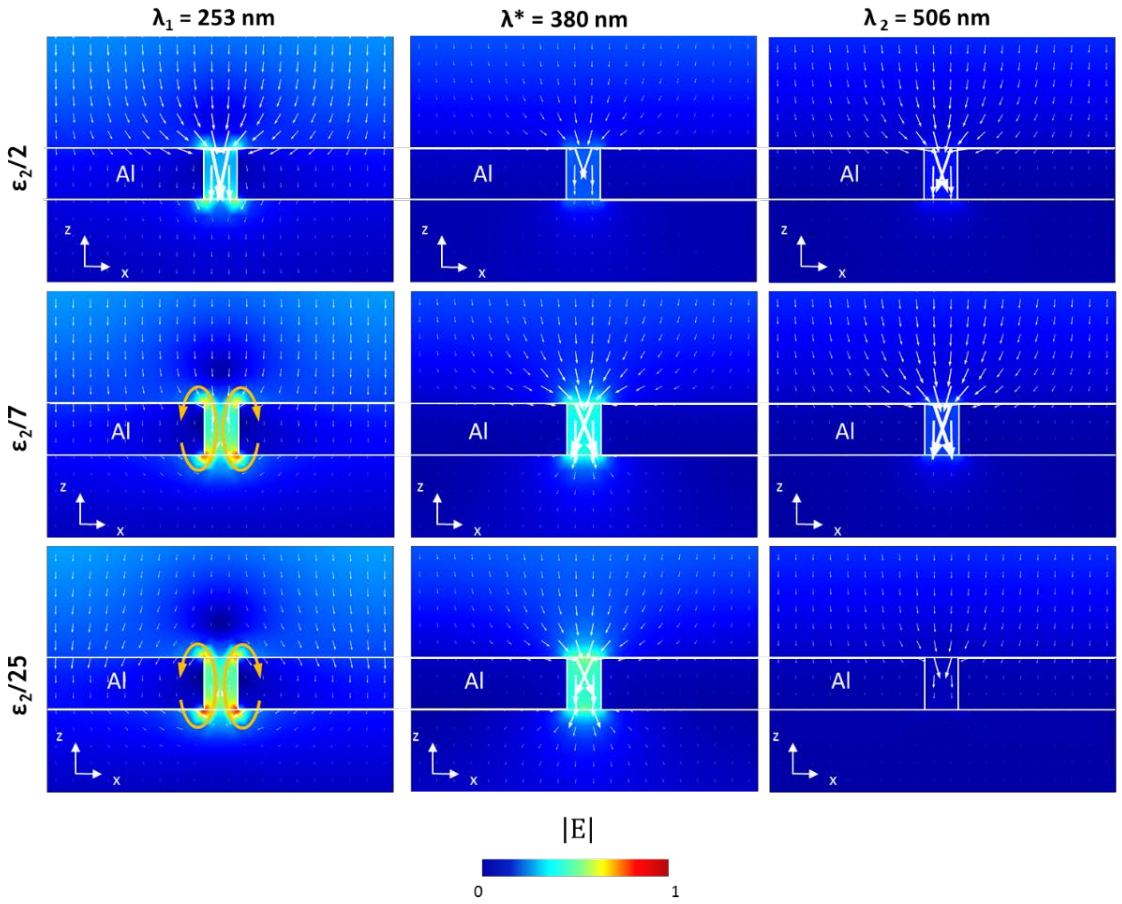

Figure 4.13: Comparison of electric field distribution for different values of ε_2. Spatial distribution of electric field in the xz plane, overlaid with arrows showing net (time-averaged) powerflow, for metasurfaces with slots filled with hypothetical media having ε_2 reduced by factors of 2, 8 and 25 at the corresponding $\varepsilon_1 = 0$ two ε_1 zero-crossing wavelengths, λ_1 = 253 (left) and λ_2 = 506 nm (right), and at λ^* = 380 nm (centre). For λ^* = 380 nm the length of arrows is reduced for clarity by a factor of 2 compared to the other two wavelengths.

Table 4.1: Lorentzian oscillator model parameters values for the fitting to ellipsometric data for the relative permittivity of amorphous Sb_2Te_3 and the modified permittivity datasets shown in Figure 4.10a and b.

	ε_∞	ε_s	ω_0 (Hz)	Γ (Hz)
Fit to measured Sb_2Te_3 parameters	3.1	23	3.19×10^{15}	4.03×10^{15}
$\varepsilon_2/1.4$ @ λ_1	2.4	16.1	3.27×10^{15}	3.65×10^{15}
$\varepsilon_2/2$ @ λ_1	2	11.25	3.42×10^{15}	2.89×10^{15}
$\varepsilon_2/3$ @ λ_1	1.43	8	3.42×10^{15}	2.81×10^{15}
$\varepsilon_2/4$ @ λ_1	1	5.3	3.46×10^{15}	2.58×10^{15}
$\varepsilon_2/7$ @ λ_1	1	4.5	3.60×10^{15}	1.67×10^{15}
$\varepsilon_2/12$ @ λ_1	1	4.2	3.68×10^{15}	0.94×10^{15}
$\varepsilon_2/15$ @ λ_1	1	4.12	3.69×10^{15}	0.76×10^{14}
$\varepsilon_2/25$ @ λ_1	1	4	3.71×10^{15}	0.46×10^{15}

4.6 Not-So-Extraordinary Transmission: Experimental

After presenting the simulation of nano-slots metasurfaces, here we describe the corresponding experimental realization. A first attempt was done using the same design utilized for the simulation (Figure 4.4) and we observed a small change in the optical spectra between empty and filled nano-slots. This is probably due to manufacturing imperfections; in particular, it seems that the nano-slots were only partially filled with Sb_2Te_3. Hence, we decided to change the metasurface design from nano-slots to an array of elliptical nano-slits (Figure 4.14).

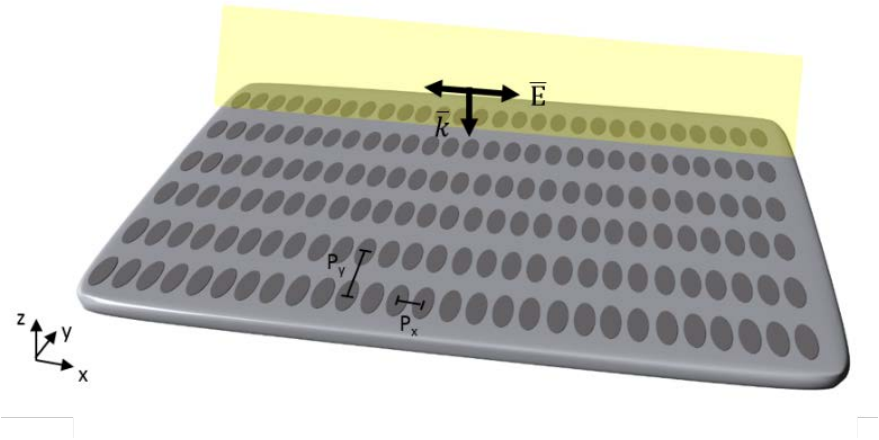

Figure 4.14: Schematic of the aluminium nano-slit array metasurface realized experimentally. Schematic illustration of the experimental metasurface, which comprises a periodic array of elliptical nano slits (with size and periods P_x and P_y << illumination wavelength) in a semi-transparent aluminium film (thickness t = 15 nm) that are empty after FIB milling of the Al layer and then filled with amorphous Sb_2Te_3 via physical vapour deposition.

The fabrication of aluminium nano-slit array metasurfaces requires multiple steps sketched in Figure 4.15, firstly we deposited an Al film on a sapphire substrate via resistive evaporation. A base pressure of 3×10^{-6} mbar was achieved prior to deposition and the thickness of the deposited film is controlled by a quartz crystal microbalance, an instrument that is sensitive to a mass variation per unit area as it measures the change in frequency of a quartz crystal resonator. The resonance is disturbed by the addition of a small mass due to film deposition at the surface of the acoustic resonator and so the thickness of the growing film can be measured. The thickness is also measured by a stylus profilometer and both techniques gives a thickness of 15 nm. Secondly, FIB milling is used to etch through the Al film several different patterns, namely arrays of nano-slits (Figure 4.17c) with different periods and size (controlled by changing the charge dosage of FIB). Thirdly, these nano-slit array metasurfaces were covered with a thin layer of Sb_2Te_3 using the HT-PVD system described in Chapter 2. In this way we expect to overfill the nano-slits fabricated via FIB covering also all the Al film. In order

to remove the residual of Sb_2Te_3 on top of Al, a dry-etching process was used. The etching rate was first calibrated by using a Sb_2Te_3 film as a reference sample; the calibration process consisted on the measurement of the Sb_2Te_3 film thickness by stylus profilometer, then dry etching for 1 minute and finally, again a measurement of the thickness of the film. After this calibration process, the nano-slit array metasurfaces overfilled with Sb_2Te_3 were gradually etched until all the Sb_2Te_3 on top of Al film was removed. In order to monitor that, after each etching step, transmission was measured with CRAIC microspectrophotometer.

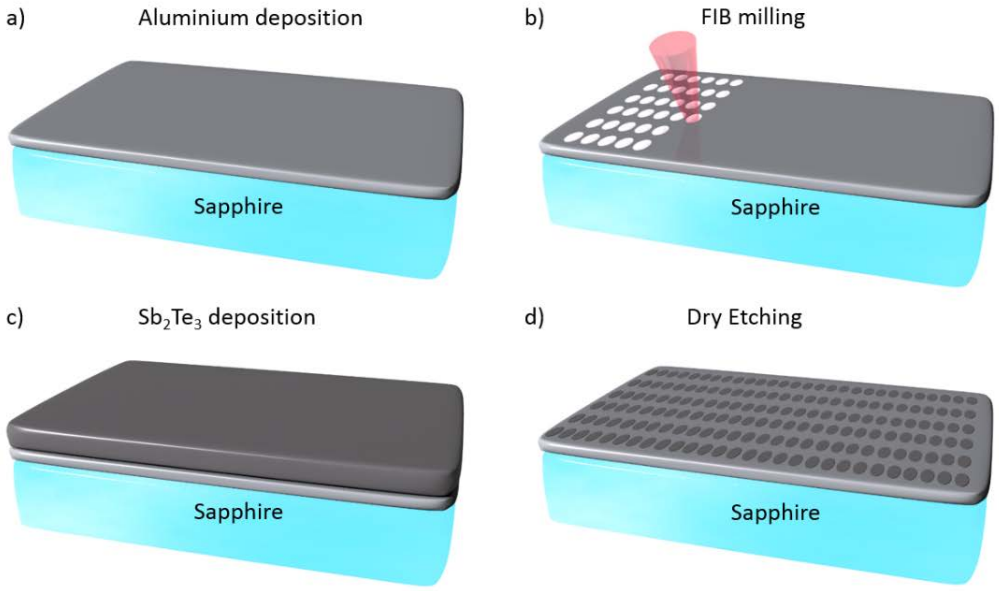

Figure 4.15: Fabrication steps for the realization of Sb_2Te_3 filled nano-slits metasurfaces: a) deposition of 15 nm of Al via resistive evaporation; b) FIB milling used to etch through the Al film an arrays of nano-slits; Sb_2Te_3 deposition via physical vapour deposition and d) Dry etching of Sb_2Te_3 residual on top of Al film.

The spectral dispersion of transmission was measured via a CRAIC microspectrophotometer covering the spectral range from 300 nm to 900 nm (Figure 4.16a) Transmission spectra reported in Figure 4.16 are measured with incident light polarized along *x*-direction. The transmission spectrum for empty nano-slit array metasurfaces with a nominal period of 100 nm along *x* and 150 nm along *y* shows a pronounced dip at around 420 nm, in this spectral range transmission is lower than the unstructured Al film. Then, by filling the nano-slits with Sb_2Te_3, transmission increases even if it is still lower than transmission of Al film. This phenomenon is observed at longer wavelength compared to the situation described in the previous section; however, we can observe the same counter-intuitive behaviour: the etching of nano-slits through a semi-transparent film reduces its transmission while it is usually expected that by removing some material, transmission should increase. Moreover,

by filling these nano-slits with a relatively lossy material which $\varepsilon_1 \approx 0$ (but negative), transmission is increased; instead, by filling the nano-slits with a dielectric ($\varepsilon_2 \approx 0$), transmission remains as low as for empty nano-slits. Thus, this peculiar behaviour can be understood through the optical energy whirlpools introduced in the previous section, namely these whirlpools with powerflow oriented in the backward direction relative to incident light are responsible of the reduction of transmission, while the presence of a material with negative ε_1 close to zero removes these whirlpools and established a laminar flow of energy that increases the overall transmission of the metasurface.

Here, we report only transmission spectra measured with incident light polarized along *x*-direction since transmission suppression due to empty nano-slit array metasurfaces and the further transmission recovering obtained with Sb_2Te_3 filling is not observed for incident light polarized along *y*.

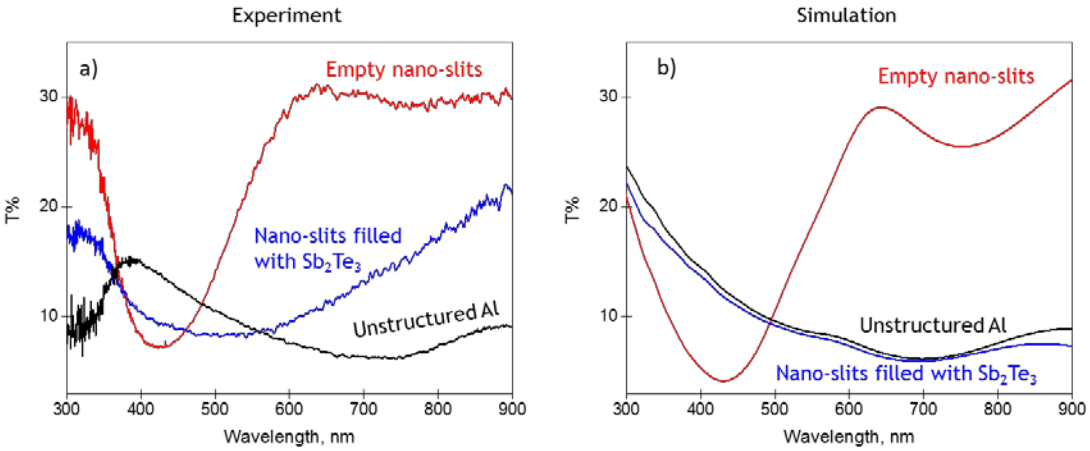

Figure 4.16: Spectral dispersion of transmission measured experimentally in a) and simulated via FDTD method (Lumerical) in b) for empty nano-slits metasurfaces (red curves), nano-slits metasurfaces filled with Sb_2Te_3 (blue curves) and unstructured Al film (black curves). Numerical simulations employ ellipsometrically measured material parameters for Sb_2Te_3 and Al. Incident light is polarized along x-direction both in experiment and simulation.

Transmission spectra obtained by numerical simulations show a good agreement with experimental spectra; the model assumes normally incident narrowband plane wave illumination in the –*z* direction of nano-slit array metasurface polarized along x direction and, by virtue of periodic boundary conditions, structures of infinite extent in the *xy* plane. Furthermore, simulations employ ellipsometrically measured material parameters for Sb_2Te_3 and Al and the substrate is modelled as a semi-infinite slab of sapphire (Al_2O_3) with optical constants from reference [165].The thickness of the Al layer used in the model is 15 nm, the period along *x* direction is 110 nm and along *y* is 150 nm, and the nano-slits width is 14 nm with a length of 110 nm.

The polarization-dependent behaviour of Sb_2Te_3 filled nano-slit array metasurfaces is well illustrated in Figure 4.17: optical microscope images in transmission mode reveal the presence of a reddish colour for *x* polarized light while for the other polarization the nanostructures show a similar colour of the surrounding Al film.

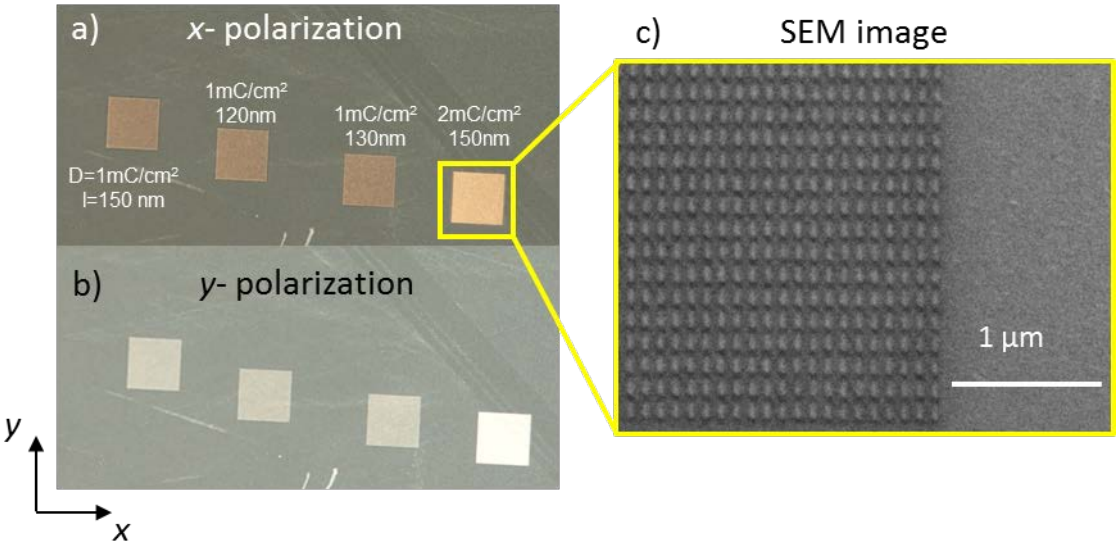

Figure 4.17: Optical and SEM images of the aluminium nano-slit array metasurfaces realized experimentally. Optical microscope images in transmission mode for Sb_2Te_3 filled nano-slit array metasurfaces with incident light polarized along x (a) and y (b) labelled according to the key experimental parameters (D is the area dose in mC/cm^2 and l is the line spacing in nm) used to control the size of the nanoholes. c) SEM picture of nano-slit array metasurface after FIB milling of aluminium film (empty nano-slits).

4.7 Summary

In summary, ENZ phenomena in metamaterials are one of the most intriguing topic of nanophotonics since ENZ behaviour has both an important fundamental interest and a profound technological impact that enables the observation of unusual phenomena and design of unconventional devices [132]. However, most of ENZ phenomena have been studied in the microwave range while the optical spectral range is still largely unexplored.

Here, we show, using experimentally measured material parameters for vapour deposited antimony telluride (Sb_2Te_3) in a series of numerical simulations, that optical frequency low-epsilon and near-unity index behaviours may be observed even in the presence of realistic losses. Sub-wavelength slots filled with the amorphous chalcogenide can serve as conduits for the “laminar flow” transmission of UV-visible light through a plasmonic metal screen: localized enhancement and powerflow “turbulence” in the optical near-field around open apertures in the screen are suppressed, producing a broadband enhancement of

transmission. However, transmission is not strongly enhanced at the low-loss epsilon-nearest-zero wavelength. Indeed a reduction of losses in the chalcogenide is found to suppress transmission at this point and can increase, rather than decrease, metasurface absorption depending on the magnitude of refractive index and the extent of index matching to the surroundings. Moreover, for a given cross-sectional area, the transmission of an ENZ channel (in a straight line through a given thickness of metal) is entirely independent of the channel shape and largely insensitive to angle of incidence up to 40°.

We also study these phenomena experimentally by realizing empty and filled with Sb_2Te_3 aluminium nano-slit array metasurfaces. The spectral range explored experimentally is at longer wavelengths compared to the simulations reported at the beginning of the chapter; however, we can observe the same counter-intuitive behaviour: the etching of nano-slits through a semi-transparent film reduces its transmission while it is usually expected that by removing some material, transmission should increase. Moreover, by filling these nano-slits with a relatively lossy material which $\varepsilon_1 \approx 0$ (but negative), transmission is increased; instead, by filling the nano-slits with a dielectric ($\varepsilon_2 \approx 0$), transmission remains as low as for empty nano-slits. Thus, this peculiar behaviour can be understood through the optical energy whirlpools introduced in the first part of the chapter, namely these whirlpools with powerflow oriented in the backward direction relative to incident light are responsible of the reduction of transmission, while the presence of a material with negative ε_1 close to zero removes these whirlpools and established a laminar flow of energy that increases the overall transmission of the metasurface.

Here, I described a first experimental attempt in the realization of these metasurfaces, however, the spectral range explored experimentally is at longer wavelengths compared to the simulations reported at the beginning of this chapter; thus, it will be interesting to study experimentally the optical properties in the same spectral range of the simulation (see section 6.2 “Future Work”).

Sb_2Te_3 is just one member of a broad chalcogenide family that includes numerous binary, ternary and quaternary sulphide, selenide and telluride alloys. With compositionally controllable optical properties, they offer a uniquely adaptable, CMOS-compatible material base for low-epsilon and low-index photonics, including applications in such areas as transmission enhancement, wavefront shaping and control of spontaneous emission.

Chapter 5

Reconfigurable Ultraviolet and High-Energy-Visible Dielectric Metamaterials

5.1 Introduction

In this chapter, we explore the optical properties of BST (already introduced in Chapter 2) and GST (germanium antimony telluride, $Ge_2Sb_2Te_5$) in order to implement reconfigurable metamaterials operating from UV to high-energy-visible (HEV) frequencies. This class of metamaterials would benefit applications in sensing, high-density optical memory, beam-steering, adaptive optics and light modulation**.** Here, for the first time, we demonstrate a non-volatile switchable dielectric metamaterial operating in the UV-HEV spectral range. Nano-grating metamaterials in a layered composite of low-loss ZnS/SiO_2 and the chalcogenide phase-change medium GST exhibit reflection resonances at UV-HEV wavelengths that are substantially modified by light-induced (amorphous-crystalline) phase transitions in the chalcogenide layer. Despite the presence of the lossy GST, resonance quality factors up to $Q \approx 15$ are ensured by the transparency (low losses) of ZnS/SiO_2 in the UV-HEV spectral range and values of Q increase as the refractive index of $Ge_2Sb_2Te_5$ decreases, upon crystallization. Notably however, this switching leaves resonance spectral positions unchanged.

5.2 Low Index Enabled Reconfigurable Metamaterials

Photonic metamaterials - artificial electromagnetic media structured on the subwavelength scale - are now a well-established enabling technology paradigm for engineering electromagnetic space and (actively) controlling the propagation of light and its interaction with matter [3, 14, 166]. An extensive range of enhanced and unusual optical properties, including dynamically tuneable/switchable and nonlinear functionalities, have been demonstrated at technologically important near-infrared and visible frequencies in

metamaterials and metasurfaces comprised of nanostructured plasmonic metals (very typically gold), high-index dielectrics (often silicon [38, 154, 167-169], but also GaAs [170], germanium [171], perovskites [118] and chalcogenides [22, 66]) and metal/dielectric composites.

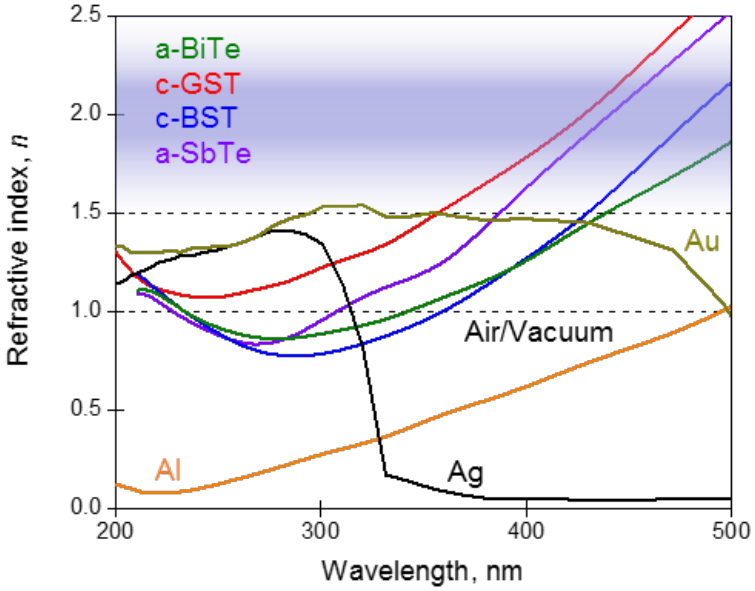

Figure 5.1: UV-high-energy visible (HEV) refractive index (real part) comparison between a selection of chalcogenides and noble metals (Al [109], Ag and Au [107]). Shaded blue/purple area indicates the refractive index of most oxides and nitrides.

However, while the ultraviolet (UV) and short-wavelength, high-energy visible (HEV) spectral range is of considerable interest and importance to a variety of applications in the physical, environmental, manufacturing and bio-sciences [172-180], it is less often the focus of attention in metamaterials research than the longer-wavelength visible / near-infrared domain. A significant factor in this, aside from dimensional requirements/constraints on nanofabrication for shorter wavelengths, is the fact that the aforementioned archetypal material platforms (gold and silicon) are unsuitable in the UV-HEV band. Alternative materials are though available: silver and aluminium for example are good plasmonic metals at short UV/HEV wavelengths beyond the reach of gold [27] (although they are subject to atmospheric degradation, i.e. oxidation/tarnishing); and materials such as diamond, alumina and zinc sulphide are transparent, relatively high-index dielectrics in this range (i.e. of sufficiently high index, relative to air as the assumed incident medium, to support Mie-type dielectric nano-cavity resonances). However, none of these are intrinsically “active” media able to provide dynamic, reversible, thermally/electrically/optically-controlled tuning and

switching functionalities. Here, we realize the first optically reconfigurable UV/HEV dielectric metasurface by hybridizing a transparent passive dielectric nanostructure with a chalcogenide that acts in this spectral range as a *low*-index phase-change medium (Figure 5.1). In this case, when the refractive index *n* of the chalcogenide material is lower than the refractive index of the surrounding material (e.g. ZnS/SiO_2); we consider it as a low-index chalcogenide.

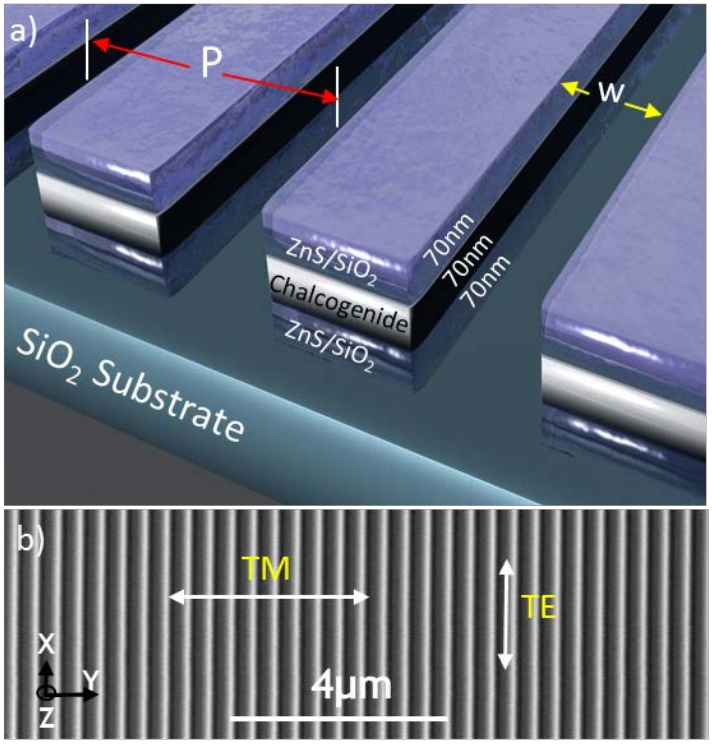

Figure 5.2: Reconfigurable UV-HEV all-dielectric metamaterials. a) Artistic cut-away section of nano-grating metamaterial structure comprising a 70 nm film of chalcogenide material (either $BiSb_5Te_9$ or $Ge_2Sb_2Te_5$) between two layers (70 nm each) of ZnS/SiO_2. b) Scanning electron microscope image of a section of such a metamaterial (dark areas being nano-grating lines milled through the tri-layer to the underlying quartz substrate).

Chalcogenide semiconductor alloys are noted for presenting an assortment of compositionally variable properties, from infrared transparency and high optical nonlinearity to photorefractivity and non-volatile phase switching between amorphous and crystalline states with often markedly different optoelectronic properties [48, 121, 181-184] as already reported in Chapter 1 and 2. As such they have been employed as functional (i.e. phase-change) dielectrics in near- to mid-IR hybrid plasmonic (noble metal) and all-dielectric metamaterials for applications including signal intensity and polarization modulation, beam steering, and multispectral imaging [22, 66, 72, 121, 185-189]. While generally known for their high refractive indices at infrared frequencies, it is less widely appreciated that chalcogenides are characteristically low-index (albeit lossy) dielectric and plasmonic media

at shorter wavelengths [34, 105, 189, 190]. Indeed, in the UV/HEV spectral range, they can have lower refractive indices than many oxides, nitrides and perovskites. Here we harness their phase-switchable character to realise the first optically reconfigurable UV/HEV dielectric metamaterials, in which the functional chalcogenide is hybridised with a transparent, high-index dielectric nanostructure supporting the resonant mode. Laser-induced crystallization of the amorphous chalcogenide decreases its refractive index and is found to increase metamaterial resonance quality *without* spectrally shifting the resonance and *in spite of* the fact that the crystalline phase has a higher extinction coefficient.

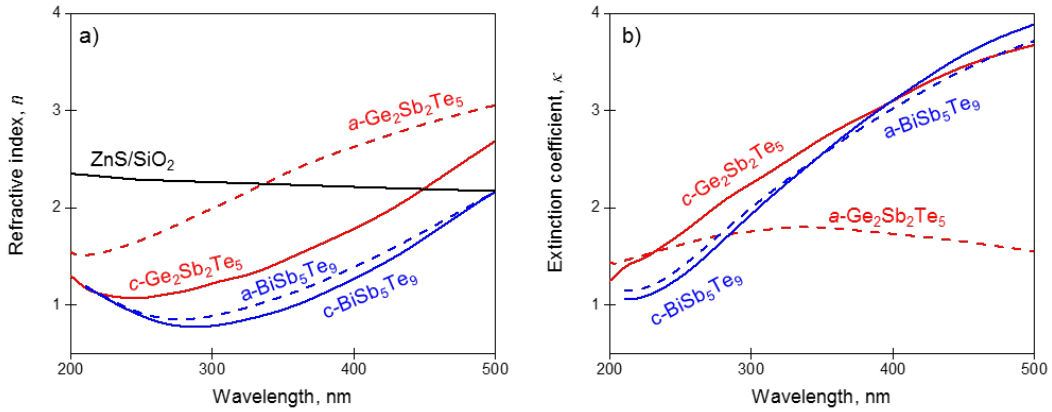

Figure 5.3: UV-High energy visible optical properties of GST and BST. a) Comparison of the spectral dispersion of refractive index, *n*, of $BiSb_5Te_9$ and $Ge_2Sb_2Te_5$ in their respectively amorphous and polycrystalline phases with ZnS/SiO_2. b) Spectral dispersion of extinction coefficient, *κ*, of $BiSb_5Te_9$ and $Ge_2Sb_2Te_5$ in their corresponding amorphous and polycrystalline phases across the UV/visible spectral region.

For the realization of these reconfigurable metasurfaces we first design the structure by implementing a 2D finite-difference-time-domain (FDTD) model. The structure is formed of a chalcogenide thin film sandwiched between two dielectric layers as represented in Figure 5.2. For simplicity, we assume the same thickness equal to 70 nm for all the three layers and we first consider BST as the chalcogenide film (with stoichiometry $BiSb_5Te_9$ as a case study) and ZnS/SiO_2 in a 1:9 at.% ratio as the dielectric layers. ZnS/SiO_2 is a passive dielectric with negligible losses across this spectral range and exhibits a relatively flat dispersion of *n* close to 2.4. The model employs ellipsometrically measured values for the complex permittivity of ZnS/SiO_2 and $BiSb_5Te_9$ in its amorphous and polycrystalline state. Moreover, it assumes lossless non-dispersive refractive index of 1.46 for the semi-infinite quartz substrate; normally-incident narrowband plane wave illumination and, by virtue of periodic boundary conditions, a nano-grating pattern of infinite extent in the x-y plane. Numerical simulations of reflection spectra for the design represented in Figure 5.2 are reported in Figure 5.4a and

reveal that despite the quite sharp resonances (*Q*-factor around 20, calculated as $Q = \Delta\lambda/\lambda_R$, where λ_R is the resonance wavelength and $\Delta\lambda$ is the spectral half-maximum linewidth) observed in the reflection spectra, the switching contrast between amorphous and polycrystalline $BiSb_5Te_9$ is quite low. In fact, the change in the optical constants of $BiSb_5Te_9$ between the amorphous and polycrystalline phase is small as can be seen in Figure 5.3. Hence, we decided to investigate also another chalcogenide material for this application that is $Ge_2Sb_2Te_5$ (or GST), a well-known phase change material widely used in rewritable optical (DVD's & Blu-ray) and electronic data storage (PCRAM) technologies. The results shown in Figure 5.4b assume the same metasurface design used for BST, but the replacement of BST with GST provides a much larger switching contrast ratio between the amorphous and polycrystalline case compared to what reported in Figure 5.4a. In fact, the optical constants of GST show a larger change than the ones of BST between the amorphous and polycrystalline phase (Figure 5.3). Specifically, GST exhibits a lower index than ZnS/SiO_2 at wavelengths shorter than 450 nm in the amorphous phase and shorter than 338 nm in the crystalline phase (Figure 5.3a and b). The index contrast between ZnS/SiO_2 and crystalline GST is higher across much of the UV range, as crystallization brings about an overall decrease in the refractive index of GST. Across this spectral range, GST in both structural phases, exhibits an extinction coefficient (κ) above 1 with an increasing contrast between the two phases at higher wavelengths (Figure 5.3b). It therefore cannot sustain high Q-factor all-dielectric resonances across this spectral range unless it is combined with a low loss medium such as ZnS/SiO_2.

Based on the results obtained by numerical simulation, we decided to use GST for the experimental implementation of low-index enabled reconfigurable metasurfaces.

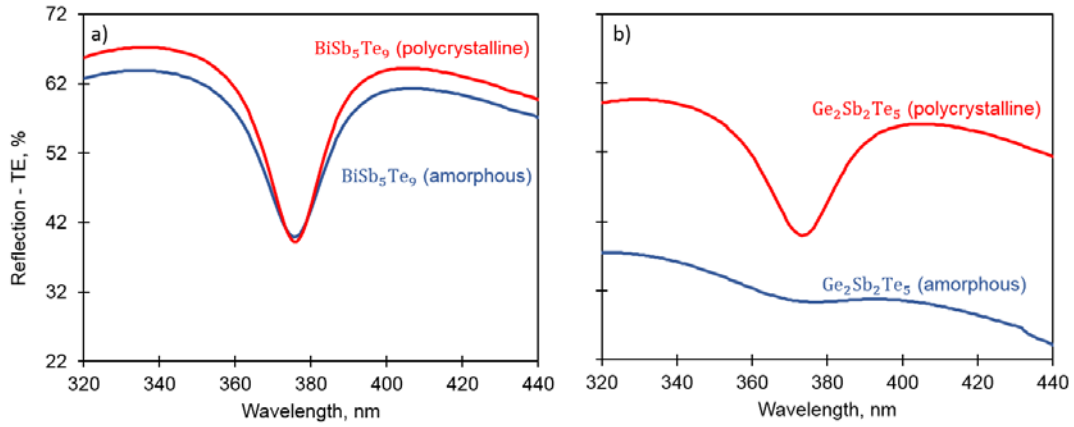

Figure 5.4: Numerically simulated reflection spectra for low index enabled reconfigurable metasurfaces based on $BiSb_5Te_9$ (a) and $Ge_2Sb_2Te_5$ (b) in their corresponding amorphous (blue curves) and polycrystalline states (red curves). The subwavelength nanogratings period is 300 nm and the grating groove width is 40 nm.

Metamaterial structures were fabricated in a tri-layer of 70 nm GST between two 70 nm layers of ZnS/SiO_2 deposited on optically flat silica substrates by RF sputtering (Kurt J. Lesker Nano 38) from $Ge_2Sb_2Te_5$ and $ZnS:SiO_2$ (1:9) targets. A base pressure of 5×10^{-7} mbar was achieved prior to deposition and high-purity argon was used as the sputtering gas. The substrate was held within 10 K of room temperature on a rotating platen 150 mm from the target so as to produce low-stress amorphous films. Sub-wavelength period (i.e. non-diffractive) grating patterns, with a fixed linewidth $W \approx 50$ nm and periods P ranging from 300 to 400 nm, each covering an area of approximately 20 µm × 20 µm, were etched through the ZnS/SiO_2–GST–ZnS/SiO_2 tri-layer by focused ion beam (FIB) milling (FEI Helios NanoLab 600), as illustrated in Figure 5.2).

The amorphous-to-crystalline transition in chalcogenides is an annealing process that can be initiated uniformly over an entire sample by increasing the ambient temperature to a point above the material's glass-transition point T_g (~160°C for GST) but below its melting point T_m (~600°C)[191], or by locally applying electrical current or laser-induced heating, as in the present study: transitions in the GST layer from the as-deposited amorphous state to the crystalline state were excited using trains of fifty 85 fs, 140 $mJ \cdot cm^{-2}$ laser pulses at a wavelength of 730 nm and a repetition rate of 1 MHz. Normal-incidence reflection characteristics of the unstructured tri-layer and the nano-grating metamaterials were quantified using a microspectrophotometer (CRAIC QDI2010) with a sampling domain size of 10 µm × 10 µm and numerical aperture of 0.28.

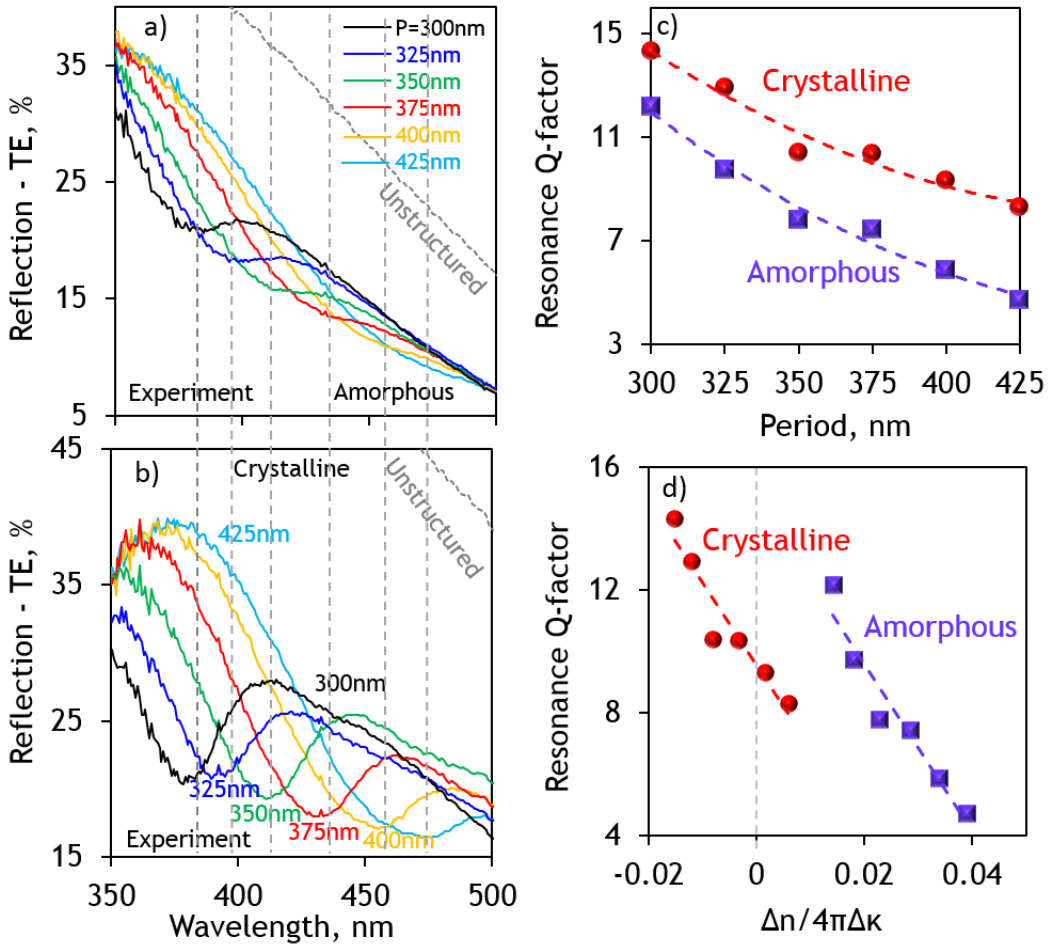

Figure 5.5: Optical properties of of ZnS/SiO_2–GST metamaterials.a, b) Measured spectral dispersion of ZnS/SiO_2–GST–ZnS/SiO_2 nano-grating metamaterial TE reflection for a selection of grating periods *P* (as labelled), for the amorphous a) and polycrystalline b) states of the GST layer, overlaid with corresponding spectra for the unstructured tri-layer (dashed lines). c) Measured resonance quality factor *Q* as a function of metamaterial period *P*. d) Measured resonance *Q* as a function of confinement figure of merit.

The reflectivity of the unstructured ZnS/SiO_2–GST–ZnS/SiO_2 tri-layer is higher when the GST layer is in its crystalline state than when it is in the amorphous state, and in both cases decreases monotonically with increasing wavelength over the UV to high energy visible spectral range, as shown in Figure 5.5a, b. The nano-grating metamaterial structures present reflection resonances for incident light polarised parallel to the grating lines (along the *x* direction defined in Figure 5.2b; or the TE orientation of the grating) at spectral positions dependent upon the period *P,* but not upon the phase state of the GST layer (Figure 5.5a-d), as may be expected on the basis of prior works relating to the switching and tuning of metamaterial resonances (e.g. via a near-field refractive index change or nano-mechanical reconfiguration [22, 66, 192]). Here, the amorphous-to-crystalline transition in the GST layer brings about an increase in the quality-factor of the resonances ($Q = \Delta\lambda/\lambda_R$) by a factor of up

to 1.7, without a change in spectral position (Figure 5.5c). For both phase states of GST, *Q* decreases with increasing metamaterial period *P*, which is to say with increasing resonance wavelength λ_R. This is as a result of the changing balance between the refractive indices of GST (in either phase) and that of ZnS/SiO_2: *Q* is largest for the shortest period gratings (shortest, UV resonance wavelengths) with GST in the crystalline phase, where $\Delta n = n_{GST} - n_{ZnS/Sio_2}$ assumes its largest negative value; and smallest for the largest period gratings (longest, HEV resonance wavelengths) with GST in the amorphous state, where Δn takes its largest positive value (Figure 5.5d).

That the balance between the refractive indices of GST and ZnS/SiO_2 is the key determinant of metamaterial resonance quality is further illustrated by the fact that *Q* increases with GST crystallisation, i.e. with decreasing GST index (increasing index contrast *Δn*), in spite of the associated increase in GST extinction coefficient *κ* (Figure 5.3). This is because the chalcogenide's extinction coefficient in either phase state is much larger than that of the ZnS/SiO_2. That said, values of *κ* for the crystalline phase are higher and increase more rapidly with wavelength than for the amorphous phase, and this is a factor in the dispersion of *Q*. Indeed, the same proportionality is seen (Figure 5.5d) for both phase states between *Q* and the figure of merit F_3 (defined as Eq. (2.17) in section 2.5.4) [193] indicative of a medium's suitability as a platform for resonant all-dielectric metamaterials.

The observed change in metamaterial resonance quality *Q* without an associated change in resonance wavelength λ_R, is made possible by the fact that the structural transition in the GST layer predominantly affects the distribution and confinement of field in the overlying ZnS/SiO_2 layer.

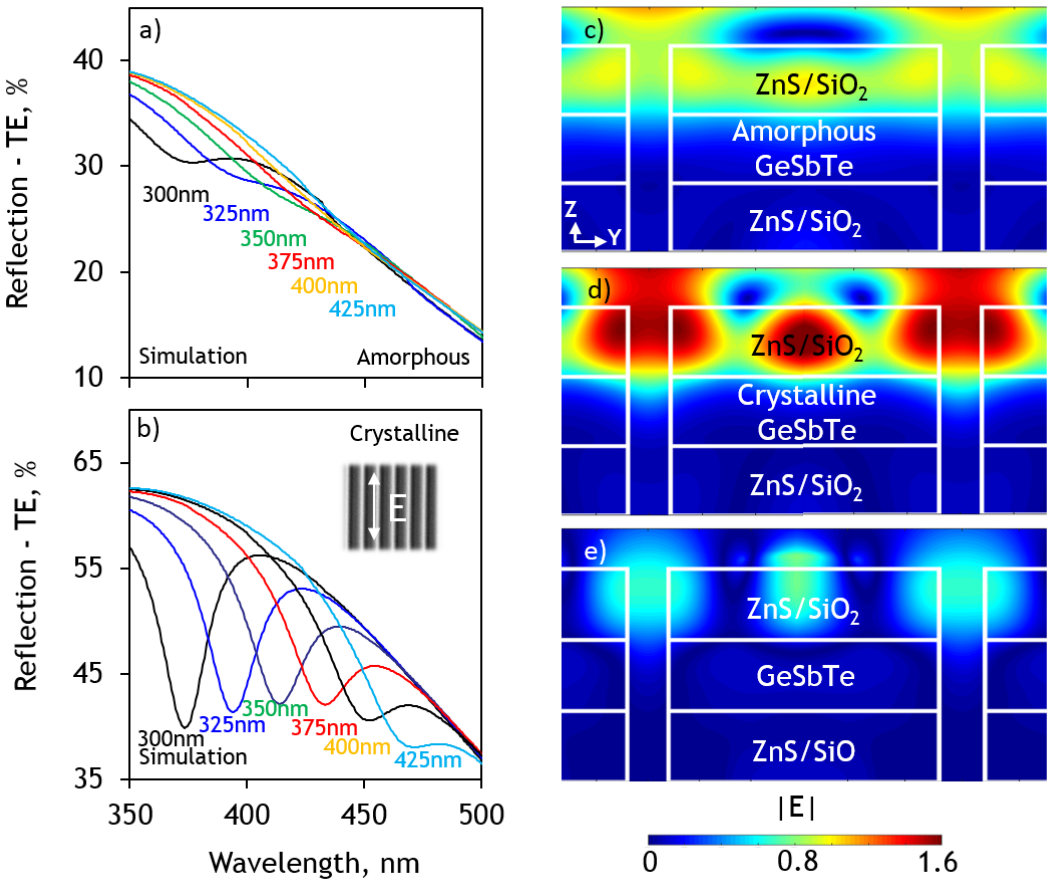

Figure 5.6: Numerically simulated optical response of hybrid chalcogenide phase-change medium / transparent dielectric metamaterials.a, b) Spectral dispersion of ZnS/SiO_2–GST–ZnS/SiO_2 nano-grating metamaterial TE reflection for a selection of grating periods P (as labelled), for the amorphous (a) and polycrystalline (b) states of the GST layer. c, d) Distributions of the normalized electric field, |E| in the yz-plane for a nano-grating period P = 300 nm at its reflection resonance wavelength λ_R = 375 nm for the amorphous c) and polycrystalline d) states of the GST layer. e) Corresponding change in the strength and spatial distribution of field between the two phase states of the GST layer, evaluated as the difference between panels c) and d).

Figure 5.6 show results of a 2D finite-difference-time-domain (FDTD) model which is the same described initially to simulate the BST and GST metasurfaces in both amorphous and crystalline states. There is very good qualitative and quantitative agreement between experimentally measured (Figure 5.5a, b) and numerically simulated (Figure 5.6a, b) reflection spectra for the tri-layer metamaterials, for both the amorphous and crystalline states of the GST layer. Minor discrepancies are attributed to manufacturing imperfections, i.e. deviations from the ideal model geometry such as slight over-milling of grating lines into the substrate, and the tapered/rounded cross-sectional profile of milled lines; and to contamination/stoichiometric change in the ZnS/SiO_2 and/or GST layers during FIB milling, which may slightly modify refractive index.

These simulations show that for any given metamaterial period, the decrease of GST layer

refractive index associated with its crystallization enhances field confinement (local field strength) in the overlying ZnS/SiO_2 layer (Figure 5.6c, d). There is consequently an increase in resonance quality *Q* without a change in resonance wavelength λ_R and despite the higher extinction coefficient of crystalline (as compared to amorphous) GST because there is minimal penetration of fields into the GST layer in either phase state. Interestingly, the differential field map shown in Figure 5.6e indicates that local fields are enhanced upon GST crystallization both within the ZnS/SiO_2 and in the gaps between the nano-grating lines. This is distinctly different to reconfiguration based on classical plasmonic and all-dielectric metasurfaces, where the field switching occurs either in the gap of a plasmonic material or the body of the nanostructured high-index layer, not both.

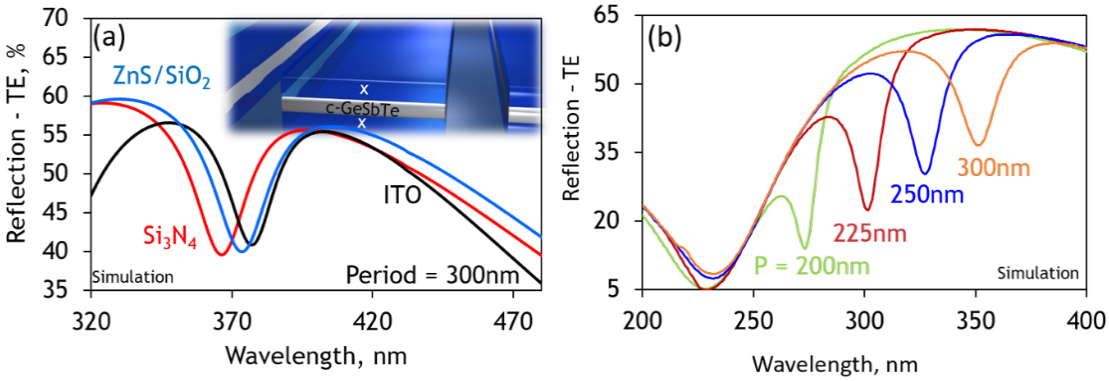

Figure 5.7: Potential of low index enabled metasurfaces. a) Numerically simulated reflection spectra for a grating period P = 300 nm for a selection of low loss dielectrics (as labelled), with the GST layer in its lower index polycrystalline phase. b) Numerically simulated reflection spectra for a selection of grating periods P (as labelled), for the polycrystalline state of the GST layer showing optical resonances deep into the UV.

Although we have chosen ZnS/SiO_2 for the current experimental demonstration, the demonstrated device configuration is a universal method that enables adding reconfigurable non-volatile memory functionality to any low loss material used for all-dielectric metasurfaces across the UV/visible spectral range. This can be observed from Figure 5.7a, where simulated reflection properties for a nanograting metasurface, illuminated with TE polarised light, is demonstrated with SiN and ITO as the high index top layer, showing identical results to that of ZnS/SiO_2. This demonstrates the versatility of the proposed devices. Furthermore, while, due to instrument limitations, we have experimentally demonstrated metasurfaces with resonances down to λ = 375 nm, if GST is used as the low index layer, the demonstrated method enables the engineering of resonances down to λ = 270 nm by simply reducing the period of the demonstrated structure (Figure 5.7b).

5.3 Results and Discussion

The experimental observed resonances described in the previous section have two contributions, namely there is a confinement effect of the electromagnetic field in the top layer due to the lower refractive index of the underlying chalcogenide film and also a plasmonic contribution from the interface between ZnS/SiO_2 and GST when it is in the polycrystalline phase. In the experimental case, these contributions are intimately correlated because *c*-GST is plasmonic (ε_1 is negative in the UV/visible spectral range) and has also a lower refractive index than ZnS/SiO_2 below 450nm. Hence, in order to separate these effects and quantify the contribution of each ones into the optical properties of the studied metasurfaces, we consider a low index enabled metasurface based on a hypothetical layer characterized by a constant n with varying κ sandwiched between two films of ZnS/SiO_2. The model is the same described in the previous section with subwavelength nanogratings period of 300 nm and a grating groove width of 40 nm. The corresponding numerically simulated reflection spectra are shown in Figure 5.8a and we notice that the resonance shifts continuously and smoothly from the situation where the effect is purely due to the low refractive index (n = 0.7 and κ = 0) since ε_1 is positive ($\varepsilon_1 = n^2 - \kappa^2 = 0.49$) to the case where both effects are present since the hypothetical layer is also plasmonic (n = 0.7 and κ = 3). These two regime are characterized by a different spectral dependency of the resonance, namely the resonance shifts in a nonlinear way when the hypothetical layer is not plasmonic and it moves linearly when the layer is plasmonic ($\kappa > 0.7$). This is represented in Figure 5.8b where resonance wavelengths are extracted as a function of κ.

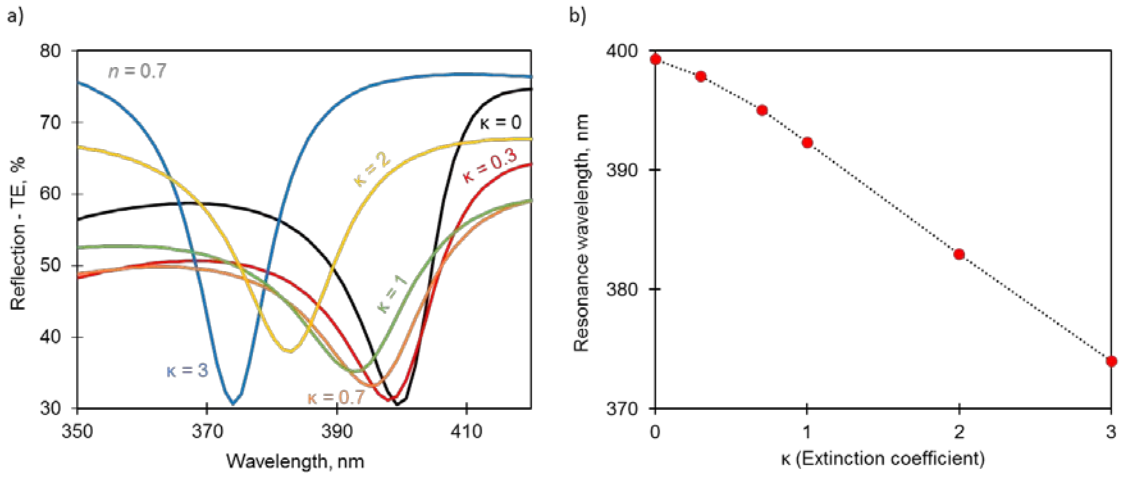

Figure 5.8: a) Numerically simulated reflection spectra for low index enabled metasurfaces based on a hypothetical layer characterized by a constant *n* with varying *κ* sandwiched between two films of ZnS/SiO_2. The subwavelength nanogratings period is 300 nm and the grating groove width is 40 nm. b) Resonance wavelengths plotted as a function of κ extracted from panel a).

Furthermore, the optical response of the simulated metasurfaces shows that is possible to obtain a spectral shift of a metamaterial resonance by changing only κ while commonly the extinction coefficient influences the spectral width of the resonance and the spectral shift is observed by varying n. This phenomenon is related to the fact that there is a smooth transition from a dielectric with low refractive index (for instance n = 0.7) to a plasmonic material. This is further confirmed by extracting the cross-sectional distribution of normalised electric field for three different values of κ maintaining the same n at the corresponding resonance wavelength (Figure 5.9) that are observed in the reflection spectra presented in Figure 5.8a. These field maps reveal that the excited mode at the resonance wavelength has similar features from the case with κ = 0 to the one with κ = 3. However, as the middle layer becomes plasmonic (larger κ at constant n) the electric field is progressively more confined in the top layer of the metasurface showing also a higher enhancement of the field.

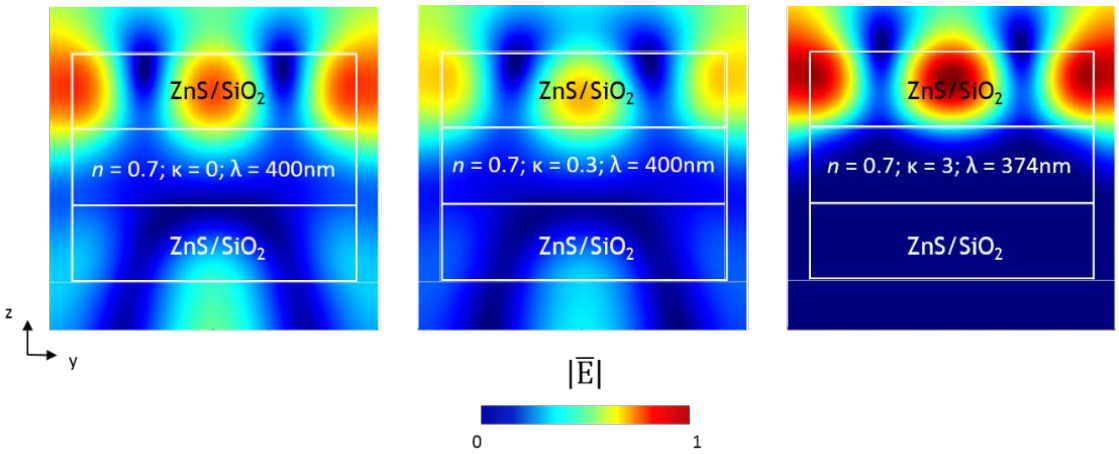

Figure 5.9: Distributions of the normalized electric field, *E* in the yz-plane for subwavelength nanogratings with period 300 nm characterized by a three-layer structure where the middle layer is a hypothetical material with constant n and varying κ from 0 to 3 as labelled in the figure. The field distributions are plotted at the corresponding resonance wavelength observed in the reflection spectra shown in Figure 5.8a.

5.4 Summary

In conclusion, we demonstrate an approach to non-volatile switching of dielectric metamaterial optical properties in the UV/HEV spectral range: by combining a chalcogenide phase-change medium with a transparent high-index dielectric, we realize a hybrid nanostructure in which optically-induced (amorphous-crystalline) phase switching of the chalcogenide component changes the quality of metamaterial resonances based upon optical field confinement in the dielectric *without* affecting their spectral position. Moreover, counterintuitively, metamaterial resonance quality increases as the extinction coefficient of

the chalcogenide increases.

In the present case, we utilize $Ge_2Sb_2Te_5$ (GST) as the functional phase-change medium and ZnS/SiO_2 as a transparent dielectric (of sufficiently high refractive index relative to the incident medium as to support dielectric cavity resonances when nanostructured) – achieving, for a simple nano-grating metamaterial design - a maximum reflection resonance quality factor $Q \approx 15$ at a wavelength of 380 nm and a change in Q of at least 20% with GST phase switching. The concept though may be applied for the introduction of non-volatile switching (memory) functionality to a variety of otherwise passive UV/HEV material platforms for all-dielectric metamaterials: higher quality factors may be achieved through the use of higher-index dielectrics and/or lower-index chalcogenides – there are, for example, BiTe and SbTe alloys which offer sub-unity refractive indices in the UV-visible spectral range[190, 193], albeit with reduced switching contrast between phase states as compared to GST. The mechanism is furthermore scalable to other spectral bands, presenting possibilities for non-volatile switching in a wide variety of meta-surface 'flat-optic' applications.

Furthermore, we study a low index enabled metasurface based on a hypothetical layer characterized by a constant n with varying κ sandwiched between two films of ZnS/SiO_2 and demonstrate that is possible to shift the spectral position of a metamaterial resonance by changing only the extinction coefficient while commonly it influences only the spectral width of the resonance and the spectral shift is observed by varying n. This phenomenon is related to the fact that there is a smooth transition from a dielectric with low refractive index (for instance $n = 0.7$) to a plasmonic material.

Chapter 6

Conclusions and Future Work

6.1 Conclusions

The main objective pursued in this thesis was the exploration of chalcogenides as a new material platform to manufacture metamaterials in the UV-visible and near-IR spectral range. Specifically, binary and ternary alloys of BST have been investigated showing high-index dielectric, epsilon-near-zero, topological insulator and plasmonic behaviour depending on composition and spectral range. The study of the relationships between properties and composition has been achieved through a high-throughput methodology that consists on coevaporation of pure elements for the synthesis of solid-state material combinatorial libraries and further parallel characterization to optimize the synthesis for specific applications. The original contributions of this work are revised below in more detail.

6.1.1 Chalcogenide Semiconductor Alloys for Photonic Applications

In chapter 2, from a systematic study enabled by high-throughput physical vapour deposition and characterization techniques, we derive stoichiometric dependences of the spectrally dispersive photonic properties of binary and ternary bismuth antimony telluride (BST) chalcogenide alloys.

According to composition, it is found that as-deposited thin films can be low-index/low-epsilon and plasmonic materials from the near ultraviolet to the visible range and high-index dielectrics in the near-infrared spectral region. We consider three different figures of merit to assess the BST alloys manufactured here and compared their properties with other well-known materials for nanophotonic and metamaterial applications. Based on that, BST chalcogenides have higher values of F_1 (Figure 2.20) - than titanium nitride and transparent conductive oxides (specifically aluminium- and gallium-doped zinc oxide, and indium tin oxide) over the near-UV to near-IR spectral range. Moreover, they are comparable if not superior to gold at wavelengths below 580 nm and silver below 365 nm. Over the entire

spectral range of interest here, the highest values of F_1 (coming within a factor of ~2 of that of Al at around 800-900 nm) are provided by the ternary alloy $Bi_5Sb_3Te_2$. This value is more than sufficient to support long-range SPPs in an insulator-metal-insulator waveguide as shown in Figure 2.23. On the basis of F_2 (Figure 2.21), BST alloys are better than silver below ~330 nm, gold below ~512 nm, TiN below ~690 nm, and TCOs below ~1400 nm. $Bi_5Sb_3Te_2$ is again among the best compositions, presenting a value of F_2 for near-UV/visible wavelengths that is comparable to that of TiN over the near-IR range and to TCOs at the upper limit of the spectral range under consideration. It achieves a maximum value of F_2 equal to 1.64 at 350 nm, which is more than sufficient to support high quality resonances [105]. This is further illustrated by the numerically simulated optical response of subwavelength period nano-grating metasurfaces of varying composition presented in Figure 2.24: the resonance observed in reflection mode has a higher quality-factor for $Bi_5Sb_3Te_2$ compared with other compositions that have a lower F_2. As a high-index dielectric, BST comes into its own at near-IR wavelengths, with values of F_3 (Figure 2.22) exceeding those of TCOs above ~1220 nm. The highest figures of merit are offered by the binary composition Sb_3Te_8 – values come within a factor of 2 of those of germanium (at around 700-800nm), though by virtue of losses are much lower than those of silicon. This value of F_3 is sufficient to support high dielectric Mie resonances as presented in Figure 2.25. Within the compositional range accessible to the present study: $Bi_5Sb_3Te_2$ is identified as the best plasmonic stoichiometry (highest figures of merit for both propagating and localized surface plasmon modes); near-IR refractive indices as high as n = 11.5 are found in certain ternaries but Sb_3Te_8 presents the highest ratio of refractive index to extinction coefficient (as a figure of merit for high-index dielectric applications); all compositions have a near- or sub-unity minimum value of refractive index in the near-UV range (the lowest measured value being n = 0.7 at 296 nm for $BiSb_3Te$); $Bi_2Sb_5Te_{18}$ provides a value of epsilon $|\varepsilon|$ that is nearest to zero ($|\varepsilon|$ = 2.27 at 230 nm).

BST is of course only one member of a large extended family of chalcogenide materials, which remain to be explored for their nanophotonic applications potential. High-throughput combinatorial techniques, as presented here, can enables rapid, systematic surveys of optical, electronic and structural properties, and thereby optimization via compositional design of material characteristics towards specific application requirements.

In Figure 1.1 the optical properties of conducting materials are classified according to three parameters: the carrier concentration, the carrier mobility and the interband losses. This is based on the fact that the UV/visible plasmonic properties of noble metals derive from the excitation of free charges and so elemental materials such as antimony and bismuth that have a relatively low carrier concentration (in the order of 10^{19} cm^{-3}) are categorised as

materials for plasmonic applications in the mid-IR. However, BST chalcogenides and p-block semiconductors in general (i.e., compounds of elements in groups 13 [IIIA] to 18 [VIIIA] of the periodic table, with valence electrons in the p-orbital), possess plasmonic properties in the UV/visible range from the excitation of strong interband transitions and this is different from the mechanism present in noble metals (excitation of free charges in p-block semiconductors is relevant only at much longer wavelengths, i.e. mid-IR) [105]. For this reason, BST chalcogenides can be used for plasmonic applications in the UV/visible and according to the figures of merit, F_1 and F_2, they have better plasmonic properties than silver below ~330 nm and gold below ~512 nm.

6.1.2 Plasmonic and Phase Change Properties of Bi:Te for Metamaterials Application

In chapter 3 we zoom in on Bi:Te, one of the corresponding binary alloys of BST, and we demonstrate that amorphous Bi:Te can serve as a compositionally tunable material platform for UV/visible plasmonics. The plasmonic character of the chalcogenide is illustrated via the fabrication of subwavelength period nano-grating metasurfaces, which present a highly anisotropic optical response: under TM-polarized illumination (incident electric field perpendicular to the grating lines) plasmonic absorption resonances are manifested as period-dependent variations in the perceived colour of the nanostructured domains, while for TE-polarized light the metasurface domains are almost indistinguishable from unstructured Bi:Te.

Moreover, we study the phase change properties of this alloy revealing that the change on the optical properties with the phase transition between the amorphous and the crystalline state is a modest variation overall with an average change in F_2 of 11 % and in F_3 of 20 % at 1310 nm and 26 % at 1550 nm. However, a change of 55% in F_2 is observed for compositions around Te content of 76% (Bi 24%) suggesting that Bi:Te material system presents phase change properties for these compositions, but in a weaker form compared to other well-known phase change materials like $Ge_2Sb_2Te_5$ and GeTe [122]. Furthermore, these phase change properties might be associated with Te segregation after the annealing that results in the formation of a material with two mixed phases, namely polycrystalline Bi_2Te_3 and polycrystalline Te.

In conclusion, we have shown that Bi:Te alloy is a compositional adaptable material base for plasmonics and nanophotonics with compositionally controlled optical properties. While presenting a plasmonic response in an as-deposited amorphous thin film that holds a

significant advantage over bulk and solution-processed crystalline chalcogenides (and various other “alternative plasmonic” media) in terms of device production process compatibility and scalability. Alongside established credentials as a thermoelectric medium [128], and the possibility of non-volatile electrically/optically-induced phase-change switching of properties [122, 123], it presents intriguing possibilities for the control of photons and electrons in thin film thermo/opto-electronics, including for aesthetic purposes (e.g. harnessing plasmonic “structural colour” in building-integrated thermoelectric devices).

6.1.3 Epsilon-Near-Zero Properties of Sb_2Te_3

In chapter 4 we report on ENZ phenomena in metamaterials that is one of the most intriguing topic of nanophotonics since ENZ behaviour has both an important fundamental interest and a profound technological impact that enables the observation of unusual phenomena and the design of unconventional devices [132]. However, most of ENZ phenomena have been studied in the microwave range while the optical spectral range is still largely unexplored.

We show, using experimentally measured material parameters for vapour deposited antimony telluride (Sb_2Te_3) in a series of numerical simulations, that optical frequency low-epsilon and near-unity index behaviours may be observed even in the presence of realistic losses. Sub-wavelength slots filled with the amorphous chalcogenide can serve as conduits for the “laminar flow” transmission of UV-visible light through a plasmonic metal screen: localized enhancement and powerflow “turbulence” in the optical near-field around open apertures in the screen are suppressed, producing a broadband enhancement of transmission. However, transmission is not strongly enhanced at the low-loss epsilon-nearest-zero wavelength. Indeed a reduction of losses in the chalcogenide is found to suppress transmission at this point and can increase, rather than decrease, metasurface absorption depending on the magnitude of refractive index and the extent of index matching to the surroundings. Moreover, for a given cross-sectional area, the transmission of an ENZ channel (in a straight line through a given thickness of metal) is entirely independent of the channel shape and largely insensitive to angle of incidence up to 40°.

We also study these phenomena experimentally by realizing empty and filled with Sb_2Te_3 aluminium nano-slit array metasurfaces. The spectral range explored experimentally is at longer wavelengths compared to the simulations reported at the beginning of chapter 4; however, we can observe the same counter-intuitive behaviour: the etching of nano-slits through a semi-transparent film reduces its transmission while it is usually expected that the removal of material produces an increase of transmission. Moreover, by filling these nano-

slits with a relatively lossy material which $\varepsilon_1 \approx 0$ (but negative), transmission is increased; instead, by filling the nano-slits with a dielectric ($\varepsilon_2 \approx 0$), transmission remains as low as for empty nano-slits. Thus, this peculiar behaviour can be understood through the optical energy whirlpools introduced in the first part of chapter 4, namely these whirlpools with powerflow oriented in the backward direction relative to incident light are responsible of the reduction of transmission, while the presence of a material with negative ε_1 close to zero removes these whirlpools and established a laminar flow of energy that increases the overall transmission of the metasurface.

6.1.4 Reconfigurable Ultraviolet and High-Energy-Visible Dielectric Metamaterials

In chapter 5 we demonstrate an approach to non-volatile switching of dielectric metamaterial optical properties in the UV/HEV spectral range: by combining a chalcogenide phase-change medium with a transparent high-index dielectric, we realize a hybrid nanostructure in which optically-induced (amorphous-crystalline) phase switching of the chalcogenide component changes the quality of metamaterial resonances based upon optical field confinement in the dielectric *without* affecting their spectral position. Moreover, counterintuitively, metamaterial resonance quality increases as the extinction coefficient of the chalcogenide increases.

In the present case, we utilize $Ge_2Sb_2Te_5$ (GST) as the functional phase-change medium and ZnS/SiO_2 as a transparent dielectric (of sufficiently high refractive index relative to the incident medium as to support dielectric cavity resonances when nanostructured) – achieving, for a simple nano-grating metamaterial design - a maximum reflection resonance quality factor $Q \approx 15$ at a wavelength of 380 nm and a change in Q of at least 20% with GST phase switching. The concept though may be applied for the introduction of non-volatile switching (memory) functionality to a variety of otherwise passive UV/HEV material platforms for all-dielectric metamaterials: higher quality factors may be achieved through the use of higher-index dielectrics and/or lower-index chalcogenides – there are, for example, BiTe and SbTe alloys which offer sub-unity refractive indices in the UV-visible spectral range[190, 193], albeit with reduced switching contrast between phase states as compared to GST. The mechanism is furthermore scalable to other spectral bands, presenting possibilities for non-volatile switching in a wide variety of meta-surface 'flat-optic' applications.

Furthermore, we study a low index enabled metasurface based on a hypothetical layer

characterized by a constant *n* with varying *κ* sandwiched between two films of ZnS/SiO_2 and demonstrate that is possible to shift the spectral position of a metamaterial resonance by changing only the extinction coefficient while commonly it influences only the spectral width of the resonance and the spectral shift is observed by varying *n*. This phenomenon is related to the fact that there is a smooth transition from a dielectric with low refractive index (for instance *n* = 0.7) to a plasmonic material.

6.2 Future Work

The work reported in this thesis about the development of new material systems for photonic metamaterials have still open questions for future work.

Specifically, further investigation is required on:

- exploration of topological insulator properties of BST material system in its amorphous and crystalline form; so far the topological properties were studied via angle resolved photoemission spectroscopy (ARPES) only for crystalline compositions of BST with stoichiometry $(Bi_{(1-x)}Sb_x)_2Te_3$ $(0 < x < 1)$ [83]. Hence, it would be interesting to investigate the topological insulator properties for a wider compositional spread; moreover, a novel theoretical demonstration of realizing topological phases in amorphous systems was recently reported showing that amorphous solids with spin-orbit coupled motifs can host topologically insulating phases [194, 195]. In particular, their analysis establishes that local interactions and local geometric arrangements are sufficient to generate chiral edge modes, since long-range spatial order is not necessary [195]. Based on that, we fit the ellipsometry measurements for amorphous compositions of BST assuming a material structure consisting of a bulk semiconductor with a thin metal film on top (Figure 6.1) as it was done in ref. [33] and we find out that this model adequately describes the optical properties of these amorphous phases. Hence, this point out that BST amorphous compositions could be topological insulators and this could be the first experimental demonstration of realizing three-dimensional amorphous topological insulators in an electronic system. However, the confirmation of these results requires ARPES measurements.

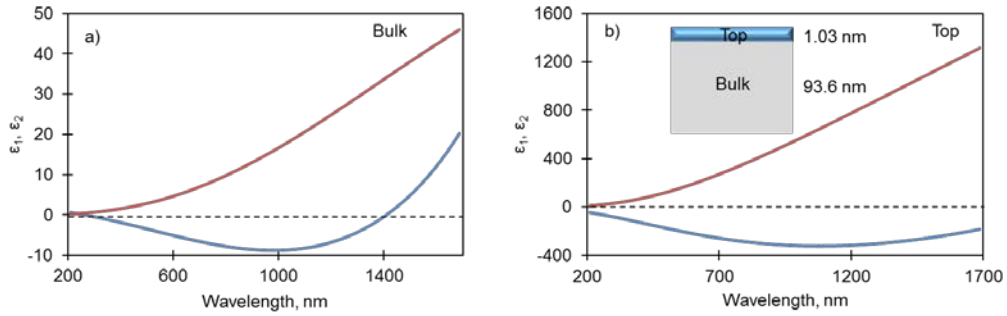

Figure 6.1: Dielectric function of amorphous BST (composition: Bi 17%, Sb 47%, Te 36%) retrieved from ellipsometry assuming a material structure consisting of a bulk semiconductor with a thin metal film on top; this structure is sketched in the inset of panel b). a) Dielectric function of the bulk and b) corresponding dielectric function of the top layer.

- Investigation of phase change properties for Bi-rich compositions of Bi:Te system; in chapter 3 we study the optical phase change properties of Te rich compositions of Bi:Te; however, in ref. [104] it is reported that other crystallographic phases than Bi_2Te_3 exist in the Bi:Te system such as tsumoite (BiTe) and pilsenite (Bi_4Te_3), while the optical properties of these phases have not been explored so far.
- Experimental study of the ENZ properties of antimony telluride-based metasurfaces; in chapter 4 we reported on the ENZ properties of nanohole arrays filled with Sb_2Te_3 and we described a first experimental realization of these metasurfaces. Nevertheless, the spectral range explored experimentally is at longer wavelengths compared to the simulations reported at the beginning of chapter 4; thus, it will be interesting to study experimentally the optical properties in the same spectral range of the simulation.

Appendix A

Tools and Techniques

In this section, a brief description of the fabrication techniques and the main characterization instruments is given. The first step in the fabrication of planar metamaterials consists on the deposition of a thin film and in this work, evaporation techniques and sputtering were used. The characterization of the structural properties of the deposited thin films was performed via x-ray diffraction and Raman spectroscopy in conjunction with energy dispersive x-ray spectroscopy to determine the chemical composition. The corresponding optical properties in the UV/visible/near-IR spectral range were retrieved by variable angle spectroscopic ellipsometry. The second fabrication step requires the patterning at the nanoscale of the deposited thin film to create a metamaterial and this was achieved through a focused ion beam instrument. The optical response in the UV/visible/near-IR spectral range of the fabricated metamaterials was measured by a CRAIC microspectrophotometer and compared with the results obtained with numerical simulations.

A.1 Deposition Techniques

Three main deposition techniques were used in this work:

- resistive evaporation is a common technique used to deposit thin films. The source material is heated in a vacuum chamber to the point that vapour particles are formed and travel to the substrate where they condense. In resistive evaporation the source material is contained in a crucible where the transit of a large current heats the material causing the evaporation. The instrument used in this work is a BOC Edwards resistance evaporator that works in high-vacuum conditions, i.e. base pressure of 1×10^{-6} mbar.
- Sputtering is a physical phenomenon that consists of the ejection of atoms from a target and the deposition of a thin layer of the extracted material on a substrate [90]. This process is accomplished by the collision of ions with the surface of the target material in the presence of high voltage. The formation of ions occurs via a glow

discharge mechanism produced in a vacuum chamber under pressure controlled gas flow. This results in the creation of a plasma, which is a partially ionized gas with a zero net charge. The applied potential is always lower for the target in order to attract the positive ions and obtain the bombardment of its surface. The sputtered gas is usually an inert gas like argon, but in some cases also reactive gas like oxygen or nitrogen are added to deposit compounds such as oxides and nitrides. There are different sputtering configurations and the main ones are diode sputtering, magnetron sputtering and RF (radiofrequency) sputtering. Only the last one was used in this work and it will be described further. This technique is used to sputter non-conducting materials, because when an ion hits the target, an electron is released from the surface and combines with the ions neutralizing it. If the target material is dielectric this mechanism creates a charged layer on the surface and the ions are no longer attracted from the target, hence electrons are not released and the plasma extinguishes. In order to avoid this effect, it is necessary to apply AC or pulsed power to the target since the surface ion charge is removed during the positive or neutral phase. The sputtering system used in this work is a Kurt J. Lesker Nano38 with a base pressure in the range of 10^{-5} mbar and it was used mainly for the deposition of $Ge_2Sb_2Te_5$.

- The physical vapour deposition (PVD) method for high throughput (HT) synthesis is a process that combines co-evaporation of pure elements from multiple sources on temperature controlled substrates with independently controlled source shutters in ultra high vacuum (UHV) condition [7]. This method was used extensively in this work and it is described in detail in Chapter 2.

A.2 X-Ray Diffraction

X-ray diffraction is a technique for the study of the fine structure of matter and it started in 1912 with von Laue's discovery that crystals diffract x-rays in a way that reveals their structure. Initially, x-ray diffraction was employed only for the determination of crystal structure while today this method is used to tackle many other problems such as chemical analysis and stress measurement, for the study of phase equilibria and the measurement of particle size, for the determination of the orientation of one crystal or the ensemble of orientations in a polycrystalline aggregate [89].

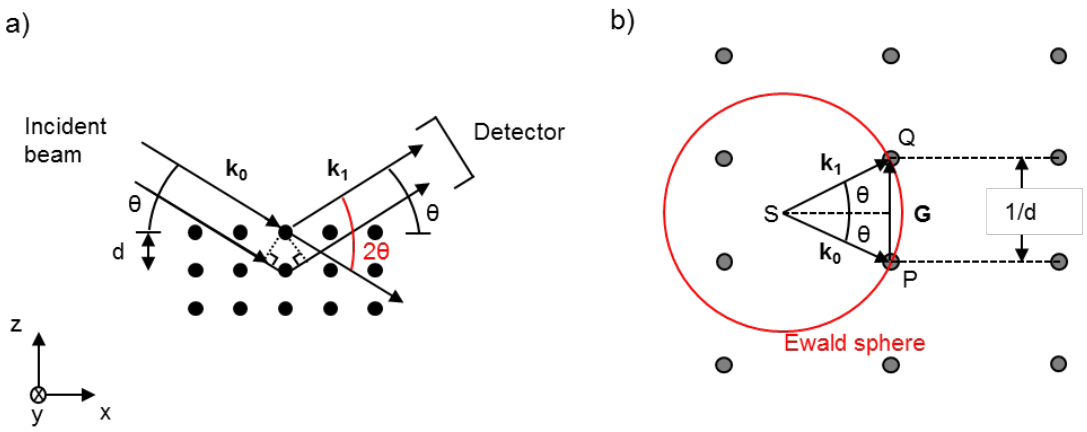

Figure A.1: Representation of diffraction from a stack of *xy* atomic planes in the real space a) and in the reciprocal space b) (adapted from [90]).

In Figure A.1a) it is represented the typical geometry of diffraction from a 3-dimensional lattice in the real space: the incident beam of x-rays characterized by a wavevector $\mathbf{k_0}$, wavelength λ and an angle of incidence θ hits the atoms producing a scattered beam with wavevector $\mathbf{k_0}$ in a process called elastic scattering ($|\mathbf{k_0}| = |\mathbf{k_1}| = \frac{1}{\lambda}$). A regular array of scatterers emits a regular array of spherical waves that interfere constructively only for specific directions given by the Bragg's law [90]:

$$2dsin\theta = n\lambda \qquad \text{(A1)}$$

Where *d* is the plane spacing and *n* is an integer number.

An alternative way to look at x-rays scattering is represented in Figure A.1b): this is the corresponding representation of Figure A.1a) in the reciprocal space. A stack of *xy* atomic planes spaced along *z* becomes a row of reciprocal-lattice points spaced along *z* with a periodicity of 1/*d* [90]. The Ewald sphere is a geometrical construction with radius equal to 1/λ; wherever this sphere intersects another reciprocal lattice point the Bragg's equation (A1) is satisfied and there will be a diffracted beam.

In XRD measurements the wavelength of the incident beam is usually fixed meaning that the radius of the Ewald sphere is constant. A polycrystalline thin film contains many crystallites in all possible orientations in absence of texturing effects (defined as the degree to which the crystallites in a polycrystalline film are similarly oriented [90]) and so the probability that many reciprocal lattice points coincide with the surface of the Ewald sphere is high (like in an ideal powder sample). Therefore, by moving the detector to the right positions, it is possible to detect the diffracted intensity. Nevertheless, texturing effects are very common in polycrystalline thin films and for this reason the sample is usually rotated along the *y* axis

(Figure A.1a)) together with the x-ray detector. This method is called 2θ or Bragg-Brentano scan [90].

A.3 Raman Spectroscopy

Raman scattering is a phenomenon observed when light is scattered by a medium that is constituted by molecules in vapour, liquid or solid phase. As opposed to other physical phenomena like spontaneous emission that is studied in fluorescence experiments, light scattering is omnidirectional, i.e. it can be observed in all directions independently of the direction of the incident radiation. In a typical experiment of scattering, the source is a monochromatic laser light at a specific frequency ν_L and the corresponding scattered light from the sample is measured at a frequency ν_S for a certain angle θ called scattering angle. The frequency of the incident radiation is chosen according with the experimental requirements and it can be in the near-UV, visible or near-IR. The measurement of the scattered light with an optical spectrometer reveals the presence of an elastic component ($\nu_L = \nu_S$) called Rayleigh scattering and inelastic components ($\nu_L \neq \nu_S$) called Raman scattering. By definition, the red-shifted components ($\nu_S < \nu_L$) are called Stokes components while the blue-shifted ones ($\nu_S > \nu_L$) are called anti-Stokes components.

The physical origin of Raman scattering is related to the excitation of molecular vibrations for gas and liquids and optical phonons for crystalline solids. The measured intensity of Raman scattering is usually plot as a function of the difference between the energy of the incident radiation and the energy of the scattered radiation ($h|\nu_L - \nu_s|$), because this quantity is independent of the excitation frequency and this energy difference is a distinctive feature of the vibrational mode (or optical phonon for solids) involved in the Raman scattering process. For this reason, Raman spectra are generally reported in Raman shift ($\Delta\tilde{\nu}$) defined in wavenumber as:

$$\Delta\tilde{\nu} = |\tilde{\nu}_L - \tilde{\nu}_S| = \left|\frac{1}{\lambda_L} - \frac{1}{\lambda_S}\right| \ (cm^{-1}) \qquad \text{(A2)}$$

The typical range of Raman spectra is between 10 cm^{-1} and 4000 cm^{-1}.

The process of Raman scattering in crystalline solids involves the interaction between the incident photons and the phonons of the crystal. Crystalline solids are characterized by a long-range order (translational order) that enables the definition of a crystalline lattice and so of a unit cell containing all the information about the structure and symmetries of the solid. The nuclear and electronic motions inside an atom can be separated by using the Born-Oppenheimer approximation and in a solid the atomic nuclei can only oscillates around an

equilibrium position. Therefore, the dynamic of these atomic nuclei can be described as collective oscillations of all the atoms (or molecules for molecular solids) included in the solid. Classically, these oscillations of the crystalline lattice are called normal modes of vibration and are characterized by a specific frequency at which all the atoms oscillate in phase. Moreover, the normal modes are independent from each other and so any possible lattice vibration can be expressed as a linear combination of normal modes. The analog of normal modes in quantum mechanics is a phonon and is defined as a collective excitation of the crystalline lattice. As all the quantum mechanical particles, also phonons have a particle and wave-like behaviour characterized by a certain energy *E* and linear momentum ***p***:

$$E = \hbar\omega \qquad \boldsymbol{p} = \hbar\boldsymbol{q} \tag{A3}$$

Where ω is the angular frequency and $\boldsymbol{q}$ is the wavevector of the phonon. In harmonic approximation, phonons are independent from each other.

Due to the translational periodicity of crystalline solids and the wave-like nature of phonons, it is useful to define a lattice in the reciprocal space (as described for XRD in the previous section) where the corresponding of the unit cell in the real space is called first Brillouin zone in the reciprocal space. Hence, the dispersion relationships can be obtained for phonons describing the dependence of the oscillation frequency of phonons as a function of the respective wavevector. Furthermore, these dispersion relationships or branches have the same periodicity of the crystal and so they can be studied inside only the first Brillouin zone. In a crystalline solids, the number of different branches are equal to 3σ where σ is the number of atoms in the primitive unit cell. In general, two class of branches exists: acoustic branches that are present in all solids and are characterized by a dispersion value of zero at the centre of the first Brillouin zone; and optical branches present only when at least two atoms are comprised in the primitive unit cell and are characterized by a dispersion value different from zero at the centre of the first Brillouin zone. The number of optical branches are equal to 3σ – 3 and are so named because these lattice vibrational waves can be excited with light of IR wavelengths, energies much higher than those of the acoustic branch, especially at the Brillouin zone centre [93]. For Raman spectroscopy of crystalline solids only the optical phonons can be detected, instead acoustic phonons are Raman inactive. This is probably the most important selection rule in Raman spectroscopy and its physical origin comes from the fact that the first Brillouin zone has a typical dimension of the order of 10^8 cm^{-1} (lattice constants of solids are of the order of 10^{-10} nm) while the wavevector of a visible photons is on the order of 10^5 cm^{-1} and since the energy and momentum must be conserved, only phonons at the centre of the first Brillouin zone can be excited in Raman scattering and only

optical phonons have a value different from zero at the zone centre. This restriction of sampling only those phonons near the Brillouin zone centre results in very narrow Raman peaks from crystalline solids [93]. Furthermore, other selection rules exist and so not all the optical phonons are Raman active (group theory can be used to predict which optical modes are Raman active).

Therefore, Raman spectroscopy gives information about the energy, lifetime and symmetry of only optical phonons at the centre of the Brillouin zone for Raman spectra of the first order. In fact, real nuclear potentials are not harmonic and so phonons can interact between each other and give rise to smaller peaks (in intensity) observed in the so-called Raman spectra of the second order. These peaks are important in order to obtain information about the density of the phononic states.

For amorphous solids, the absence of long-range order removes the Raman selection rule about the excitation of acoustic and optical phonons derived for crystalline solids [93]. Hence, all the phonons of the Brillouin zone become Raman active and the corresponding Raman spectrum is very broad, because it contains contributions from the full vibrational density of states [94].

A.4 Energy Dispersive X-Ray Spectroscopy

Energy dispersive x-ray spectroscopy (EDX) is a technique used for the determination of the chemical composition of a sample. A source of high energy electrons is focused on the sample and the incident beam can excite an electron in one of the inner shell of an atom inside the specimen. This electron is ejected from the atom and an electronic hole is created. Hence, an electron from the outer shells can fill this hole and the difference in energy between the higher-energy shell and the lower energy shell may be released in the form of an x-ray. In the EDX technique the intensity and the energy of the x-rays emitted in this process are measured; since the energy of these x-rays depends on the difference between two atomic shells and each atomic element has a unique energetic structure, it is possible to determine the chemical composition of the analysed material. Usually EDX is a tool of a SEM instrument as it provides a suitable electron source for this technique.

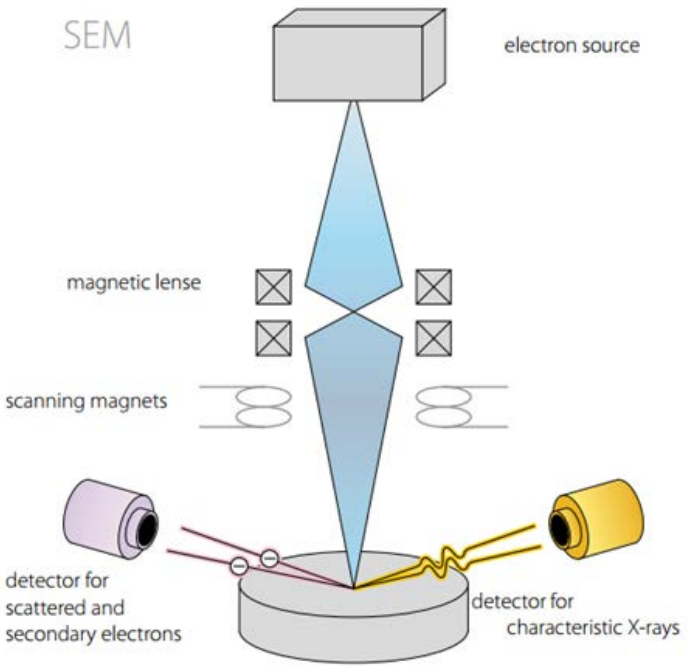

Figure A.2: Schematic of the principle of energy dispersive x-ray spectroscopy (EDX) in the scanning electron microscope (SEM).

Quantitative analysis of elements in any sample requires the measurements of the peak intensities; once these intensities have been determined, a comparison is made with standards of known composition and matrix corrections are applied in order to obtain the concentration of each element inside the analysed sample [120].

X-ray intensities are measured by counting photons and the precision obtainable is limited by statistical error. For heavier elements it is usually not difficult to obtain a precision better than ± 1%, but the overall analytical accuracy is commonly nearer ± 2%, owing to other factors such as uncertainties in the compositions of the standards and errors in the various corrections which need to be applied to the raw data. As well as producing characteristic x-ray lines, the bombarding electrons also give rise to a continuous x-ray spectrum which limits the detachability of small peaks, owing to the presence of background. Using routine procedures, detection limits are typically about 1000 ppm (by weight) but can be reduced by using long counting times.

A.5 Ellipsometry

Ellipsometry is typically a non-invasive and non-destructive optical technique by which the measured signal is the change in polarization of the incident light due to the interaction with the analysed sample. The polarization change depends on the material properties and on the

thickness of the layer, hence this technique can be used to characterize the optical properties, the surface roughness and the thickness of the sample.

A general representation of the processes involved in ellipsometry is illustrated in Figure A.3: a monochromatic plane wave light linearly polarized is directed at a surface at oblique incidence and the reflected light is detected. The plane of incidence is defined as a plane perpendicular to the sample's surface that contains the wavevector of the incident light. In general, the electric field can be described as a linear combination of a component parallel (*y* axes in Figure A.3) and perpendicular (*x* axes in Figure A.3) to the plane of incidence (*z* axes is the propagation direction):

$$\boldsymbol{E}(z,t) = E_x\hat{\boldsymbol{x}} + E_y\hat{\boldsymbol{y}} \tag{A4}$$

Where the components E_x and E_y can be written as a function of their amplitudes A_x and A_y:

$$\begin{aligned} E_x(z,t) &= A_x\cos(\omega t - kz + \phi_x) \\ E_y(z,t) &= A_y\cos(\omega t - kz + \phi_y) \end{aligned} \tag{A5}$$

The spatial and temporal dependencies can be omitted here, because the quantity of interest in ellipsometry is the polarization state [196]. Therefore, by using the Jones formalism, the electric field ***E*** can be written as:

$$\boldsymbol{E} = \begin{bmatrix} E_x \\ E_y \end{bmatrix} = \begin{bmatrix} A_x e^{i\phi_x} \\ A_y e^{i\phi_y} \end{bmatrix} \tag{A6}$$

And the relative phase difference ϕ is defined as:

$$\phi = \phi_y - \phi_x \tag{A7}$$

The physical quantities measured in ellipsometry are two angles ψ and Δ called ellipsometric parameters. In general, the reflected light in an ellipsometry measurement is elliptically polarized and by using the Jones formalism, a new quantity χ is defined as:

$$\boldsymbol{\chi} = \frac{E_y}{E_x} \tag{A8}$$

In Figure A.3 there is an incident electric field $\boldsymbol{E_i}$ (input) and a reflected field $\boldsymbol{E_o}$ (output). In order to obtain information on the properties of the sample, the term of interest is the ratio χ_i/χ_o:

$$\frac{\boldsymbol{\chi}_i}{\boldsymbol{\chi}_o} = \left(\frac{E_{y,i}}{E_{x,i}}\right) / \left(\frac{E_{y,o}}{E_{x,o}}\right) = \frac{E_{y,i}E_{x,o}}{E_{x,i}E_{y,o}} \tag{A9}$$

Using the Jones vectors defined in Eq. (A6), the precedent expression becomes:

$$\frac{\boldsymbol{\chi}_i}{\boldsymbol{\chi}_o} = \frac{A_{y,i}}{A_{x,i}} e^{i(\phi_{y,i}-\phi_{x,i})} \frac{A_{x,o}}{A_{y,o}} e^{i(\phi_{x,o}-\phi_{y,o})} \tag{A10}$$

If the incident light is linearly polarized with $\phi_i = 0$ and $A_{y,i} = A_{x,i}$, then:

$$\frac{\boldsymbol{\chi}_i}{\boldsymbol{\chi}_o} = \frac{A_{x,o}}{A_{y,o}} e^{i(\phi_{x,o}-\phi_{y,o})} \tag{A11}$$

This expression contains only contributions from the elliptically polarized reflected light. At this point, the ellipsometric parameters ψ and Δ can be defined as:

$$\begin{aligned} tan(\psi) &= \frac{A_{x,o}}{A_{y,o}} \\ \Delta &= \phi_{x,o} - \phi_{y,o} \end{aligned} \tag{A12}$$

Hence, the general ellipsometer equation is derived and can be written as [197]:

$$\frac{\boldsymbol{\chi}_i}{\boldsymbol{\chi}_o} = tan(\psi) e^{i\Delta} \tag{A13}$$

This expression can be related to the Fresnel reflection coefficient ρ of the sample that is defined as the ratio of the reflected wave's complex electric field amplitude to that of the incident wave. The reflected wave has in general two components, one parallel (*y* axes in Figure A.3) and one perpendicular (*x* axes in Figure A.3) to the plane of incidence:

$$\begin{aligned} \rho_y &= \frac{E_{y,o}}{E_{y,i}} \\ \rho_x &= \frac{E_{x,o}}{E_{x,i}} \end{aligned} \tag{A14}$$

Then, χ_i / χ_o can be written in terms of the Fresnel reflection coefficients ρ_x and ρ_y as:

$$\frac{\boldsymbol{\chi}_i}{\boldsymbol{\chi}_o} = \frac{E_{y,i} E_{x,o}}{E_{x,i} E_{y,o}} = \frac{\rho_y}{\rho_x} \tag{A15}$$

Therefore, the final expression is:

$$\frac{\rho_y}{\rho_x} = tan(\psi) e^{i\Delta} \tag{A16}$$

This expression correlates the ellipsometric parameters to the Fresnel reflection coefficients ρ_x and ρ_y and it enables the derivation of the refractive index of a material as a function of ψ and Δ. In fact, the data from an ellipsometer measurement are the values of ψ and Δ as function of wavelength; using Eq. (A16) these data can be used to calculate the complex refractive index as a function of wavelength (the Fresnel coefficient can be written as a

function of the complex refractive index of the materials that constitute the sample and the angle of incidence of the light) [196].

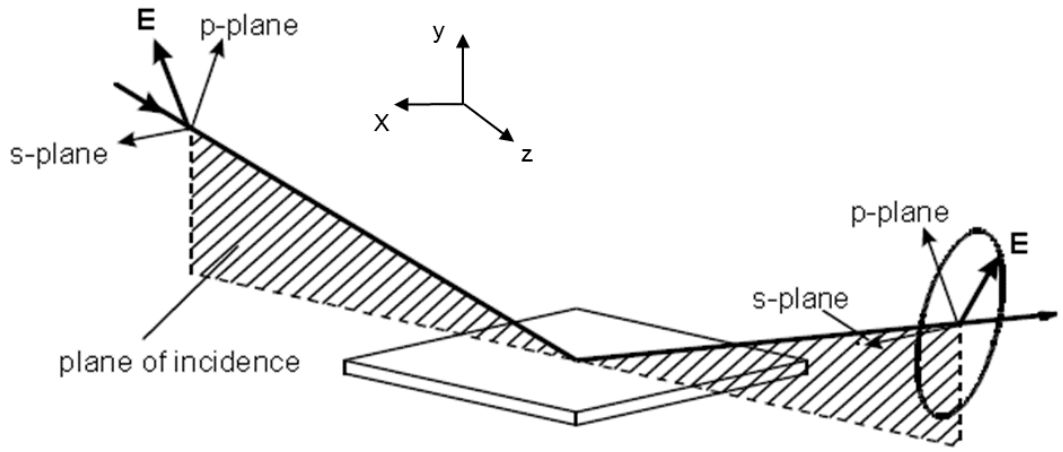

Figure A.3: The general principle in ellipsometry: interaction of polarized light with a sample (adapted from [198]).

The determination of properties such as the thickness and the refractive index of a thin film requires a model-based analysis of the data collected from ellipsometry. This analysis process can be summarized in three steps [198]:

- a layered optical model is built which represents the nominal structure of the sample. This model is used to calculate trial ellipsometry data for the nominal sample.
- The trial ellipsometry data are adjusted to improve the agreement with the measured ellipsometry data via a fitting procedure based on the definition of model fit parameters (these could be the thickness of the layers, the surface roughness, the optical constants of the layers, etc.)
- The results of the fit are evaluated; if the results are not acceptable, the optical model and/or the defined fit parameters are modified and the data is fit again.

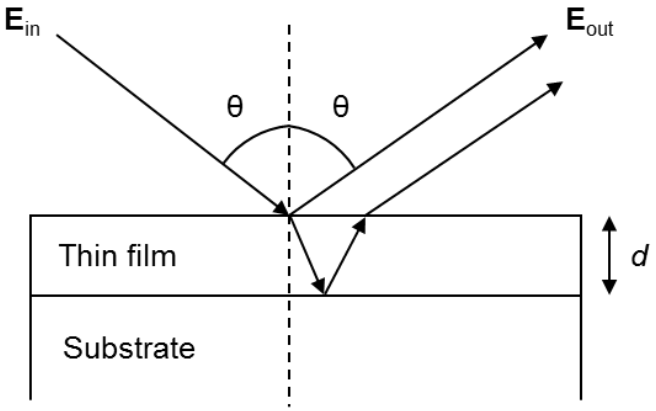

Figure A.4: Schematic representation of the interaction of light with a thin film sample on top of a substrate.

A.6 FIB Fabrication

The deposition of thin films is the first step toward the fabrication of metamaterials; the deposited layer must be patterned in a proper way to obtain a subwavelength response from it. For this task, a FIB milling system is employed. This uses a finely focused beam of ions (Ga ions in this case) to produce structure in the micro and nanoscale with a resolution of approximately 10 nm. The working principle is similar to a scanning electron microscope (SEM). In fact the ion beam is scanned over the sample surface in a raster scan pattern much like a SEM's electron beam. However, the ions remove atoms from specific sites, creating a desired pattern on the sample surface. The instrument used in this work is named "Dual Beam FIB", since in addition to the ion beam (FIB column), it is equipped also with an electron beam (SEM column) that allows imaging the sample surface without a sensible change of its structure. The two different beams emit from different directions with respect to the sample, forming an angle of 52° from each other. This instrument operates in high vacuum conditions, namely the pressure is of about 10^{-5} mbar. Moreover, the instrument is equipped with a gas injection system (GIS) and a moving sample holder (stage). The GIS allows the injection of a gas into the working chamber in a specified zone of the sample surface. The gas is formed by metal-organic molecules and the ion beam is used to dissociate these molecules so that the metal atoms are deposited on the surface in the area swept by the ion beam while the organic part is removed by the pumping system. This covers the sample surface with a layer made of a metal-Carbon-Ga mixture that has a shape and a thickness set by the user. The specimen is placed on a sample holder that can move along all three spatial directions and also provides both polar and azimuthal angular control with respect to the sample surface normal.

A.7 CRAIC Microspectrophotometer

The optical response of the samples is measured by using a UV/visible/near-IR CRAIC QDI2010 microspectrophotometer. A microspectrophotometer combines an optical microscope with a UV/visible/near-IR spectrophotometer. With this configuration, this instrument is able to measure samples on the order of μm^2 that is an essential feature for measuring planar metamaterials that have typical size of 20×20 µm.

This microspectrophotometer is a single-beam instrument and can be configured to measure transmittance and reflectance from the analysed sample (Figure A.5). In fact, it is equipped with two lamps, one for transmission and the other for reflection illumination of the sample; the light transmitted or reflected from the sample is collected from the objective lens of the microscope and focused on the spectrophotometer aperture. The spectrophotometer measures the intensity of light as a function of its wavelength via a diffraction grating that separates the light into its component wavelengths and the separated light is then focused onto a CCD (charge-coupled device) array detector where the intensity of each wavelength is measured by a pixel of the array.

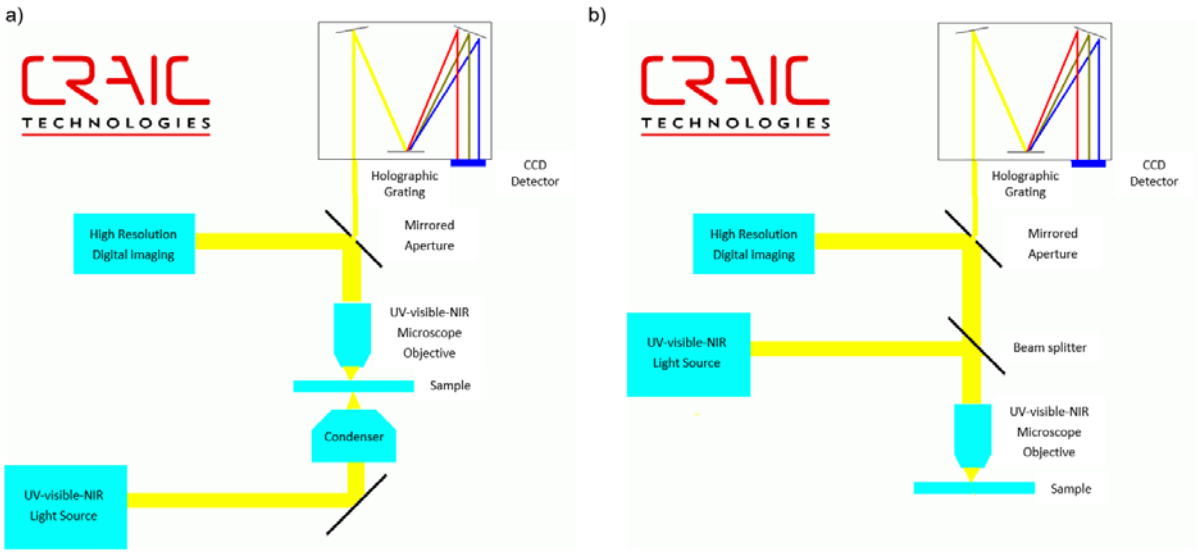

Figure A.5: General diagram of a microspectrophotometer in transmission a) and reflection mode b).

Transmission and reflection spectra are calculated from a sample and reference single-beam spectra:

$$T\% = \frac{S - D}{R - D} \times 100 \qquad \text{(A17)}$$

$$R\% = \frac{S - D}{R - D} \times 100$$

Where R is the single beam spectrum of the reference material, S is the single beam spectrum of the sample and D is the dark counts (electronic noise) of the system. For transmission mode, the reference material is air or the substrate where the thin film is deposited while for reflection mode the reference is a high-reflectivity mirror.

A.8 Computational tools: Comsol and Lumerical

The optical properties of photonic metamaterials were studied also by full wave numerical simulations. Numerical analysis tools are very useful for the design of metamaterials and also for obtaining a deeper insight into the electromagnetic modes excited in the nanostructures via the visualization of the corresponding electromagnetic field distribution.

In this work, numerical simulations were performed using two commercial software: Comsol Multiphysics 5.1 and Lumerical. Comsol is based on the finite element method (FEM) while Lumerical is based on the finite difference time domain (FDTD) method.

The finite element method is a numerical technique for obtaining approximate solutions to boundary-value problems in engineering and mathematical physics [199]. The principle of the method is to replace an entire continuous domain by a number of subdomains (a process called discretization) in which the unknown function is represented by interpolation functions with unknown coefficients. Then, a system of algebraic equations is obtained by applying some specific procedures and, by solving this system of equation, the solution of the initial problem is obtained [199].

The finite difference time domain method is a numerical technique for solving Maxwell's equations on a discrete spatial and temporal grid (or mesh). The principle of the method is to discretize the time dependent Maxwell's equations by replacing the space and time partial derivatives with the corresponding finite difference by using the central-difference approximation. Then, these finite difference equations are solved for the electric field vector components in a certain volume of space at a given instant in time; after that, the magnetic field vector components in the same spatial volume are solved at the next instant in time; and the process is repeated over and over again until the desired transient or steady-state electromagnetic field behaviour is fully evolved. One of the main advantage over the FEM techniques is that solutions in FDTD can cover a wide frequency range with a single simulation run, since it is a time-domain method. Instead, in FEM techniques the equations

are normally solved in the frequency domain, so the equations must be solved at each specific frequency in the range of interest.

Despite the fundamental difference between Comsol and Lumerical, the main steps involved in the modelling of photonic metamaterials are similar and can be summarized as:

- Definition of the geometrical structure; only the geometry of the unit cell needs to be defined explicitly due to the periodicity of planar metamaterials.
- Definition of the material properties; most of the optical constants used in this work were retrieved experimentally from ellipsometry and were employed in the numerical simulations.
- Definition of the boundary conditions; the planar periodicity of the studied metamaterials requires periodic boundary conditions for directions perpendicular to the propagation direction. Along the propagation direction, port boundary conditions are used in one side as the source of the incident plane wave and on the other side as the detector for the transmitted wave. Moreover, perfectly matched layers (PML) are generally used at the top and bottom boundaries along the propagation direction to attenuate the wave as it propagates in the direction perpendicular to the PML boundary.
- Definition of the mesh domains; the physical domain needs to be discretised and so a polygonal or polyhedral mesh is generated to approximate the geometric domains. For mesh parameters, the maximum element size in each domain should be one tenth of wavelength or smaller.
- Set the solver parameters and run the simulation.

Appendix B

BST Ternary Maps

In this section, XRD, Raman and ellipsometry data are mapped to the corresponding chemical composition in the ternary Bi:Sb:Te space.

B.1 XRD Maps

Here, we report intensity plot of the x-ray signal at a certain selected 2θ angle (in degrees) mapped to the corresponding chemical composition. These ternary plot show the intensity at the 2θ angle for the peaks observed in Figures 2.11, 2.12, 2.13 and 2.14.

This visualization technique enables the observation of the intensity data for all the spectra simultaneously, but at only one specific diffraction angle [56]. This visual method is useful because it allows the observation in a single image of the compositional range over which a specific peak is present at a particular angle and it allows to track the shift in the position of the peak as function of angle in the compositional space [56].

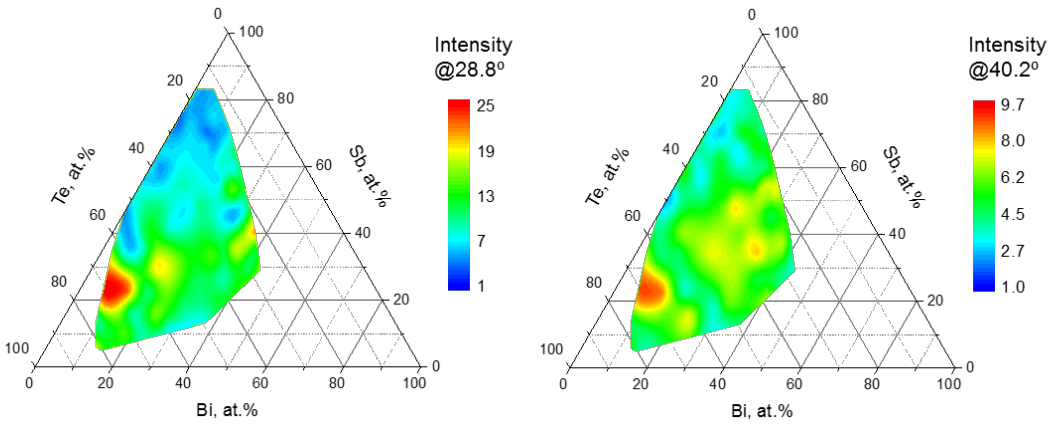

Figure B.1: Intensity plot of the x-ray signal at a certain selected 2θ angle (in degrees) mapped to the corresponding chemical composition. These ternary plot show the intensity at the 2θ angle for the peaks observed in Figure 2.13.

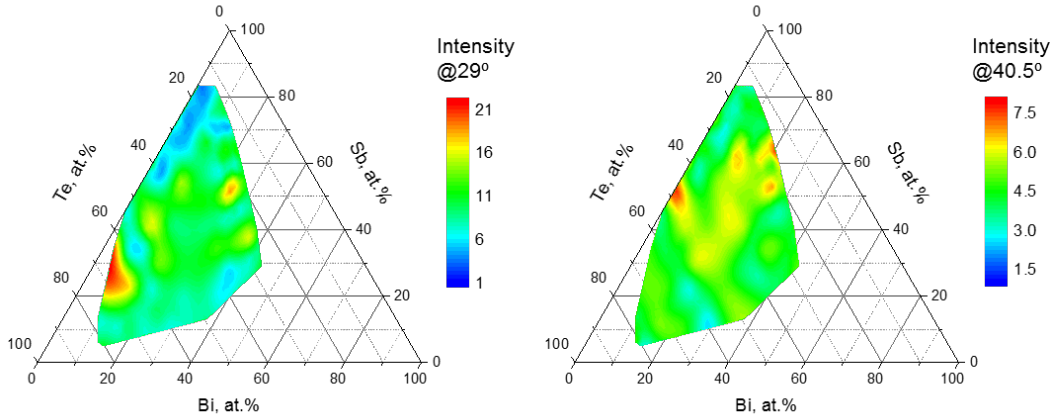

Figure B.2: Intensity plot of the x-ray signal at a certain selected 2θ angle (in degrees) mapped to the corresponding chemical composition. These ternary plot show the intensity at the 2θ angle for the peaks observed in Figure 2.15.

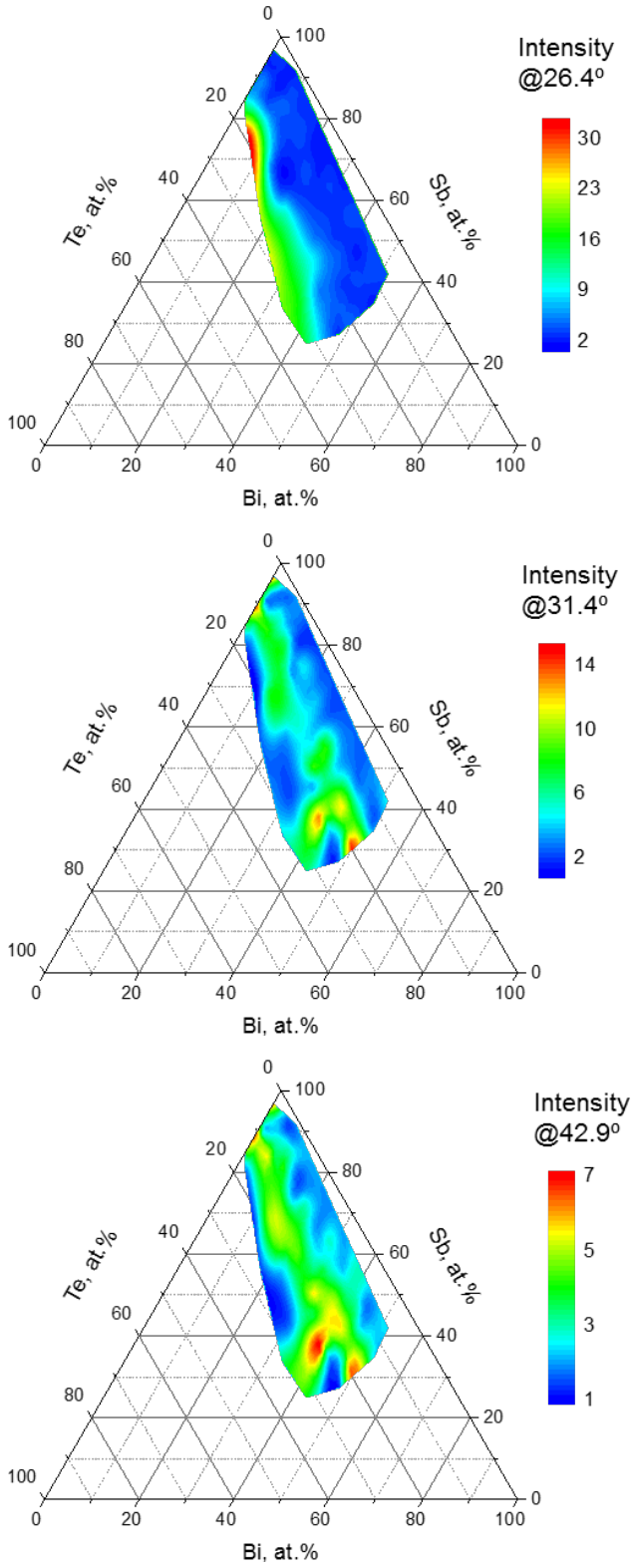

Figure B.3: Intensity plot of the x-ray signal at a certain selected 2θ angle (in degrees) mapped to the corresponding chemical composition. These ternary plot show the intensity at the 2θ angle for the peaks observed in Figure 2.12 and Figure 2.14.

B.2 Raman Maps

Here, we report intensity plot of the Raman signal at a certain selected Raman shift (in cm^{-1}) mapped to the corresponding chemical composition. These ternary plot show the intensity at the Raman shift for the peaks observed in Figures 2.11, 2.12, 2.13 and 2.14.

This visualization technique is similar to the one used in the previous section for XRD measurements and it enables the observation of the intensity data for all the spectra simultaneously at one specific value of the Raman shift. This visual method is useful because it allows the observation in a single image of the compositional range over which a specific peak is present at a particular Raman shift and it allows to track the shift in the position of the peak as function of the Raman shift in the compositional space.

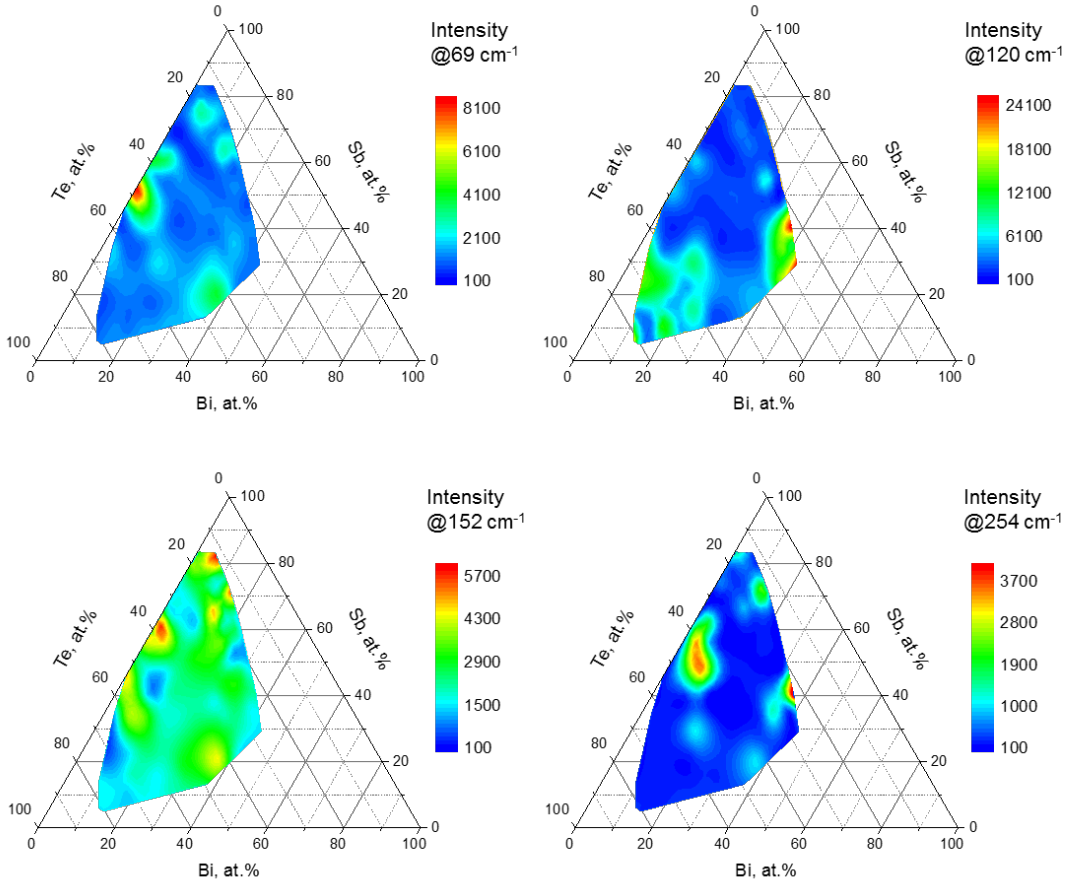

Figure B.4: Intensity plot of the Raman signal at a certain selected Raman shift (in cm^{-1}) mapped to the corresponding chemical composition. These ternary plot show the intensity at the Raman shift for the peaks observed in Figure 2.13.

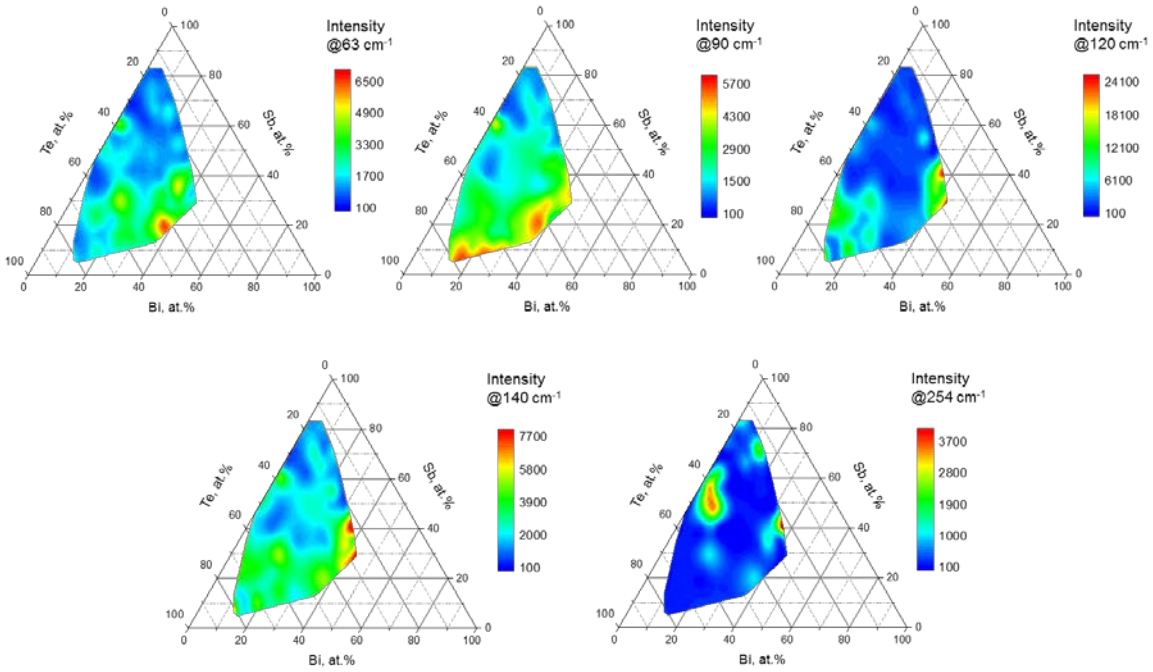

Figure B.5: Intensity plot of the Raman signal at a certain selected Raman shift (in cm^{-1}) mapped to the corresponding chemical composition. These ternary plot show the intensity at the Raman shift for the peaks observed in Figure 2.15.

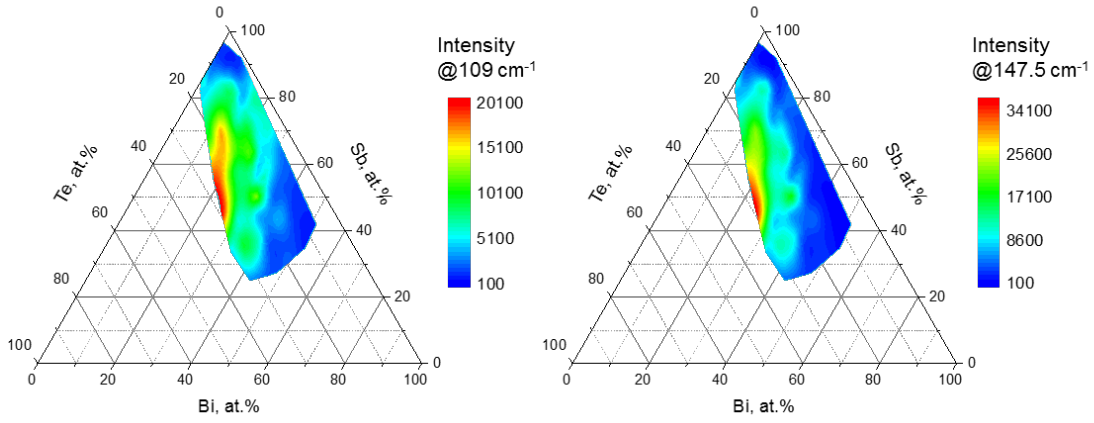

Figure B.6: Intensity plot of the Raman signal at a certain selected Raman shift (in cm^{-1}) mapped to the corresponding chemical composition. These ternary plot show the intensity at the Raman shift for the peaks observed in Figure 2.12 and Figure 2.14.

B.3 Optical Properties Maps

Here, we report the plasmonic and dielectric properties of BST mapped to the corresponding chemical composition for some specific wavelengths.

In Figure B.7 we plot the figure of merit for localized surface plasmon resonances (LSPR), defined as F_2 in Eq. (2.16), mapped to the corresponding chemical composition in the UV (253 nm and 350 nm), visible (550 nm) and near-IR (900 nm) spectral range.

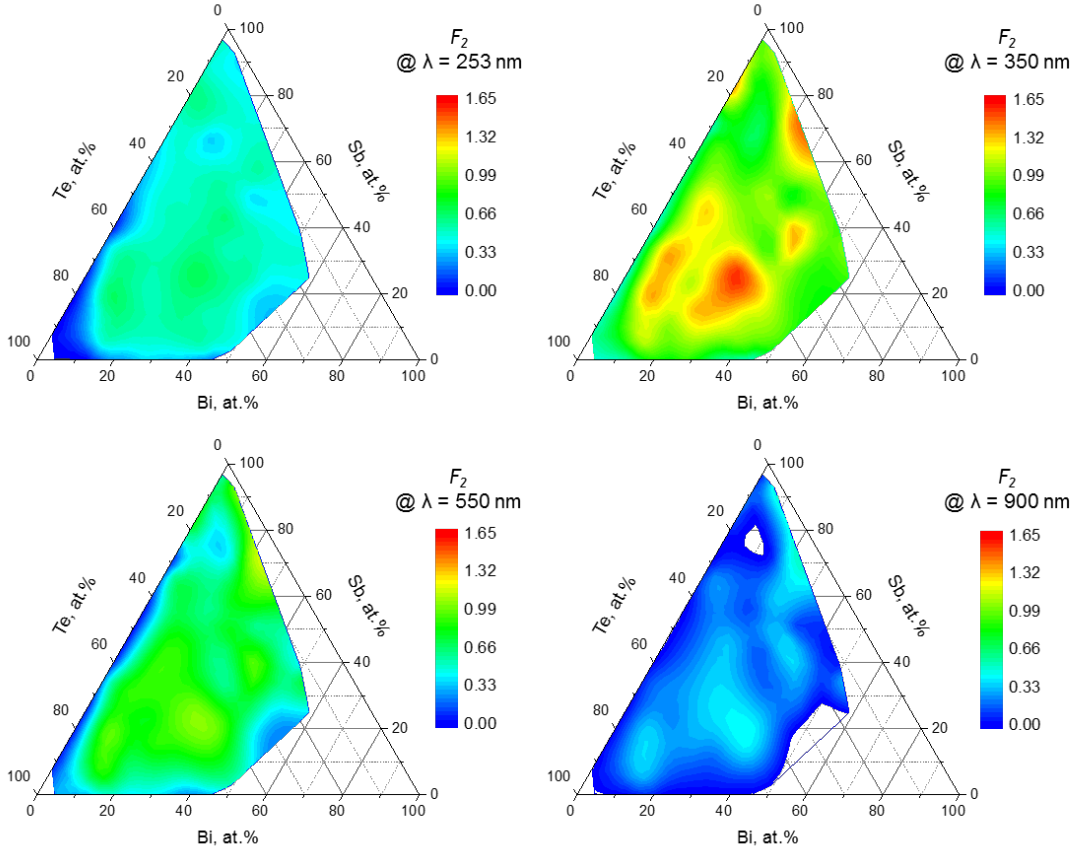

Figure B.7: Figure of merit for localized surface plasmon resonances (LSPR), defined as F_2 in Eq. (2.16), mapped to the corresponding chemical composition in the UV (253 nm and 350 nm), visible (550 nm) and near-IR (900 nm) spectral range.

In Figure B.8 we plot the figure of merit for low-loss propagating light waves, defined as F_3 in Eq. (2.17), mapped to the corresponding chemical composition at telecom wavelengths, i.e. 1310 nm (on the left) and 1550 nm (on the right).

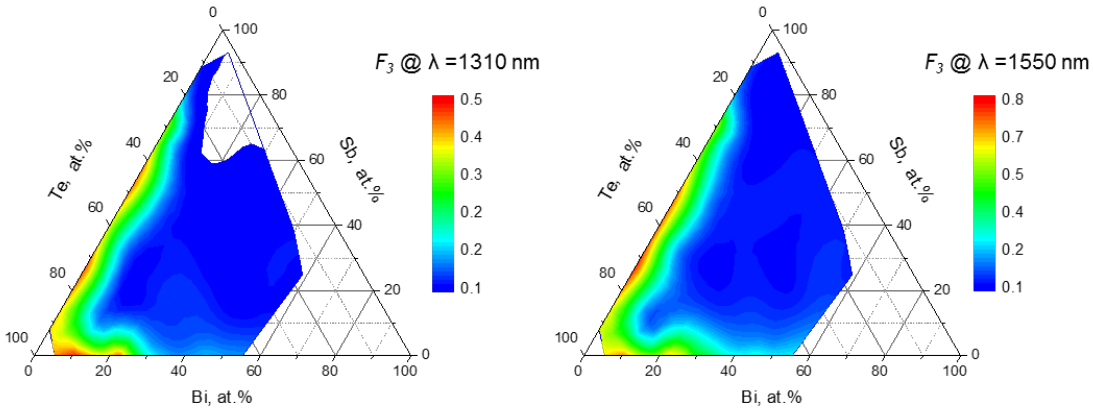

Figure B.8: Figure of merit for low-loss propagating light waves, defined as F_3 in Eq. (2.17), mapped to the corresponding chemical composition at telecom wavelengths, i.e. 1310 nm (on the left) and 1550 nm (on the right).

Bibliography

[1] R. M. Walser, "Electromagnetic metamaterials," in *International Symposium on Optical Science and Technology*, 2001, vol. 4467, p. 15: SPIE.

[2] J. W. Haus, *Fundamentals and Applications of Nanophotonics*. 2016, p. 426.

[3] P. Genevet, F. Capasso, F. Aieta, M. Khorasaninejad, and R. Devlin, "Recent advances in planar optics: from plasmonic to dielectric metasurfaces," *Optica,* vol. 4, 1, p. 139, 2017

[4] H. T. Chen, A. J. Taylor, and N. Yu, "A review of metasurfaces: physics and applications," *Reports on Progress in Physics,* vol. 79, 7, p. 076401, 2016

[5] X. Zhang and Z. W. Liu, "Superlenses to overcome the diffraction limit," *Nature Materials,* vol. 7, 6, pp. 435-441, 2008

[6] N. Yu and F. Capasso, "Flat optics with designer metasurfaces," *Nature Materials,* vol. 13, p. 139, 2014

[7] P. Chaturvedi, "Optical Metamaterials: Design, Characterization and Applications," Doctor of Philosophy, University of Illinois, 2009.

[8] C. M. Soukoulis and M. Wegener, "Past achievements and future challenges in the development of three-dimensional photonic metamaterials," *Nature Photonics,* vol. 5, 9, pp. 523-530, 2011

[9] D. R. Smith, J. B. Pendry, and M. C. K. Wiltshire, "Metamaterials and negative refractive index," *Science,* vol. 305, 5685, pp. 788-792, 2004

[10] H. T. Chen, W. J. Padilla, J. M. O. Zide, A. C. Gossard, A. J. Taylor, and R. D. Averitt, "Active terahertz metamaterial devices," *Nature,* vol. 444, 7119, pp. 597-600, 2006

[11] W. Li *et al.*, "Refractory Plasmonics with Titanium Nitride: Broadband Metamaterial Absorber," *Advanced materials,* vol. 26, 47, p. 7959, 2014

[12] Y. Yang, I. I. Kravchenko, D. P. Briggs, and J. Valentine, "All-dielectric metasurface analogue of electromagnetically induced transparency," *Nature Communications,* vol. 5, p. 5753, 2014

[13] N. I. Zheludev, "Obtaining optical properties on demand," *Science,* vol. 348, pp. 973-974, 2015

[14] N. I. Zheludev and Y. S. Kivshar, "From metamaterials to metadevices," *Nature Materials,* vol. 11, 11, pp. 917-24, 2012

[15] A. Y. Zhu, A. I. Kuznetsov, B. Luk'yanchuk, N. Engheta, and P. Genevet, "Traditional and emerging materials for optical metasurfaces," *Nanophotonics,* vol. 6, 2, pp. 452–471, 2017

[16] J. B. Khurgin, "How to deal with the loss in plasmonics and metamaterials," *Nature Nanotechnology,* vol. 10, 1, pp. 2-6, 2015

[17] J. B. Khurgin and G. Sun, "In search of the elusive lossless metal," *Applied Physics Letters,* vol. 96, 18, 2010

[18] G. V. Naik, J. Kim, and A. Boltasseva, "Oxides and nitrides as alternative plasmonic materials in the optical range," *Optical Materials Express,* vol. 1, 6, pp. 1090-1099, 2011

[19] Y. K. Srivastava *et al.*, "A Superconducting Dual-Channel Photonic Switch," *Advanced Materials,* vol. 30, 29, p. 1801257, 2018

[20] N. Dabidian *et al.*, "Electrical Switching of Infrared Light Using Graphene Integration with Plasmonic Fano Resonant Metasurfaces," *ACS Photonics,* vol. 2, 2015

[21] M. I. Stockman *et al.*, "Roadmap on plasmonics," *Journal of Optics,* vol. 20, 4, p. 043001, 2018

[22] Q. Wang *et al.*, "Optically reconfigurable metasurfaces and photonic devices based on phase change materials," *Nature Photonics,* vol. 10, 1, pp. 60-U75, 2016

[23] D. R. Smith, D. C. Vier, T. Koschny, and C. M. Soukoulis, "Electromagnetic parameter retrieval from inhomogeneous metamaterials," *Physical Review E,* vol. 71, p. 036617, 2005

[24] R. A. Shelby, D. R. Smith, and S. Schultz, "Experimental verification of a negative index of refraction," *Science,* vol. 292, 5514, pp. 77-79, 2001

[25] L. Min and L. Huang, "Perspective on resonances of metamaterials," *Optics Express,* vol. 23, p. 19022, 2015

[26] W. Cai and V. Shalaev, *Optical Metamaterials*. New York: Springer Science+Business Media, 2010.

[27] P. R. West, S. Ishii, G. V. Naik, N. K. Emani, V. M. Shalaev, and A. Boltasseva, "Searching for better plasmonic materials," *Laser & Photonics Reviews,* vol. 4, 6, pp. 795-808, 2010

[28] A. Sobhani *et al.*, "Narrowband photodetection in the near-infrared with a plasmon-induced hot electron device.," *Nature communications,* vol. 4, 2013

[29] J. Zhang, "Controlling light with photonic metamaterials," Doctor of Philosophy, Optoelectronics Research Centre, University of Southampton, 2013.

[30] N. Papasimakis, "Trapped-modes, Slow Light and Collective Resonances in Metamaterials," Doctor of Philosophy, Optoelectronics Research Centre, University of Southampton, 2009.

[31] V. Fedotov, M. Rose, S. Prosvirnin, N. Papasimakis, and N. Zheludev, "Sharp Trapped-Mode Resonances in Planar Metamaterials with a Broken Structural Symmetry," *Physical Review Letters,* vol. 99, 2007

[32] A. Boltasseva and H. A. Atwater, "Low-Loss Plasmonic Metamaterials," in *Science* vol. 331, ed, 2011, pp. 290-291.

[33] J. Ou, J. So, G. Adamo, A. Sulaev, L. Wang, and N. I. Zheludev, "Ultraviolet and visible range plasmonics of a topological insulator," *Nature communications,* vol. 5, 5139, p. 5139, 2014

[34] J. Yin *et al.*, "Plasmonics of topological insulators at optical frequencies," *NPG Asia Materials,* vol. 9, 8, p. e425, 2017

[35] S. Jahani and Z. Jacob, "All-dielectric metamaterials," *Nature Nanotechnology,* vol. 11, pp. 23-36, 2016

[36] A. Krasnok, S. Makarov, M. Petrov, R. Savelev, P. Belov, and Y. Kivshar, "Towards all-dielectric metamaterials and nanophotonics," in *10th SPIE Conference on Metamaterials*, Prague, CZECH REPUBLIC, 2015, vol. 9502, p. 950203: Spie-Int Soc Optical Engineering.

[37] Q. Zhao, J. Zhou, F. Zhang, and D. Lippens, "Mie resonance-based dielectric metamaterials," *Materials Today,* vol. 12, pp. 60-69, 2009

[38] J. Zhang, K. F. MacDonald, and N. I. Zheludev, "Near-infrared trapped mode magnetic resonance in an all-dielectric metamaterial," *Optics Express,* vol. 21, pp. 26721-26728, 2013

[39] L. Y. Cao, J. S. White, J. S. Park, J. A. Schuller, B. M. Clemens, and M. L. Brongersma, "Engineering light absorption in semiconductor nanowire devices," *Nature Materials,* vol. 8, 8, pp. 643-647, 2009

[40] J. C. Ginn *et al.*, "Realizing Optical Magnetism from Dielectric Metamaterials," *Physical Review Letters,* vol. 108, 2012

[41] R. C. Devlin, M. Khorasaninejad, W. T. Chen, J. Oh, and F. Capasso, "Broadband high-efficiency dielectric metasurfaces for the visible spectrum," *Proceedings of the National Academy of Sciences of the United States of America,* vol. 113, 38, pp. 10473-10478, 2016

[42] M. Khorasaninejad *et al.*, "Polarization-Insensitive Metalenses at Visible Wavelengths," *Nano Letters,* vol. 16, 11, pp. 7229-7234, 2016

[43] M. Khorasaninejad *et al.*, "Achromatic Metalens over 60 nm Bandwidth in the Visible and Metalens with Reverse Chromatic Dispersion," *Nano Letters,* vol. 17, 3, pp. 1819-1824, 2017

[44] M. Khorasaninejad, W. T. Chen, R. C. Devlin, J. Oh, A. Y. Zhu, and F. Capasso, "Metalenses at visible wavelengths: Diffraction-limited focusing and subwavelength resolution imaging," *Science,* vol. 352, 6290, pp. 1190-1194, 2016

[45] S. M. Choudhury *et al.*, "Material platforms for optical metasurfaces," *Nanophotonics,* vol. 7, 6, pp. 959-987, 2018

[46] S. Guerin, B. Hayden, D. W. Hewak, and C. Vian, "Synthesis and Screening of Phase Change Chalcogenide Thin Film Materials for Data Storage," *ACS Combinatorial Science,* vol. 19, 7, pp. 478-491, 2017

[47] S. Guerin and B. E. Hayden, "Physical vapor deposition method for the high-throughput synthesis of solid-state material libraries," *Journal of Combinatorial Chemistry,* vol. 8, 1, pp. 66-73, 2006

[48] B. J. Eggleton, B. Luther-Davies, and K. Richardson, "Chalcogenide photonics," *Nature Photonics,* vol. 5, 3, pp. 141-148, 2011

[49] A. Zakery and S. R. Elliott, "Optical properties and applications of chalcogenide glasses: a review," *Journal of Non-Crystalline Solids,* vol. 330, 1-3, pp. 1-12, 2003

[50] M. Popescu, "Disordered chalcogenide optoelectronic materials: phenomena and applications," *Journal of Optoelectronics and Advanced Materials,* vol. 7, 4, pp. 2189-2210, 2005

[51] M. Popescu, "Chalcogenides – Past, present, future," *Journal of Non-Crystalline Solids,* vol. 352, 9-20, pp. 887-891, 2006

[52] R. E. Simpson, "Chalcogenide thin film materials for next generation data storage," Doctor of Philosophy, Optoelectronics Research Centre, University of Southampton, 2008.

[53] J. Dresner and G. B. Stringfellow, "Electronic processes in the photo-crystallization of vitreous selenium," *Journal of Physics and Chemistry of Solids,* vol. 29, 2, pp. 303-311, 1968

[54] A. V. Kolobov and S. R. Elliott, "Reversible photo-amorphization of crystalline films of As50Se50," *Journal of Non-Crystalline Solids,* vol. 189, 3, pp. 297-300, 1995

[55] K. Tanaka, "Configurational and Structural Models for Photodarkening in Glassy Chalcogenides," *Japanese Journal of Applied Physics,* vol. 25, Part 1, No. 6, pp. 779-786, 1986

[56] H. Hamanaka, K. Tanaka, A. Matsuda, and S. Iizima, "Reversible photo-induced volume changes in evaporated As2S3 and As4Se5Ge1 films," *Solid State Communications,* vol. 19, 6, pp. 499-501, 1976

[57] M. Janai and P. S. Rudman, "The kinetics of the light-enhanced vaporization of amorphous As2S3 thin films," *Physica Status Solidi (a),* vol. 42, 2, pp. 729-737, 1977

[58] G. Kluge, "A new interpretation of the photodoping effect in amorphous As- and Ge-chalcogenides," *Physica Status Solidi (a),* vol. 101, 1, pp. 105-114, 1987

[59] J. P. De Neufville, S. C. Moss, and S. R. Ovshinsky, "Photostructural transformations in amorphous As2Se3 and As2S3 films," *Journal of Non-Crystalline Solids,* vol. 13, 2, pp. 191-223, 1974

[60] F. Weigert, "Über die spezifische Wirkung der polarisierten Strahlung," *Annalen der Physik,* vol. 368, 24, pp. 681-725, 1920

[61] J. M. Lee, PhD, North Carolina State University, 1990.

[62] S. Raoux, "Phase Change Materials," *Annual Review of Materials Research,* vol. 39, 1, pp. 25-48, 2009

[63] M. Wuttig and N. Yamada, "Phase-change materials for rewriteable data storage," *Nature Materials,* vol. 6, 11, pp. 824-832, 2007

[64] E. Yablonovitch, "A light read," *Materials Today,* vol. 7, 3, p. 49, 2004

[65] K. F. MacDonald and N. I. Zheludev, "Active plasmonics: current status," *Laser & Photonics Reviews,* vol. 4, 4, pp. 562-567, 2009

[66] A. Karvounis, B. Gholipour, K. F. MacDonald, and N. I. Zheludev, "All-dielectric phase-change reconfigurable metasurface," *Applied Physics Letters,* vol. 109, 5, p. 051103, 2016

[67] Z. L. Samson *et al.*, "Metamaterial electro-optic switch of nanoscale thickness," *Applied Physics Letters,* vol. 96, 14, p. 143105, 2010

[68] B. Gholipour, J. F. Zhang, K. F. MacDonald, D. W. Hewak, and N. I. Zheludev, "An All-Optical, Non-volatile, Bidirectional, Phase-Change Meta-Switch," *Advanced Materials,* vol. 25, 22, pp. 3050-3054, 2013

[69] A. K. U. Michel *et al.*, "Using Low-Loss Phase-Change Materials for Mid-Infrared Antenna Resonance Tuning," *Nano Letters,* vol. 13, 8, pp. 3470-3475, 2013

[70] M. Rudé, R. E. Simpson, R. Quidant, V. Pruneri, and J. Renger, "Active Control of Surface Plasmon Waveguides with a Phase Change Material," *ACS Photonics,* vol. 2, 6, pp. 669-674, 2015

[71] X. Yin *et al.*, "Active Chiral Plasmonics," *Nano Letters,* vol. 15, 7, pp. 4255-60, 2015

[72] A. Tittl *et al.*, "A Switchable Mid-Infrared Plasmonic Perfect Absorber with Multispectral Thermal Imaging Capability," *Advanced Materials,* vol. 27, 31, pp. 4597-4603, 2015

[73] M. Rudé *et al.*, "Ultrafast and Broadband Tuning of Resonant Optical Nanostructures Using Phase-Change Materials," *Advanced Optical Materials,* vol. 4, 7, pp. 1060-1066, 2016

[74] D. Piccinotti, B. Gholipour, J. Yao, K. F. Macdonald, B. E. Hayden, and N. I. Zheludev, "Combinatorial search for plasmonic and epsilon-near-zero chalcogenide alloys," presented at the 2017 Conference on Lasers and Electro-Optics Europe & European Quantum Electronics Conference (CLEO/Europe-EQEC), 2017/06, 2017. Available: http://dx.doi.org/10.1109/cleoe-eqec.2017.8086613

[75] D. R. Smith, W. J. Padilla, D. C. Vier, S. C. Nemat-Nasser, and S. Schultz, "Composite Medium with Simultaneously Negative Permeability and Permittivity," *Physical Review Letters,* vol. 84, 18, pp. 4184-4187, 2000

[76] W. F. Maier, "The combinatorial approach," *Materials Today,* vol. 7, 10, pp. 55-56, 2004

[77] H. Koinuma and I. Takeuchi, "Combinatorial solid-state chemistry of inorganic materials," *Nature Materials,* vol. 3, p. 429, 2004

[78] X. D. Xiang *et al.*, "A combinatorial approach to materials discovery," *Science,* vol. 268, p. 1738, 1995

[79] E. J. Amis, "Combinatorial material science: reaching beyond discovery," *Nature Materials,* vol. 3, p. 83, 2004

[80] B. Luk'yanchuk *et al.*, "The Fano resonance in plasmonic nanostructures and metamaterials.," *Nature materials,* vol. 9, pp. 707-715, 2010

[81] E. Plum, K. Tanaka, W. T. Chen, V. a. Fedotov, D. P. Tsai, and N. I. Zheludev, "A combinatorial approach to metamaterials discovery," *Journal of Optics,* vol. 13, p. 055102, 2011

[82] I. Takeuchi *et al.*, "Data management and visualization of x-ray diffraction spectra from thin film ternary composition spreads," *Review of Scientific Instruments,* vol. 76, 6, 2005

[83] J. Zhang *et al.*, "Band structure engineering in $(Bi_{1-x}Sb_x)_2Te_3$ ternary topological insulators," *Nature Communications,* vol. 2, p. 574, 2011

[84] V. B. Ufimtsev, V. B. Osvensky, V. T. Bublik, T. B. Sagalova, and O. E. Jouravlev, "Structure, homogeneity and properties of thermoelectric materials based on ternary solid solutions of bismuth and antimony chalcogenides," *Adv. Perform. Mater.,* vol. 4, 2, pp. 189-197, 1997

[85] L. Xue-Dong and Y.-H. Park, "Structure and Transport Properties of $(Bi_{1-x}Sb_x)_2Te_3$ Thermoelectric Materials Prepared by Mechanical Alloying and Pulse Discharge Sintering," *Materials Transactions,* vol. 43, 4, pp. 681-687, 2002

[86] W. S. Whitney *et al.*, "Gate-Variable Mid-Infrared Optical Transitions in a $(Bi_{1-x}Sb_x)_2Te_3$ Topological Insulator," *Nano Letters,* vol. 17, 1, pp. 255-260, 2017

[87] F. Wooten, *Optical Properties of Solids* (Optical Properties of Solids). Academic Press, 1972, pp. 42 - 52.

[88] H. Ibach and H. Luth, *Solid-State Physics*, Fourth ed. Springer, 2009.

[89] B. D. Cullity, *Elements of X-Ray Diffraction*. Addison-Wesley Publishing Company, Inc., 1956.

[90] D. L. Smith, *Thin-Film Deposition: Principles and Practice*. McGraw-Hill Education, 1995.

[91] W. Richter, H. Kohler, and C. R. Becker, "A Raman and Far-Infrared Investigation of Phonons in the Rhombohedra1 V2-V13 Compounds Bi2Te3, Bi2Se3, Sb2Te3 and Bi2(Te1-xSex)3 (0 < x < l), (BilySb1-y)2Te3 (0 < y < 1)," *Physica Status solidi (b),* vol. 84, 2, pp. 619-628, 1977

[92] W. Liu, L. Endicott, V. A. Stoica, H. Chi, R. Clarke, and C. Uher, "High-quality ultra-flat $BiSbTe_3$ films grown by MBE," *Journal of Crystal Growth,* vol. 410, pp. 23-29, 2015

[93] D. Tuschel, "Why are the Raman spectra of crystalline and amorphous solids different?," *Spectroscopy,* vol. 32, 3, pp. 26-33, 2017

[94] R. Zallen, *The Physics of Amorphous Solids*. Wiley-VCH, 2007.

[95] O. Degtyareva, V. V. Struzhkin, and R. J. Hemley, "High-pressure Raman spectroscopy of antimony: As-type, incommensurate host-guest, and bcc phases," *Solid State Communications,* vol. 141, 3, pp. 164-167, 2007

[96] J. S. Lannin, J. M. Calleja, and M. Cardona, "Second-order Raman scattering in the group-Vbsemimetals: Bi, Sb, and As," *Physical Review B,* vol. 12, 2, pp. 585-593, 1975

[97] J. Secor, M. A. Harris, L. Zhao, H. Deng, S. Raoux, and L. Krusin-Elbaum, "Phonon renormalization and Raman spectral evolution through amorphous to crystalline transitions in Sb2Te3 thin films," *Applied Physics Letters,* vol. 104, 22, 2014

[98] R. N. Zitter and P. C. Watson, "Raman and x-ray spectra of single-crystal Bi-Sb alloys," *Physical Review B,* vol. 10, 2, pp. 607-611, 1974

[99] A. S. Pine and G. Dresselhaus, "Raman Spectra and Lattice Dynamics of Tellurium," *Physical Review B,* vol. 4, 2, pp. 356-371, 1971

[100] L. N. Luk'yanova *et al.*, "Surface morphology and Raman spectroscopy of thin layers of antimony and bismuth chalcogenides," *Physics of the Solid State,* vol. 58, 7, pp. 1440-1447, 2016

[101] J. Humlíček *et al.*, "Raman and interband optical spectra of epitaxial layers of the topological insulators Bi_2Te_3 and Bi_2Se_3 on BaF_2 substrates," *Physica Scripta,* vol. T162, p. 014007, 2014

[102] G. C. Sosso, S. Caravati, and M. Bernasconi, "Vibrational properties of crystalline Sb(2)Te(3) from first principles," *Journal of Physics: Condensed Matter,* vol. 21, 9, p. 095410, 2009

[103] X. Wang, K. Kunc, I. Loa, U. Schwarz, and K. Syassen, "Effect of pressure on the Raman modes of antimony," *Physical Review B,* vol. 74, 13, 2006

[104] V. Russo *et al.*, "Raman spectroscopy of Bi-Te thin films," *Journal of Raman Spectroscopy,* vol. 39, 2, pp. 205-210, 2008

[105] J. Toudert and R. Serna, "Interband transitions in semi-metals, semiconductors, and topological insulators: a new driving force for plasmonics and nanophotonics [Invited]," *Optical Materials Express,* vol. 7, 7, pp. 2299-2325, 2017

[106] B. Dastmalchi, P. Tassin, T. Koschny, and C. M. Soukoulis, "A New Perspective on Plasmonics: Confinement and Propagation Length of Surface Plasmons for Different Materials and Geometries," *Advanced Optical Materials,* vol. 4, 1, pp. 177-184, 2016

[107] P. B. Johnson and R. W. Christy, "Optical Constants of the Noble Metals," *Physical Review B,* vol. 6, 12, pp. 4370-4379, 1972

[108] W. S. M. Werner, K. Glantschnig, and C. Ambrosch-Draxl, "Optical Constants and Inelastic Electron-Scattering Data for 17 Elemental Metals," *Journal of Physical and Chemical Reference Data,* vol. 38, 4, pp. 1013-1092, 2009

[109] K. M. McPeak *et al.*, "Plasmonic Films Can Easily Be Better: Rules and Recipes," *ACS Photonics,* vol. 2, 3, pp. 326-333, 2015

[110] G. V. Naik, J. L. Schroeder, X. Ni, A. V. Kildishev, T. D. Sands, and A. Boltasseva, "Titanium nitride as a plasmonic material for visible and near-infrared wavelengths," *Optical Materials Express,* vol. 2, 4, pp. 478-489, 2012

[111] G. V. Naik, V. M. Shalaev, and A. Boltasseva, "Alternative Plasmonic Materials: Beyond Gold and Silver," *Advanced Materials,* vol. 25, 24, pp. 3264-3294, 2013

[112] D. E. Aspnes and A. A. Studna, "Dielectric functions and optical parameters of Si, Ge, GaP, GaAs, GaSb, InP, InAs, and InSb from 1.5 to 6.0 eV," *Physical Review B,* vol. 27, pp. 985-1009, 1983

[113] Z. Han and S. I. Bozhevolnyi, "Radiation guiding with surface plasmon polaritons," *Reports on Progress in Physics,* vol. 76, 1, p. 016402, 2012

[114] B.-L. Huang and M. Kaviany, "Ab initio and molecular dynamics predictions for electron and phonon transport in bismuth telluride," *Physical Review B,* vol. 77, pp. 1-19, 2008

[115] D. Hsieh *et al.*, "Observation of time-reversal-protected single-dirac-cone topological-insulator states in Bi_2Te_3 and Sb_2Te_3," *Physical Review Letters,* vol. 103, 14, p. 146401, 2009

[116] M. Zhao *et al.*, "Actively Tunable Visible Surface Plasmons in Bi2Te3and their Energy-Harvesting Applications," *Advanced Materials,* vol. 28, 16, pp. 3138-3144, 2016

[117] S. J. Kim, P. Fan, J.-H. Kang, and M. L. Brongersma, "Creating semiconductor metafilms with designer absorption spectra," *Nature Communications,* vol. 6, p. 7591, 2015

[118] B. Gholipour *et al.*, "Organometallic Perovskite Metasurfaces," *Advanced Materials,* vol. 29, 9, p. 1604268, 2017

[119] L. T. Cam Tuyen, P. H. Le, C. W. Luo, and J. Leu, "Thermoelectric properties of nanocrystalline Bi3Se2Te thin films grown using pulsed laser deposition," *Journal of Alloys and Compounds,* vol. 673, pp. 107-114, 2016

[120] Z. Wang *et al.*, "Effect of Annealing on the Properties of Antimony Telluride Thin Films and Their Applications in CdTe Solar Cells," *International Journal of Photoenergy,* vol. 2014, pp. 1-6, 2014

[121] M. Wuttig, H. Bhaskaran, and T. Taubner, "Phase-change materials for non-volatile photonic applications," *Nature Photonics,* vol. 11, 8, pp. 465-476, 2017

[122] S. Lee, K. Esfarjani, T. F. Luo, J. W. Zhou, Z. T. Tian, and G. Chen, "Resonant bonding leads to low lattice thermal conductivity," *Nature Communications,* vol. 5, p. 8, 2014

[123] N. Han *et al.*, "Phase-Change Memory in Bi_2Te_3 Nanowires," *Advanced Materials,* vol. 23, 16, p. 1871, 2011

[124] H. W. Ho *et al.*, "Optical response characteristics arising from delocalized electrons in phase change materials," *Acta Materialia,* vol. 61, 5, pp. 1757-1763, 2013

[125] L. S. Faraji, R. P. Singh, and M. Allahkarami, "Pulsed laser deposition of bismuth telluride thin film and annealing effects," *The European Physical Journal Applied Physics,* vol. 46, 2, p. 20501, 2009

[126] S. J. Jeon *et al.*, "Microstructure Evolution of Sputtered Bi-Te Films during Post-Annealing: Phase Transformation and Its Effects on the Thermoelectric Properties," *J. Electrochem. Soc.,* vol. 158, 8, pp. H808-H813, 2011

[127] H. J. Lee, S. Hyun, H. S. Park, and S. W. Han, "Thermoelectric properties of n-type Bi–Te thin films with various compositions," *Microelectronic Engineering,* vol. 88, 5, pp. 593-596, 2011

[128] D. H. Kim, E. Byon, G. H. Lee, and S. Cho, "Effect of deposition temperature on the structural and thermoelectric properties of bismuth telluride thin films grown by co-sputtering," *Thin Solid Films,* vol. 510, 1-2, pp. 148-153, 2006

[129] V. G. Veselago, "The electrodynamics of substances with simultaneously negative values of ε and μ," *Soviet Physics Uspekhi,* vol. 10, 1968

[130] S. Enoch, G. Tayeb, P. Sabouroux, N. Guerin, and P. Vincent, "A metamaterial for directive emission," *Physical Review Letters,* vol. 89, 21, p. 4, 2002

[131] R. W. Ziolkowski, "Propagation in and scattering from a matched metamaterial having a zero index of refraction," *Phys Rev E Stat Nonlin Soft Matter Phys,* vol. 70, 4 Pt 2, p. 046608, 2004

[132] I. Liberal and N. Engheta, "Near-zero refractive index photonics," *Nature Photonics,* vol. 11, 3, pp. 149-158, 2017

[133] N. Engheta, "Pursuing Near-Zero Response," *Science,* vol. 340, pp. 286-287, 2013

[134] M. Silveirinha and N. Engheta, "Tunneling of electromagnetic energy through subwavelength channels and bends using epsilon-near-zero materials," *Physical Review Letters,* vol. 97, 15, p. 157403, 2006

[135] Y. Li, I. Liberal, and N. Engheta, "Metatronic analogues of the Wheatstone bridge," *Journal of the Optical Society of America B,* vol. 33, 2, pp. A72-A79, 2016

[136] I. Liberal and N. Engheta, "Zero-index structures as an alternative platform for quantum optics," *Proceedings of the National Academy of Sciences of the United States of America,* vol. 114, 5, pp. 822-827, 2017

[137] B. Edwards, A. Alu, M. E. Young, M. Silveirinha, and N. Engheta, "Experimental verification of epsilon-near-zero metamaterial coupling and energy squeezing using a microwave waveguide," *Physical Review Letters,* vol. 100, 3, p. 033903, 2008

[138] I. Liberal, A. M. Mahmoud, Y. Li, B. Edwards, and N. Engheta, "Photonic doping of epsilon-near-zero media," *Science,* vol. 355, 6329, pp. 1058-1062, 2017

[139] A. Alù, M. G. Silveirinha, A. Salandrino, and N. Engheta, "Epsilon-near-zero metamaterials and electromagnetic sources: Tailoring the radiation phase pattern," *Physical Review B,* vol. 75, 15, 2007

[140] C. Della Giovampaola and N. Engheta, "Plasmonics without negative dielectrics," *Physical Review B,* vol. 93, 19, p. 195152, 2016

[141] R. Maas, J. Parsons, N. Engheta, and A. Polman, "Experimental realization of an epsilon-near-zero metamaterial at visible wavelengths," *Nature Photonics,* vol. 7, 11, pp. 907-912, 2013

[142] M. T. Sheldon *et al.*, "Plasmoelectric potentials in metal nanostructures," *Science,* vol. 346, pp. 828-31, 2014

[143] T. W. Ebbesen, H. J. Lezec, H. F. Ghaemi, T. Thio, and P. A. Wolff, "Extraordinary optical transmission through sub-wavelength hole arrays," *Nature,* vol. 391, pp. 667-669, 1998

[144] C. Genet and T. W. Ebbesen, "Light in tiny holes," *Nature,* vol. 445, 7123, pp. 39-46, 2007

[145] W. L. Barnes, a. Dereux, and T. W. Ebbesen, "Surface plasmon subwavelength optics," *Nature,* vol. 424, pp. 824-30, 2003

[146] D. Reibold, F. Shao, A. Erdmann, and U. Peshel, "Extraordinary low transmission effects for ultra-thin patterned metal films," *Optics Express,* vol. 17, 2, pp. 544-551, 2009

[147] I. S. Spevak, A. Y. Nikitin, E. V. Bezuglyi, A. Levchenko, and A. V. Kats, "Resonantly suppressed transmission and anomalously enhanced light absorption in periodically modulated ultrathin metal films," *Physical Review B,* vol. 79, 16, p. 161406, 2009

[148] J. Braun, B. Gompf, G. Kobiela, and M. Dressel, "How Holes Can Obscure the View: Suppressed Transmission through an Ultrathin Metal Film by a Subwavelength Hole Array," *Physical Review Letters,* vol. 103, 20, p. 203901, 2009

[149] B. Zeng, Y. Gao, and F. J. Bartoli, "Ultrathin nanostructured metals for highly transmissive plasmonic subtractive color filters," *Scientific Reports,* vol. 3, p. 2840, 2013

[150] E. Plum, V. A. Fedotov, A. S. Schwanecke, N. I. Zheludev, and Y. Chen, "Giant optical gyrotropy due to electromagnetic coupling," *Applied Physics Letters,* vol. 90, 22, p. 223113, 2007

[151] Y. Ye and S. He, "90° polarization rotator using a bilayered chiral metamaterial with giant optical activity," *Applied Physics Letters,* vol. 96, 20, p. 203501, 2010

[152] V. A. Fedotov, P. L. Mladyonov, S. L. Prosvirnin, A. V. Rogacheva, Y. Chen, and N. I. Zheludev, "Asymmetric propagation of electromagnetic waves through a planar chiral structure," *Physical Review Letters,* vol. 97, 16, p. 167401, 2006

[153] V. A. Fedotov, A. S. Schwanecke, N. I. Zheludev, V. V. Khardikov, and S. L. Prosvirnin, "Asymmetric Transmission of Light and Enantiomerically Sensitive Plasmon Resonance in Planar Chiral Nanostructures," *Nano Letters,* vol. 7, pp. 1996 - 1999, 2007

[154] M. Decker *et al.*, "High-Efficiency Dielectric Huygens' Surfaces," *Advanced Optical Materials,* vol. 3, 6, pp. 813 - 820, 2015

[155] T. Kaelberer, V. A. Fedotov, N. Papasimakis, D. P. Tsai, and N. I. Zheludev, "Toroidal Dipolar Response in a Metamaterial," *Science,* vol. 330, 6010, pp. 1510-1512, 2010

[156] N. Papasimakis, V. A. Fedotov, V. Savinov, T. A. Raybould, and N. I. Zheludev, "Electromagnetic toroidal excitations in matter and free space," *Nature Materials,* vol. 15, 3, pp. 263-271, 2016

[157] S. Feng, "Loss-induced omnidirectional bending to the normal in -near-zero metamaterials," *Physical Review Letters,* vol. 108, 19, p. 193904, 2012

[158] S. Zastrow *et al.*, "Thermoelectric transport and Hall measurements of low defect Sb2Te3thin films grown by atomic layer deposition," *Semiconductor Science and Technology,* vol. 28, 3, p. 035010, 2013

[159] H. Zou, D. M. Rowe, and G. Min, "Preparation and characterization of p-type Sb2Te3 and n-type Bi2Te3 thin films grown by coevaporation," *Journal of Vacuum Science & Technology A: Vacuum, Surfaces, and Films,* vol. 19, 3, pp. 899-903, 2001

[160] Y. Kim, A. DiVenere, G. K. L. Wong, J. B. Ketterson, S. Cho, and J. R. Meyer, "Structural and thermoelectric transport properties of Sb2Te3 thin films grown by molecular beam epitaxy," *Journal of Applied Physics,* vol. 91, 2, pp. 715-718, 2002

[161] H. Zhang, C.-X. Liu, X.-L. Qi, X. Dai, Z. Fang, and S.-C. Zhang, "Topological insulators in Bi_2Se_3, Bi_2Te_3 and Sb_2Te_3 with a single Dirac cone on the surface," *Nature Physics,* vol. 5, 6, pp. 438-442, 2009

[162] M. V. Bashevoy, V. A. Fedotov, and N. I. Zheludev, "Optical whirlpool on an absorbing metallic nanoparticle," *Optics Express,* vol. 13, 21, pp. 8372-8379, 2005

[163] M. Silveirinha and N. Engheta, "Tunneling of Electromagnetic Energy through Subwavelength Channels and Bends using ε-Near-Zero Materials," *Physical Review Letters,* vol. 97, p. 157403, 2006

[164] M. H. Javani and M. I. Stockman, "Real and Imaginary Properties of Epsilon-Near-Zero Materials," *Physical Review Letters,* vol. 117, 10, p. 107404, 2016

[165] E. Palik, *Handbook of Optical Constants of Solids*. Academic Press, 1998.

[166] A. M. Urbas *et al.*, "Roadmap on optical metamaterials," *Journal of Optics,* vol. 18, 9, p. 53, 2016

[167] C. Wu *et al.*, "Spectrally selective chiral silicon metasurfaces based on infrared Fano resonances," *Nature communications,* vol. 5, p. 3892, 2014

[168] P. Moitra, B. A. Slovick, Z. Gang Yu, S. Krishnamurthy, and J. Valentine, "Experimental demonstration of a broadband all-dielectric metamaterial perfect reflector," *Applied Physics Letters,* vol. 104, 17, p. 171102, 2014

[169] P. R. West *et al.*, "All-dielectric subwavelength metasurface focusing lens," *Optics Express,* vol. 22, 21, p. 26212, 2014

[170] F. J. F. Löchner *et al.*, "Polarization-Dependent Second Harmonic Diffraction from Resonant GaAs Metasurfaces," *ACS Photonics,* vol. 5, 5, pp. 1786-1793, 2018

[171] Y. Li *et al.*, "Ultrafast electron and phonon response of oriented and diameter-controlled germanium nanowire arrays," *Nano Letters,* vol. 14, 6, pp. 3427-31, 2014

[172] F. Tabataba-Vakili *et al.*, "Q factor limitation at short wavelength (around 300 nm) in III-nitride-on-silicon photonic crystal cavities," *Applied Physics Letters,* vol. 111, 13, p. 131103, 2017

[173] T. Wunderer *et al.*, "Optically pumped UV lasers grown on bulk AlN substrates," *physica status solidi (c),* vol. 9, 3-4, pp. 822-825, 2012

[174] M. Stegmaier, J. Ebert, J. M. Meckbach, K. Ilin, M. Siegel, and W. H. P. Pernice, "Aluminum nitride nanophotonic circuits operating at ultraviolet wavelengths," *Applied Physics Letters,* vol. 104, 9, p. 091108, 2014

[175] M. Soltani, R. Soref, T. Palacios, and D. Englund, "AlGaN/AlN integrated photonics platform for the ultraviolet and visible spectral range," *Optics Express,* vol. 24, 22, p. 25415, 2016

[176] M. Razeghi and A. Rogalski, "Semiconductor ultraviolet detectors," *Journal of Applied Physics,* vol. 79, 10, pp. 7433-7473, 1996

[177] K. H. Li, X. Liu, Q. Wang, S. Zhao, and Z. Mi, "Ultralow-threshold electrically injected AlGaN nanowire ultraviolet lasers on Si operating at low temperature," *Nature Nanotechnology,* vol. 10, 2, pp. 140-144, 2015

[178] M. Kneissl *et al.*, "Advances in group III-nitride-based deep UV light-emitting diode technology," *Semiconductor Science and Technology,* vol. 26, 1, p. 014036, 2010

[179] M. Asif Khan, M. Shatalov, H. P. Maruska, H. M. Wang, and E. Kuokstis, "III–Nitride UV Devices," *Japanese Journal of Applied Physics,* vol. 44, 10, pp. 7191-7206, 2005

[180] C. Argyropoulos, F. Monticone, G. D'Aguanno, and A. Alù, "Plasmonic nanoparticles and metasurfaces to realize Fano spectra at ultraviolet wavelengths," *Applied Physics Letters,* vol. 103, 14, p. 143113, 2013

[181] B. Gholipour, P. Bastock, C. Craig, K. Khan, D. Hewak, and C. Soci, "Microfibers: Amorphous Metal-Sulphide Microfibers Enable Photonic Synapses for Brain-Like Computing," *Advanced Optical Materials,* vol. 3, 5, pp. 634-634, 2015

[182] K. B. Borisenko *et al.*, "Photo-induced optical activity in phase-change memory materials," *Scientific Reports,* vol. 5, p. 8770, 2015

[183] C. C. Huang, B. Gholipour, J. Y. Ou, K. Knight, and D. W. Hewak, "Electrical phase change of CVD-grown Ge-Sb-Te thin-film device," *Electronics Letters,* vol. 47, 4, p. 288, 2011

[184] D. Hewak and B. Gholipour, "Primed to Remember," *Science,* vol. 336, 6088, pp. 1515-1516, 2012

[185] B. Gholipour, J. Zhang, K. F. MacDonald, D. W. Hewak, and N. I. Zheludev, "An All-Optical, Non-volatile, Bidirectional, Phase-Change Meta-Switch," *Advanced Materials,* vol. 25, 22, pp. 3050-3054, 2013

[186] Y. G. Chen *et al.*, "Hybrid phase-change plasmonic crystals for active tuning of lattice resonances," *Optics Express,* vol. 21, 11, pp. 13691-13698, 2013

[187] M. Rude *et al.*, "Optical switching at 1.55 um in silicon racetrack resonators using phase change materials," *Applied Physics Letters,* vol. 103, 14, p. 141119, 2013

[188] H. N. S. Krishnamoorthy, B. Gholipour, N. I. Zheludev, and C. Soci, "A Non-Volatile Chalcogenide Switchable Hyperbolic Metamaterial," *Advanced Optical Materials,* vol. 6, 19, p. 1800332, 2018

[189] B. Gholipour, A. Karvounis, J. Yin, C. Soci, K. F. MacDonald, and N. I. Zheludev, "Phase-change-driven dielectric-plasmonic transitions in chalcogenide metasurfaces," *NPG Asia Materials,* vol. 10, pp. 533-539, 2018

[190] D. Piccinotti, B. Gholipour, J. Yao, K. F. Macdonald, B. E. Hayden, and N. I. Zheludev, "Compositionally controlled plasmonics in amorphous semiconductor metasurfaces," *Optics Express,* vol. 26, 16, p. 20861, 2018

[191] J. Orava, A. L. Greer, B. Gholipour, D. W. Hewak, and C. E. Smith, "Characterization of supercooled liquid $Ge_2Sb_2Te_5$ and its crystallization by ultrafast-heating calorimetry," *Nat. Mater.,* vol. 11, 4, pp. 279-283, 2012

[192] N. I. Zheludev and E. Plum, "Reconfigurable nanomechanical photonic metamaterials," *Nature Nanotechnology,* vol. 11, 1, pp. 16-22, 2016

[193] D. Piccinotti, B. Gholipour, J. Yao, K. F. Macdonald, B. E. Hayden, and N. I. Zheludev, "Extraordinary Properties of Epsilon-Near-Zero and Low-Index Chalcogenide Metamaterials," presented at the Conference on Lasers and Electro-Optics, 2018. Available: http://dx.doi.org/10.1364/cleo_qels.2018.fth4h.6

[194] A. Agarwala and V. B. Shenoy, "Topological Insulators in Amorphous Systems," *Physical Review Letters,* vol. 118, 23, p. 236402, 2017

[195] N. P. Mitchell, L. M. Nash, D. Hexner, A. M. Turner, and W. T. M. Irvine, "Amorphous topological insulators constructed from random point sets," *Nature Physics,* vol. 14, 4, pp. 380-385, 2018

[196] J. Jung, J. Bork, T. Holmgaard, N. Anker Kortbek, and K. Pedersen, "Ellipsometry," Aalborg University, Institute of Physics and Nanotechnology2004.

[197] R. M. A. Azzam and N. M. Bashara, *Ellipsometry and polarized light*. 1987.

[198] J. A. W. C. Inc, "CompleteEASE ™ Data Analysis Manual," ed, 2011, pp. 1-207.

[199] J. Jianming, IEEE, Ed. *The finite element method in electromagnetics*. Wiley-IEEE Press, 2002.

List of Publications

Articles

- "Compositionally controlled plasmonics in amorphous semiconductor metasurfaces", D. Piccinotti, B. Gholipour, J. Yao, K. F. MacDonald, B. E. Hayden, and N. I. Zheludev, *Opt. Express*, vol. 26, pp. 20861-20867, 2018.
- "Optical Response of Nano-hole Arrays Filled with Chalcogenide Low-epsilon Media", D. Piccinotti, B. Gholipour, J. Yao, K. F. MacDonald, B. E. Hayden, and N. I. Zheludev, *Adv. Opt. Mat.,* vol. 6, 22, 1800395, 2018 – chosen for back-cover publication in issue 22/2018.
- "Stoichiometric engineering of chalcogenide semiconductor alloys for nanophotonic applications", D. Piccinotti, B. Gholipour, J. Yao, K. F. MacDonald, B. E. Hayden, and N. I. Zheludev, *Adv. Mat.,* vol. 31, 14, e1807083, 2019.
- "Reconfigurable ultraviolet and high-energy-visible dielectric metamaterials", B. Gholipour, D. Piccinotti, A. Karvounis, K. F. MacDonald and N. I. Zheludev, *Nano Lett.*, vol. 19, 3, pp. 1643-1648, 2019.

Conference Contributions

- "Extraordinary properties of chalcogenide metamaterials", K. F. MacDonald, D. Piccinotti, A. Karvounis, B. Gholipour, J. Yao, B. E. Hayden, and N. I. Zheludev, *12th International Congress on Artificial Materials for Novel Wave Phenomena*, Espoo, Finland, 27 Aug – 1 Sept 2018.
- "Extraordinary properties of epsilon-near-zero and low-index chalcogenide metamaterials", D. Piccinotti, B. Gholipour, J. Yao, K. F. MacDonald, B. E. Hayden, and N. I. Zheludev, *CLEO 2018*, San Jose, CA, USA, 13-18 May 2018.
- "New materials for metamaterials: plasmonic and ENZ chalcogenides", K. F. MacDonald, D. Piccinotti, B. Gholipour, J. Yao, B. E. Hayden, and N. I. Zheludev, *SPIE Photonics Europe 2018,* Strasbourg, France, 22-26 Apr 2018.

- “Optical switching in nanostructured phase change materials”, B. Gholipour, D. Piccinotti, J. Yao, K. F. MacDonald, B. E. Hayden, and N. I. Zheludev, *Photonics West 2018,* San Francisco, CA, USA, 2018, 27 Jan - 1 Feb 2018.
- “Not-so-extraordinary transmission through an array of nano-holes in a metal film”, D. Piccinotti, B. Gholipour, J. Yao, K. F. MacDonald, B. E. Hayden, and N. I. Zheludev, *PIERS 2017*, Singapore, 19 - 22 Nov 2017.
- “Tunable epsilon near-zero chalcogenides”, B. Gholipour, D. Piccinotti, J. Yao, K. F. MacDonald, B. Hayden, and N. I. Zheludev, *Metamaterials'2017*, Marseille, France, 28 - 31 Aug 2017.
- “Merging metamaterial and optical fiber technologies”, N. I. Zheludev, K. F. MacDonald, E. Plum, A. Karvounis, D. Piccinotti, A. Xomalis, I. Demirtzioglou, V. Savinov, B. Gholipour, Y. Jung, P. Petropoulos, and D. J. Richardson, *META2017*, Seoul, South Korea, 25 - 28 Jul 2017.
- “Merging photonic metamaterial and optical fiber technologies”, A. Xomalis, D. Piccinotti, A. Karvounis, I. Demirtzioglou, V. Savinov, B. Gholipour, J. Y. Ou, Y. Jung, E. Plum, P. Petropoulos, K. F. MacDonald, D. J. Richardson, and N. I. Zheludev, *Integrated Photonics Research, Silicon, and Nano-Photonics*, New Orleans, LA, USA, 24 - 27 Jul 2017.
- “Combinatorial search for plasmonic and epsilon-near-zero chalcogenide alloys”, D. Piccinotti, B. Gholipour, J. Yao, K. F. MacDonald, B. E. Hayden, and N. I. Zheludev, *CLEO Europe - EQEC 2017,* Munich, Germany 25 - 29 Jun 2017.
- “Fibre-coupled photonic metadevices”, A. Xomalis, D. Piccinotti, A. Karvounis, H. Zhang, V. Savinov, B. Gholipour, Y. Jung, A. C. Peacock, E. Plum, K. F. MacDonald, D. J. Richardson, and N. I. Zheludev, *Nanometa 2017*, Seefeld, Austria, 4 - 7 Jan 2017.
- “Plasmonic response of chalcogenides and switchable all-dielectric metamaterials”, B. Gholipour, D. Piccinotti, J. Yao, A. Karvounis, J. Yin, C. Soci, B. E. Hayden, K. F. MacDonald, N. I. Zheludev, *Nanometa 2017*, Seefeld, Austria, 4 - 7 Jan 2017 (poster).
- “Nano-optomechanical dielectric metasurfaces reconfigurable with light”, A. Karvounis, J. Y. Ou, D. Piccinotti, W. Wu, E. Plum, K. F. MacDonald, and N. I. Zheludev, *Materials Research Society MRS 2015 Fall Meeting & Exhibit*, Boston, MA, USA, 29 Nov - 4 Dec 2015.